

Design Guidelines for Radial Supersonic Stators

J.H. Stuijt Giacaman

Preliminary (Meanline) Design Guidelines

for unconventional stator vanes operating under non-ideal flow conditions



Design Guidelines for Radial Supersonic Stators

by

J.H. Stuijt Giacaman

to obtain the degree of Master of Science in Mechanical Engineering
at the Delft University of Technology.
To be defended publicly on Tuesday October 23rd, 2018 at 10:00 AM.

Student number:	4217721	
Project duration:	August 28, 2017 – October 23, 2018	
Supervisors:	Dr. ir. M. Pini,	TU Delft (FPP)
	Ir. N. Anand,	TU Delft (FPP)
Thesis committee:	Dr. ir. R. Pecnik,	TU Delft (P&E)
	Dr. ir. C. A. Infante Ferreira,	TU Delft (P&E)

This thesis is confidential and cannot be made public until October 23, 2023.

An electronic version of this thesis is available at <http://repository.tudelft.nl/>.

*"There is no passion to be found playing small
in settling for a life that is less than the one you are capable of living."*

Nelson Mandela

Abstract

Increasing concerns about the effects of freeing large quantities of greenhouse gases into the atmosphere have sparked interest in organic Rankine cycle for renewable power systems. Single-stage radial inflow turbines appear as suitable expansion devices for this type of application. However, supersonic conditions can be reached in the stator of these devices, causing non-ideal fluid-dynamic behavior. This makes it necessary to explore unconventional architectures, for which only a limited number of design methods have been proposed.

In this context, the principal activity of this study was to formulate guidelines, and thereby reduce the preliminary design space, of supersonic radial stator vanes. This was done by first identifying the relevant loss mechanism and design parameters through an examination of the available literature. This led to the formulation of a research hypothesis, which was studied by means of two-dimensional, steady computational fluid dynamic simulations.

To this end, a parametric study was devised, in which any design parameter can be varied to study its effect on the blade performance. This is done analyzing the trends resulting from the post-processing of simulation generated data. The data production is based on a workflow consisting of finding a condition-specific convergent-divergent nozzle, which is used to build a mean-line radial vane, for which a mesh grid is generated and utilized by a previously validated numerical solver to perform the simulations. The complete process was overseen by a semi-automated design chain constructed to manage and execute the necessary steps.

It was assumed that profile losses would be the most influential loss characteristic, given that two-dimensional flow is predominant in mean-line geometries. According to the literature, both its major components, viscous dissipation and mixing losses should have an impact on the stator's efficiency. Likewise, the degree of expansion along the embedded nozzle present between adjacent blades, was identified as the main design specifications to be analyzed. A trade-off between the contribution of the main loss mechanisms based on the variation of this parameter was predicted to exist.

Applying the generalized research method on a candidate test case resulted in the generation of data from almost 500 different simulations. This led to several findings, including that it is not possible to vary the nozzle design Mach number without causing simultaneous changes to other relevant geometrical features, such as the throat width. This rendered invalid some of the initial assumptions used to set up the experiments.

Similarly, this finding was expected to be the reason behind large differences between the calculated and imposed pressure ratio on the boundary conditions, as well as large variations in the mass flow of each set of blades. Additional simulations were required to analyze these deviations, based on varying other relevant parameters, including the imposed pressure ratio and outflow boundary location. The results seem to suggest that, due to the supersonic nature of the flow, an additional geometrical constraint influences the expansion process.

Performance analyzes were then possible by adapting the definition of valid designs to blade configurations matching or exceeding the imposed pressure ratio. Based on these results, the relevance of the post-expansion ratio (defined as the ratio between the pressure level at the nozzle exit and the stator outflow) became apparent. This was also the case when this ratio was manipulated by changing the imposed back pressure on the system. Moreover, when quantified with respect to this parameter, the flow deviation showed a linear behavior and the losses exhibited a plateau of higher performance.

Finally, this project provides a foundation for this line of research, both in a theoretical and practical sense. Future studies should focus on validating claims made regarding the supersonic expansion process and extending the data to determine the generality of the found performance trends. Only then will it be possible to conclusively establish the dependence between design parameters and performance for this unconventional type of blade.

Acknowledgements

Before you lies the end of a journey, one which started over six years ago when I first arrived at Delft, full of energy, hungry of knowledge and keen to overcome any challenge that stood before me. A journey with ups and downs, twist and turns and full of surprises. A journey which made me who I am now.

Although, more concretely, this report the final product of my thesis project, the last requirement to earn the MSc. degree in Mechanical Engineering and thereby the Engineer title. This project started at the end of August 2017, with a kick-off meeting between me and my two supervisors, Matteo Pini and Nitish Anand. It will end at the end of October 2018 when I shall defend my work before the appointed thesis committee.

During this period I devoted an estimated 1500 direct hours of work to accomplish what is contained in these pages. This, of course, does not take into account the uncountable hours of guidance by my supervisors and work of all the university support staff which make it possible to study at the TU Delft. Nonetheless, it became the toughest task I have had to undertake in the almost 25 years of my life and it will most probably be the pinnacle of my academic achievements.

I would first like to thank Matteo for believing in me and entrusting me such a challenging task, but also for his guidance and counsel throughout the project. My special thanks also go to Nitish, who assisted me closely during my work and without whose support and would not have achieved the attained results. My gratitude goes to Rene Pecnik and Carlos Infante Ferreira, for accepting to be in my thesis committee and taking the time to review my work. Also, to my little brother Willem, thank you for taking time of your vacations to help me finalize some details of the report.

Finally, a word of thanks is due to my study counsellor Lourdes for the mental support you gave me and my family for coping with me during my worst moments. And last but not least, to my many friends in Delft to whom I could reach out when I needed a distraction.

Preface

In my search for the next challenge in my life and a spectacular closure for my university period, I came across the projects of my soon to be thesis supervisor Matteo Pini. I was looking for something ambitious, which would possibly lead to a useful finding or insights and the opportunity to develop new hard skills. I was aware my thesis project would be a unique opportunity to dedicate full time to study a topic of my choice to a level I will probably never reach again in my life.

After some discussions, a project about formulating design guidelines for a supersonic turbine drew my attention. When I accepted to undertake the project, I was expecting to carry out some type of optimization. It took me time to realize I was actually going to return to basics and perform a much more fundamental kind of analysis: explore the design space based on the underlying physics of the complex flows arising within these devices.

This would lead me into a journey of almost 14 months, a period which also included time spent in other activities of personal development and some unexpected trips, but nonetheless a period where I devoted many hours into making this the best project I could possibly deliver. It all started with some weeks of planning, after which I dived deep into the literature related to supersonic (radial) vanes. To fully grasp the complexity of the topic, it was necessary for me to learn some additional subjects, such as gas dynamics and compressible fluid dynamics.

Then came the moment where I had to convert my programming skills into actual coding with *Python* and confront the existing code handed over to me by my supervisors. I spent weeks (more than I actually would have wanted) developing a robust automated procedure for generating a blade contour based on a given set of nozzle coordinates. Then came the meshing, the carrying out of the simulations in the faculty cluster (a single simulation in my own computer would take at least 5 hours and not allow me to do any other work), followed by the non-trivial task of post-processing of the generated data.

However, this complete process was not in any way as linear as described above. Already after the first set of results were available, we realized the assignment had to change slightly its course; the calculated pressure ratio unexpectedly would deviate largely from the imposed value on the boundary conditions, invalidating a major initial assumption on which the research hypothesis was formulated. This led to the need of more simulations and more work than planned. Finally, after finding a way to overcome the experimental hurdle and come up with an explanation for my results, I needed to put all the work on paper, a step I completely underestimated.

In any case, I am proud of the results of this undertaking and I am very confident that this work has provided some useful insights to the much larger goal of designing efficient unconventional radial inflow turbines in an effective manner. To the reader, if you stumbled upon my work for your own research project, I would be very glad if this report can provide you with any useful information. If you are reading this just by sheer interest, please enjoy the reading.

J.H. Stuijt Giacaman

Delft, October 2018

Contents

Preface	iv
Acronyms	vii
Nomenclature	viii
List of Figures	xii
List of Tables	xv
1 Introduction	1
1.1 Project Context	1
1.1.1 Energy Transition	1
1.1.2 Organic Rankine Cycle Power Systems	2
1.2 Research Framework	4
1.2.1 Problem Statement	4
1.2.2 Objective & Research Questions	5
1.2.3 Original Contribution	5
1.3 Report Outline	6
2 Theoretical Background	7
2.1 Radial Turbine Architecture & Design	7
2.1.1 Traditional Configurations	7
2.1.2 (Unconventional) Highly Supersonic Operation	8
2.2 Turbomachinery Performance	12
2.2.1 Loss Accounting	13
2.2.2 Two-Dimensional Loss Mechanisms in Turbine Vanes	14
2.2.3 Unconventional (Radial) Losses	18
2.3 Research Hypothesis	21
3 Methodology	24
3.1 Parametric Study	24
3.2 Blade Design & Simulation Tools	25
3.2.1 Inverse Methodology Nozzle Design (MoC Tool)	25
3.2.2 Radial Stator Tool	27
3.2.3 Computational Domain Discretization (Meshing)	33
3.2.4 Numerical Solver	34
3.2.5 Additional Post-Processing	36
3.3 Semi-Automated Design Chain	36
4 Method Application	38
4.1 Case Study	38
4.1.1 Test Case	38
4.1.2 Simulation Details	38
4.2 Results & Discussion	40
4.2.1 Geometry Sensitivity Analysis	41
4.2.2 Stage Expansion Behavior	43
4.2.3 Stator Performance	53
4.2.4 Supplementary Variable Monitoring	57
5 Research Closure	61
5.1 Conclusions	61
5.2 Recommendations	62

A SU2 Configuration File	64
B Mesh Convergence Study	72
C Line Integration Validation	76
Bibliography	77

Acronyms

2D	Two-dimensional
AI	Artificial intelligence
BC	Boundary condition
BL	Boundary layer
BV	Base value
C-D	Convergent-divergent
CFD	Computational fluid dynamics
MoC	Method of Characteristics
NICFD	Non-ideal compressible fluid dynamics
NRBC	Non-reflecting boundary condition
NURBS	Non-uniform rational Bézier-spline
ORC	Organic Rankine cycle
PE	Post-expansion
RIT	Radial inflow turbine
RST	Radial Stator Tool
TE	Trailing edge

Nomenclature

Latin Letters

- A* Nozzle exit cross-section length [m]
- B* NURBS basis function
- c* Specific heat capacity of a material on a per mass basis [$\text{kJ K}^{-1} \text{kg}^{-1}$]
- C* Blade chord [m] or non-dimensional coefficient [-]
- e* Distance between two relevant points used in building radial stator blade [m]
- F* Scaling factor [-]
- H* Thickness [m]
- h* Enthalpy [kJ kg^{-1}]
- I* Rothalpy [kJ kg^{-1}]
- J* Minimization function
- k* Degree of curve [-]
- L* Pitch length [m]
- l* Gap between plates [m]
- M* Mach number [-]
- m* Size of knot sequence [-] or mass [kg]
- L* NURBS function
- n* Number or nozzle
- O* Throat width [m] (in some cases the origin of coordinate system)
- P* Pressure [Pa, bar]
- Q* NURBS specific interval
- q* NURBS specific variable
- R* Radius [m]
- Re* Reynolds number [-]
- S* Stator outlet / rotor inlet area length [m]
- s* Entropy [$\text{kJ kg}^{-1} \text{K}^{-1}$]
- T* Temperature [K]
- t* Trailing edge thickness [m]
- U* Angular velocity [m s^{-1}]
- u* Horizontal (or normal) velocity component [m s^{-1}]

- V Dummy variable
 v Vertical velocity component [m s^{-1}]
 w Weight of control point [-]
 x Euclidean horizontal coordinate [m]
 y Euclidean vertical coordinate [m]
 Z Parameter in Design Chain
 z Value of specific parameter in Design Chain

Greek Letters

- α Deviation angle [$^{\circ}$]
 δ Boundary layer thickness [m]
 ϵ General error or difference [-]
 γ Ratio of specific heat capacities [-]
 η Isentropic efficiency [-]
 κ Expansion section angle [rad]
 Ω Angular velocity [rad s^{-1}]
 ϕ Gauging or flow angle [$^{\circ}$]
 β Pressure ratio [-]
 ρ Density [kg m^{-3}]
 Θ Angle used in the solution of the MoC [$^{\circ}$]
 θ Pitch angle [rad]
 ν Kinematic viscosity [Pa s]
 φ Stagger angle [$^{\circ}$]
 ζ Loss coefficient [-]

Subscripts

- 0 Start of nozzle or first value in range
 β Matching the imposed pressure ratio
conv Convergent
2D Two-dimensional
BC Boundary Condition
BL Boundary Layer
BV Base value
PE Post-expansion
TE Trailing Edge
 i Denoting the count of a parameter

<i>in</i>	Incoming
<i>irr</i>	Irreversible process
<i>kern</i>	Kernel region
<i>max</i>	Maximum
<i>min</i>	Minimum
<i>s</i>	Isentropic
<i>o</i>	Total or stagnation conditions
<i>opt</i>	Optimum
<i>out</i>	Outgoing
<i>PS</i>	Pressure side
<i>R</i>	Blade outlet radius
<i>ref</i>	Reference
<i>rel</i>	Relative
1	Stator inflow
2	Stator outflow / rotor inflow
3	Rotor outflowv/ diffuser inflow
4	Rotor outflow / diffuser inflow
<i>a</i>	Nozzle exit
<i>B</i>	Base
<i>b</i>	Blade exit
<i>d</i>	Dissipation
δ	Related to boundary layer thickness
<i>e</i>	Conditions far from blade wall (also used to denote electric power)
<i>gen</i>	Generation coefficient
<i>g</i>	To denote relation to universal gas constant ($8.314 \text{ J mol}^{-1} \text{ K}^{-1}$)
<i>m</i>	Final value of NURBS knot sequence
<i>p</i>	Isobaric
<i>SS</i>	Suction side
<i>t</i>	Throat conditions
<i>stator</i>	Overall value for the stator stage
<i>w</i>	With respect to wall
<i>x</i>	Along x-axis
<i>y</i>	Along y-axis
<i>tot</i>	Total-to-outflow

visc Viscous

h Enthalpy based

k Kinetic energy based

P Stagnation pressure based

S Entropy based

Superscripts

* Properties at sonic conditions

' Adjacent

2 Denoting 2nd order continuity of a function

List of Figures

1.1	Projected world primary energy consumption. Adapted from [1] based on data from [2]	2
1.2	Picture of an operational RIT [15]	4
2.1	Schematic layout of a traditional RIT. Adapted from [8]	7
2.2	Mollier diagram of a typical RIT at design point. Adapted from [8]	8
2.3	Shape and profile of blades employing different nozzle types according to the application. (a) Convergent nozzle for subsonic cascade (b) Convergent nozzle for transonic cascade (c) C-D channel for high supersonic velocities. Adapted from [23]	9
2.4	Schematic diagram of a generic C-D (supersonic) nozzle. Adapted from [24]	9
2.5	Schematic diagram of supersonic nozzle contour designed using the method of characteristics. Adapted from [24].	10
2.6	CFD results of Mach number (left images) and pressure gradient (right image) contours of stators designed using different methods. (a) Base design (b) CFD-based optimization (c) MoC-based design. Adapted from [10].	11
2.7	Diagram summarizing classification of loss characteristics in turbine. Adapted from [29]	12
2.8	Schematic diagram of a turbulent boundary layer in a blade surface. Adapted from [32]	15
2.9	Idealized flow distribution along blade. Adapted from [34]	15
2.10	Supersonic flow structure around a blunt blade trailing edge. Adapted from [36]	16
2.11	Schematic diagram of staggered plates with control volume for trailing edge analysis. Adapted from [36]	17
2.12	Schematic diagram of unstaggered plates with a proposed control volume. Adapted from [36]	18
2.13	Predicted increase in mass-averaged entropy along meanline distance for a test case, for steady and unsteady simulations. Adapted from [16]	19
2.14	Instantaneous entropy generation rate of the unsteady simulation of a highly supersonic radial ORC turbine. Light shading represents minimum values and dark shaded areas are the maximum. Relevant variables have been added and the boundaries of the stator stage have been marked for reference purposes. Adapted from [15]	20
2.15	Sketch of the expected optimum existing for the profile losses of C-D stator blades based on the variation of the nozzle design Mach number	23
3.1	Flow diagram depicting the steps required to build and simulate a blade configuration	25
3.2	Plot of the characteristic lines used for the calculations to design the diverging region of a nozzle	26
3.3	Plot of the nozzle coordinates resulting from the MoC-solver	26
3.4	Schematic diagrams of the steps required to generate a radial blade geometry contour. Adapted from [38].	28
3.5	Schematic diagram of a stator vane geometry generated using the RST, including the chosen control points for the NURBS	29
3.6	Visualization of the conformal mapping procedure [38]	30
3.7	Visualization of the change of nozzle centerline after conformal mapping procedure within the radial limits of the stage. Adapted from [38]	30

3.8	Visualization of the final product of the conformal mapping and nozzle positioning procedure. Adapted from [38]	30
3.9	Schematic diagram of the relevant geometric features of a C-D radial stator blade	33
3.10	Plots of (a) computational region and (b) the resulting output of the meshing tool, including a close-up of the TE and outflow regions	34
3.11	Plot of an eighteen blade stator stage including radial limits	35
3.12	Flow diagram illustrating the structure and workflow of the semi-automated design and simulation chain	37
4.1	Plot of the TE thickness and blade outlet radius errors, solidity and throat scaling (from top to bottom) for varying values of the nozzle design Mach	41
4.2	Plot of the TE thickness and blade outlet radius errors, solidity and throat scaling (from top to bottom) for varying values of the flow angle	42
4.3	Plot of the TE thickness and blade outlet radius errors, solidity and throat scaling (from top to bottom) for varying values of the blade outlet radius	43
4.4	Plots of different blade configurations showing the sensitivity of the geometry with respect to (a) nozzle design Mach (b) gauging angle	44
4.5	Simulation results of outflow Mach and total-to-outflow pressure ratio for blade configurations with varying value of M_a	45
4.6	Pressure gradient contour of two equal configurations simulated using (a) Giles (NRBC) and (b) Riemann (Reflective) boundary conditions	46
4.7	Mach and pressure gradient contours of an (a) under-expanded (b) matching and (c) over-expanded blade configurations	47
4.8	Simulation results of outflow Mach and stage pressure ratio for blade configurations with varying M_a plotted against the relevant area ratio	48
4.9	Simulation results of outflow Mach and stage pressure ratio for configurations with varying M_a , for different values of β_{BC} , plotted against the relevant area ratio	49
4.10	Fitted simulation results of outflow Mach and stage pressure ratio for under-expanded configurations	50
4.11	Simulation results of outflow Mach and stage pressure ratio for blades with varying nozzle design Mach and different outflow radius, plotted against the relevant area ratio	51
4.12	Simulation results of β_{tot} for a blade configuration tested under different stage pressure ratios (by varying P_2)	52
4.13	Simulation results of the difference between calculated and imposed total-to-outflow pressure ratio for blades with varying M_a plotted against the resulting post-expansion ratio	52
4.14	Simulation results of stage pressure ratio, flow deviation and entropy generation (from top to bottom respectively) for configurations with varying M_a	53
4.15	Simulation results of outflow Mach, flow deviation and entropy generation (from top to bottom respectively) plotted against the calculated post-expansion ratio, for blades with varying M_a	54
4.16	Pressure gradient and Mach contour plots of blade configurations with differing M_a leading to (a) re-compression (b) no post-expansion (c) post-expansion in the PE region	56
4.17	Simulation results of outflow Mach, flow deviation and entropy generation (from top to bottom respectively) plotted against the PE ratio (for varying imposed back pressures)	57
4.18	Pressure gradient and Mach contour plots of fixed blade configurations ($M_a = 2.2$) simulated for different stage pressure ratios (by varying the imposed back pressure), leading to (a) re-compression (b) no post-expansion (c) post-expansion in the PE region	58
4.19	Simulation results of flow deviation and entropy production of different blades plotted against the res (for varying imposed back pressure)	59
4.20	Simulation results of throat Reynolds number and normalized mass flow for variations of nozzle design Mach	60

4.21 Simulation results of entropy generation for values of artificially varied throat Reynolds on a fixed blade configuration	60
B.1 Mesh convergence for number of simulation iterations	73
B.2 Mesh convergence for boundary layer thickness	73
B.3 Mesh convergence for number of elements	74
B.4 Mesh convergence for trailing edge refinement radius	75

List of Tables

3.1	Input parameters required to run MoC solver	26
3.2	Summary of control points including short description and corresponding weight value	32
4.1	Overview of important design parameters of the test case and their original base value	39
4.2	Summary of all the runs and the respective jobs performed to collect the necessary data for the analysis	40
5.1	Summary of dependencies between performance, behavior and relevant design parameters for fixed geometrical and operating conditions	62
C.1	Results between commercial package line integration and custom made script for mass (entropy) and area (pressure) average values	76

Introduction

To open this report, this chapter will provide introductory information in an attempt to place the reader in the relevant context related to the project and to motivate the efforts carried out during the research. This will be done by first presenting an overview of the background surrounding the main topic, followed by the research framework on top of which the project was built. Finally, the contents of the remainder of the report will be briefly outlined. Although the contents of this chapter have been attempted to be maintained as general as possible, basic knowledge of turbomachinery and the (organic) Rankine cycle will probably better help assimilate the context and the motivation of this work better.

1.1. Project Context

To understand the motivation to carry out a project of this kind, it is important to first comprehend the context surrounding it. In this section this background will be briefly epitomized; to do this, the information has been broken down and presented in fragments of thematic similarity containing what was deemed to be the relevant information for the reader.

1.1.1. Energy Transition

Fossil fuels, an energy source formed naturally inside deep layers of the earth during millions of years, have been one of the primary drivers for the economic growth and technological advancements experienced in the past century. Although the reliable and stable power made available from burning these fuels has benefited society in numerous ways, a growing unease about the effects of freeing carbon dioxide, a greenhouse gas, into the atmosphere by combustion processes has offset a new global energy transition in motion.

Assuming the global temperatures can be maintained under control by containing the emission of greenhouse gases, a great deal remains to be done. The problem could be approached by breaking it down into the demand (consumption) and the supply (generation) side of power distribution. Decades of growth in consumption and forecasts predicting a prolongation of this trend seem to demonstrate the ineffectiveness of attempting to mitigate the world's appetite for energy. Such a projection can be found in Figure 1.1, where trends of past consumption and predictions for the coming decades confirm the previous statement.

It can be observed in Figure 1.1 that renewable energies, excluding hydroelectric and nuclear sources, are expected to play a larger role in the future energy economy; this group should to present the largest relative growth. This fact also highlights how the focus remains on the supply side of power generation, with world-wide efforts of making available larger quantities of low-emission energy. However, various of these sources, including nuclear, but also geothermal, concentrated solar power and ocean thermal energy conversion, still require a thermal cycle for its energy production.

On the other hand, there is still room for improvement in the demand side of the problem. The largest opportunities can be found in increasing the effectiveness of energy consuming process. This is probably the reason energy efficiency is a priority topic in the agenda of

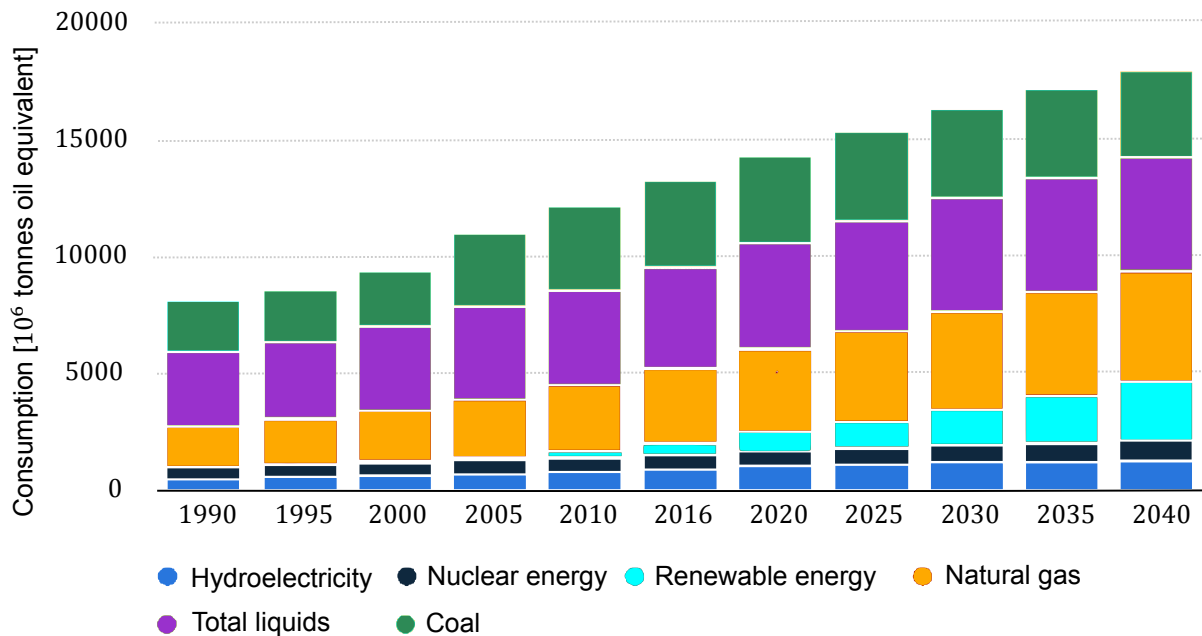


Figure 1.1: Projected world primary energy consumption. Adapted from [1] based on data from [2]

the European Energy Commission [3]. An important area within this topic is thermal energy recovery from waste heat streams. For example, statistical studies have shown that industrial low-grade waste heat accounts for more than half of the energy used for heat generation in this sector [4].

A large fraction of the energy used for heating purposes is released into the environment in the form of warm exhaust streams such as cooling water, cooling tower vapor, hot flue gases, among other examples. Not only is there a large potential for energy savings from these sources, but waste heat recovery can also reduce the possible hazards of thermal pollution.

Both reducing the demand of power by improving energy consuming processes and increasing the supply of renewables are ways of reducing unwanted emissions. Both tasks would benefit greatly from efficient thermal cycles and providing these will therefore be a necessary task in the context of the world energy transition.

1.1.2. Organic Rankine Cycle Power Systems

It is within the situation presented in the previous section that the growing interest for Organic Rankine cycle (ORC) power systems can be understood. An important reason for this is the added capabilities this technology provides for both power generation and in thermal energy recovery. Currently, the ORC technology has matured and is already well established for the conversion of heat from low-temperature geothermal reservoirs, concentrated solar power, biomass fuels and different sources of waste heat streams [5].

Although the first theoretical developments of this technology were first brought to light in the 1960s, it has been gaining traction in the past years as a better understanding of Non-ideal compressible fluid dynamics (NICFD) has been developed, together with an increase in computational power availability needed for ever more accurate numerical methods to predict fluid behavior, known as Computational fluid dynamics (CFD).

Using a Rankine cycle-based heat engine is a suitable means for energy production based on a thermal energy source. However, traditional heat engines using water as its working fluid cannot extract energy efficiently from heat sources with temperatures lower than 370°C [4], thereby reducing the range of possible applications considerably. Opportunities for improvement are made available by employing other working fluids in the cycle, with organic compounds being suitable candidates [6]; this is the basic working principle behind the ORC.

Benefits of employing an organic fluid in the Rankine cycle instead of water include higher flexibility in terms of capacity and temperature levels and the possibility of co-generating heat

and/or cooling [7]. These advantages are important in the framework of decentralized power generation, which is expected to play an important role in future energy systems. The ORC can therefore be seen as an extension of the traditional steam cycle, far better suited for the new and more dynamic energy landscape which is being shaped during the 21st century.

Nonetheless, the technology still presents shortcomings which still have to be overcome. The main issues are related to the efficiency of the cycle in converting heat energy into useful electricity. A critical component impacting the overall efficiency of such a system is the cycle expander, where the thermal energy absorbed by the working fluid can be converted into useful electrical energy.

Expanders for Organic Fluids

Although different types of expansion devices exist, for the typical power generation capacity of ORCs, which ranges from a few kW_{el} to several MW_{el} , the choice of preference is utilization of turbo-generators. This is the name given to all those devices in which energy is transferred either to, or from, a continuously flowing fluid by the dynamic action of one or more moving blade rows [8]. The focus of this work lies on the so called closed machines, those that produce power by expanding fluid to a lower pressure, or head, in an enclosed environment.

As mentioned in the previous section, the employment of organic fluids offers several advantages with respect to the heat engine cycle, especially related to the effectiveness of the expansion process. Aside from flexibility in temperature and pressure levels due to the range of possible saturation vapor curves, organic compounds usually consist of complex and heavy molecules. This property is inversely proportional to the enthalpy change related to an expansion process. Changes in pressure levels with a lower enthalpy drop will require less stages and consequently lead to lower mean peripheral speeds and mechanical stresses on the turbine equipment [9].

However, to make use of the full potential of these benefits, several complications arising from the same characteristics which provide the benefits must be dealt with. For starters, a group of complex molecules, as the ones composing organic fluids, will behave in a more non-ideal manner than traditional working fluids. Similarly, a lower number of stages will increase the pressure ratio per stage. When employing organic compounds in a turbine type expander, the lower speed of sound of the fluid in combination with a large pressure ration will usually result in highly supersonic flow within the first stage of the device [9]. This complicates the design procedure and limits the type of architectures that can be utilized.

Radial Inflow Turbines

Within the devices classified as turbo-generators, there are also several types of commonly used architectures. For single-stage, low power-output applications, radial turbines have traditionally received preference as the configuration of choice due to their high power density and their capacity to handle large volumetric flow rates [10]. Studies have shown that, for the range of applications considered in this work, this is also the case for ORC power systems [11].

More specifically, it has been asserted that Radial inflow turbine (RIT)s are a reasonable choice of expander in mini and small high-temperature cycles ORC [12, 13]. This has been confirmed by more recent work has recommending the use of single-stage RITs for small scale ORC applications [14]. A operational example of such a turbine can be appreciated in Figure 1.2.

The basic working principle of these devices will be dealt with in the next chapter. However, it can be observed that a turbine stage consists of two main components: the stator and the rotor. Although traditionally the rotor has been known to concentrate most of the losses and is usually designed more carefully than the stator, the contrary has been found to be true for turbines operating under supersonic conditions [16]. For this reason, more unconventional design methodologies must be employed to produce efficient working devices.

To date, a limited number of methods have been proposed to design the stator blades of unconventional types of turbines [17]. In recent years, scientists and designers have been slowly and increasingly resorting to intelligent CFD based optimizations to carry out the design process. This is in part due to the larger availability and improved accuracy of CFD



Figure 1.2: Picture of an operational RIT [15]

tools and the increasing capabilities of Artificial intelligence (AI). But also due to the lack of understanding of the underlying physical phenomena controlling the fluid behavior in non-ideal cases, knowledge which seems to become redundant when smart algorithms can do the work.

For this reason, results of these methods cannot easily be generalized, and need to be applied from scratch for each new design. This is due to what has better been expressed in the following lines: “Today’s AI systems are pattern-recognition engines, trained on thousands of examples in the hope that the rules they infer will continue to apply in the wider world. But they apply those rules blindly, without a human like understanding of what they are doing or an ability to improvise a solution on the spot...” [18]. Relying solely on these procedures has then the limitation of being time computational-resource consuming.

This has led to the emergence of more research focusing on physical modelling and understanding of flow behavior. In the case of the design of unconventional supersonic stators, the use of an inverse design methodology based on the theory of characteristics [19] has been found to be a suitable starting point for a more physics backed procedure. Recently, this theoretical approach has been successfully implemented in a method which was also adapted to account for the effects of NICFD [10].

Despite the physical-based design strategy showing a substantial improvement in the performance of the preliminary design of stator blades, it was found that the method on itself cannot guarantee the optimal fluid-dynamic behavior of an arbitrary configuration [10]. The method requires knowledge about the value of certain design parameters in order to provide an optimal design.

1.2. Research Framework

Research framework refers to the theoretical structure devised to support the execution of this project. The content of this section is dedicated to explain the current understanding of the problem which requires attention, the desired goal to be achieved and the proposed approach to deliver the results of the project.

1.2.1. Problem Statement

One of the requirements for viable ORC power systems is the possibility of designing efficient expanding devices for a wide range of possible working fluids and operating conditions. A vast amount of research has already been devoted to the design of RITs, however most of these efforts have focused on traditional applications. When the flow within the devices can reach supersonic conditions, as is usually the case when employed in the ORC using organic fluids, the design can become a much more complex task. Under these circumstances, the turbine stator can account for the majority of the losses, making the design of this component a critical aspect to consider.

Both traditional and modern design methodologies often require a certain level of existing empirical knowledge [20]. In practice, this usually entails choosing certain parameters in the preliminary phases of the design process. These choices can have an enormous impact on the final performance of the turbo-generator. It has been customary in turbomachinery design to condense design knowledge into mathematical models, or correlations, supported partially by, and in many cases purely based on, empirical results. However, the existing methods for small-scale turbines cannot easily be applied directly for unconventional applications; most models are developed for obtaining velocity triangles and sizing dimensions without consideration for the more complex details of the flow [21].

A small number of studies carried out in the past have already hinted the relevance of certain design parameters that could influence the efficiency of unconventional stator types [22, 23]. Despite this, similar attempts for more complex architectures have never been undertaken. For this reason, the preliminary design space of supersonic radial stators remains too large; both in terms of degrees of freedom and the range of possible values of these important parameters. Some of these can already be fixed at preliminary, and therefore mean-line, design level. Finding relevant guidelines for the design of unconventional RITs based on a sound physical understanding of the underlying loss mechanisms is an important research task which was until this moment left almost unattended by the scientific community.

1.2.2. Objective & Research Questions

In the present work the main objective was to *formulate preliminary design guidelines for supersonic radial inflow turbine stator vanes by studying the effect of relevant parameters on the blade's performance based on numerical computer simulations.*

This project aims to answer a set of steering research questions. These questions read as follows:

- (I) *What are the significant loss mechanisms affecting the performance and flow characteristics of radially inward supersonic stator vanes?*
- (II) *What are the important design parameters and the corresponding geometrical features which influence the relevant loss mechanisms?*

Definitions of blade behavior and performance will be given later on this report. Nevertheless, these questions are key to this research work and played an important role throughout the entire project. They should be kept in close consideration when going through the pages of this report; the cumulative knowledge attainable from answering the questions was the source of information used to achieve the project objective.

1.2.3. Original Contribution

This work is one of the first attempts to study unconventional RITs in a fundamental manner. This led to the execution of a parametric study specific for RIT stator vanes by means of multiple CFD simulations. Most of the relevant studies related to this field of research were carried out during a period when computational resources were much scarcer than nowadays. For this reason results produced from this work are therefore a novel addition to the scientific literature.

Similarly, the semi-automated computational framework produced to build and simulate the various blade configurations provides a solid base for future research. Several tools were developed, some based on existing code, built mainly using open-source software. With access to them, they can easily be extended and improved. Likewise, the results produced in this project should also be reproducible following the steps laid out in subsequent chapters of this report and new useful data could be attained by attempting to undertake the recommendations presented at the end of this report.

Finally, this project acquired an exploratory facet in which some very fundamental relations between the design parameters, geometrical features and performance have been established. The scope of the project needed to be iterated to adapt to the unexpected findings encountered during the experiments, which also limited the possibility of completing the original objective

to its full extent. Nonetheless, it led to other invaluable and unforeseen insights, which should provide enough motivation to continue this line of research.

1.3. Report Outline

Following this introductory chapter, this report has been structured in the following manner: chapter 2 will layout the theoretical knowledge gathered and used to develop a relevant hypothesis. Subsequently, chapter 3 will proceed to explain in detail the methodology employed to test the hypothesis resulting from the aforementioned theoretical analysis. In chapter 4 an application for the generic method is proposed, whereafter the results of the experimental tests are presented, followed by a discussion of the relevant findings. Finally, chapter 5 will contain the conclusions that could be drawn from the results accompanied by recommendations for researchers interesting in pursuing future work related to this topic.

2

Theoretical Background

This chapter contains the knowledge necessary to understand this project, gathered mainly through the study of scientific literature. There are several core topics important to this research project, which in broad lines include gas dynamics, thermodynamics and turbomachinery. An extensive treatment of all the fundamental subjects related to this research cannot be provided in this report. However, readers interested in pursuing a better understanding of this theoretical knowledge are encouraged to review some of the sources used to gather the content present in this chapter.

2.1. Radial Turbine Architecture & Design

This section will present information regarding the important architectural features and design techniques used for both traditional and unconventional radial turbines.

2.1.1. Traditional Configurations

A small scale ORC expander realized in the form of a RIT was depicted in the previous chapter in Figure 1.2. To understand the workings of such a device, it is useful to first review the fundamental theory behind them. Figure 2.1 contains schematic diagram of a conventional single stage RIT, which will serve as a basic reference for the analysis in the subsequent sections.

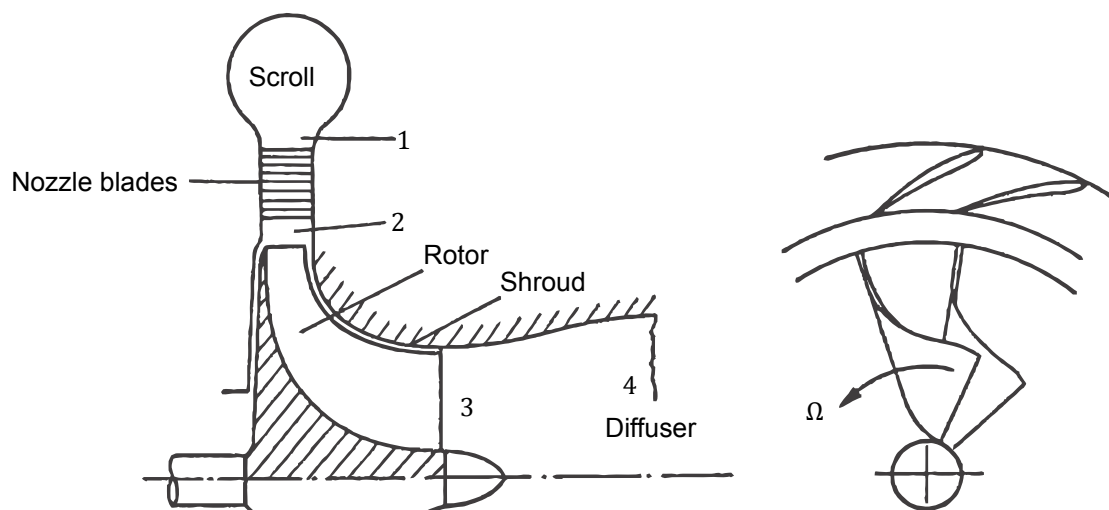


Figure 2.1: Schematic layout of a traditional RIT. Adapted from [8]

The basic structure of such a turbine consists of a stationary set of vanes, called the stator and the collection of rotating blades that generate mechanical power, also known as the rotor. In order to extract useful energy from the working fluid, its velocity must be increased in the stators, which act as nozzles; a basic component in fluid-dynamic systems which consists of a duct with a change in cross-sectional area. The gradual area change accelerates the fluid at the expense of its potential (pressure) energy.

The adiabatic expansion occurring within the turbine present in Figure 2.1, can be modeled thermodynamically and the process can be expressed using an enthalpy-entropy chart (Mollier diagram). A generalized version of such a diagram can be found in Figure 2.2. The diagram's convenience is that it presents visual information linking the enthalpy h and the entropy s of the fluid at the different states in the stage. The former property is directly related to the work produced by a process, while the latter can be associated with the losses in a system. Other important parameters shown in the diagram are U , u and u_{rel} , the tangential, normal and relative components, respectively, of the fluid velocity at different stations in the machine. These are frequently referenced in the velocity triangle analysis commonly used to design turbines.

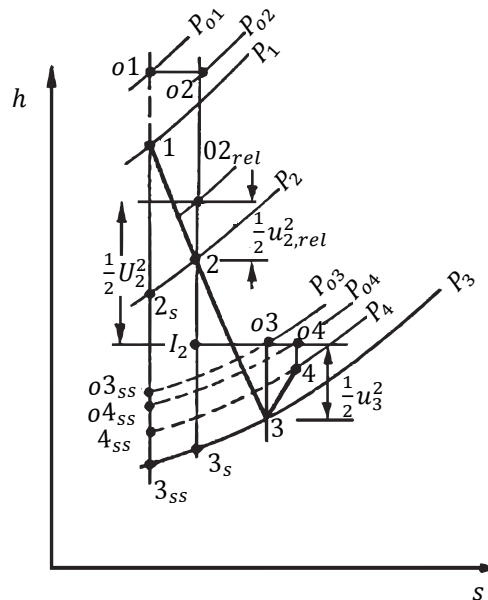


Figure 2.2: Mollier diagram of a typical RIT at design point. Adapted from [8]

The goal when designing a turbine is to attempt to make the real expansion, modelled by the line 1 – 3 to resemble the corresponding isentropic process, represented by line 1 – 3_{ss}. It can be observed that this expansion consists of two segments, namely 1 – 2, corresponding to the stator, and 2 – 3, corresponding to the rotor. The design of both components will therefore play a role in the overall efficiency of the machine.

2.1.2. (Unconventional) Highly Supersonic Operation

Traditionally, turbomachinery was designed mainly for low Mach number regimes, where the assumption of incompressible flow can be applied without a substantial loss of accuracy. However, the search for ever increasing performance has gradually pushed the designs well over the sonic flow limits. In components with internal flows reaching supersonic velocities, choked flow conditions and compressibility will play a major role in the analysis and substantially increase the design complexity. These issues are mainly caused by the appearance of shock discontinuities, which can lead to a large decrease in the overall efficiency of the turbine.

For plane nozzles, a C-D duct is required to achieve $M_2 > 1$. However, when applying

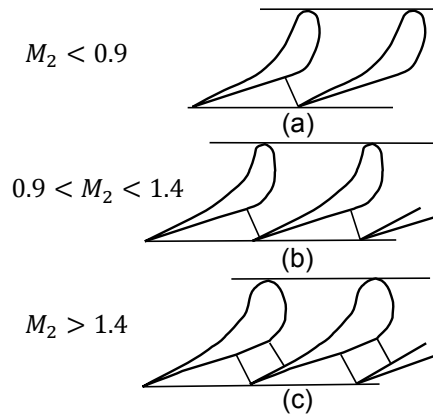


Figure 2.3: Shape and profile of blades employing different nozzle types according to the application. (a) Convergent nozzle for subsonic cascade (b) Convergent nozzle for transonic cascade (c) C-D channel for high supersonic velocities. Adapted from [23]

the concept in turbine cascades, an alternative solution can be found, by adopting a purely converging bladed channel and allowing the flow to reach supersonic speeds through an after-expansion process in the semi-bladed region downstream of the throat. For $M_2 < 1.4$, this is the recommended design topology. However, for higher Mach numbers, the post-expansion process involves strong shocks and the resulting flow deviation can be large enough to render converging cascades inefficient [9]. A comparison between the types of possible blade configurations can be found in Figure 2.3.

Convergent-Divergent Nozzles

Given the main purpose of stator blades in turbomachinery equipment, as previously mentioned, their design must resemble nozzle geometries. Accelerating a fluid in a subsonic state will require decreasing the cross-sectional area, as the velocity of the fluid must increase for the mass to be conserved in the system. However, once the flow approaches a Mach number of unity, the fluid accelerates by a different mechanism; the cross-sectional area must be increased.

When the flow exiting the stator is expected to reach such conditions, as is typically the case for single stage RIT operating in a ORC, this fundamental concept must be taken into account. Hence, a supersonic nozzle will consist first of a convergent section followed by a divergent section, and the minimum cross-sectional area, usually referred to as the throat, is where the flow will reach supersonic conditions. An example of such a C-D geometry is shown in Figure 2.4.

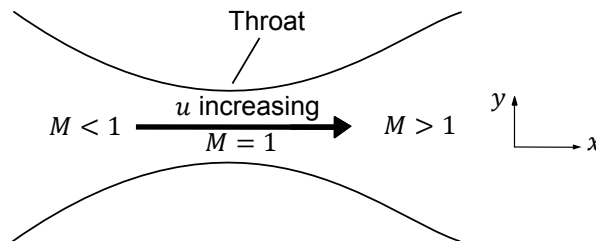


Figure 2.4: Schematic diagram of a generic C-D (supersonic) nozzle. Adapted from [24]

Where u refers to the fluid's velocity in the horizontal (x) direction. For such a nozzle, the outlet Mach number for isentropic conditions is given by the well-known Mach-area relation, an expression which can be derived by performing a quasi-one-dimensional analysis of nozzle flow and has the form

$$\frac{A}{A^*} = \frac{1}{M^2} \left[\frac{2}{\gamma + 1} \left(1 + \frac{\gamma - 1}{2} M^2 \right) \right]^{\frac{\gamma + 1}{\gamma - 1}}, \quad (2.1)$$

where the asterisk denotes properties at sonic conditions, γ is the ratio of the specific heat capacities, represents the effects of the fluid on the expansion process. M is the Mach number of the fluid at any specific (x, y) coordinate and A represents the (one-dimensional) cross-section of the nozzle. The significance of Equation 2.1 is that for a given expansion process, M will solely be defined between the ratio of the outlet and throat areas. For such a system, only one supersonic solution exists where the fluid expands from given initial conditions to an imposed back pressure. Other expansion ratios will result in over- or under expanded solutions which will lead to the appearance of expansion fans or discontinuities, increasing the entropy production in the system.

Nozzle Design: Method of Characteristics

The isentropic modelling approach described above is useful and simple method for making preliminary calculations and understanding the underlying physics behind supersonic nozzles. On the other hand, it gives no information on the suitable wall outline for such nozzles.

A more advanced technique, known as the Method of Characteristics (MoC) can provide the information missing from a quasi-one-dimensional analysis. *Characteristic lines*, is the name given to the set of points in x, y space along which the derivatives of the flow-field variables are indeterminate [24]. Usually, lines extending in the positive vertical direction are called positive characteristics and in the same way, lines going in the opposite direction are described as negative characteristics. A thorough account of this theory is out of the scope of this report, see [24, 25] for more details.

In the Two-dimensional (2D) flow in Figure 2.5, used as visual guide, the flow properties are a function of x and y . This type of 2D flow can represent the actual conditions of a range of simple supersonic nozzles.

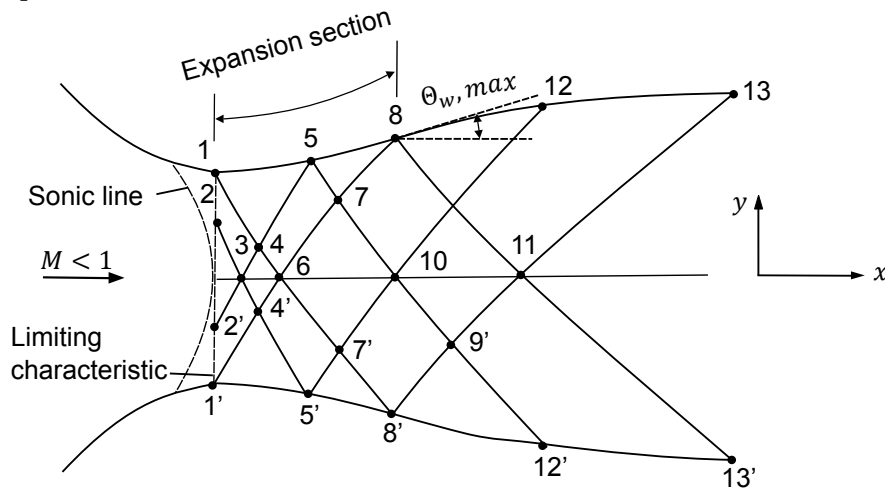


Figure 2.5: Schematic diagram of supersonic nozzle contour designed using the method of characteristics. Adapted from [24].

Consider the case when a C-D nozzle will be employed to expand a gas from rest to a desired supersonic Mach number M_a at the exit. The subsonic section, which will be convergent in nature, will have less strict requirements regarding the shape of its contour. Due to the predominant 2D behavior of the flow in the throat region, the sonic line is generally curved. A line called the limiting characteristic is defined at a location such that any characteristic line emanating from this boundary can intersect the sonic line. To commence a MoC solution, an initial data line downstream of this location must be known [24].

It is then assumed that the values at all points on the limiting characteristic can be determined by independent calculation of the flow conditions, making it the initial data line. An example of such a method is the one proposed by Sauer [26] to solve the subsonic-transonic problem using perturbation theory. Allowing θ_w denote the angle between a tangent to the wall and the horizontal, the section of the divergent region of the nozzle where this angle increases in value is called the expansion section. The end of this section is marked by $\theta_w = \theta_{w,max}$ (point 8 on Figure 2.5) [24].

Downstream of this point, θ_w decreases until it equals zero, demarcating the nozzle exit. The part of the contour between point 8 and the exit is called the straightening section and has less rigorous requirements in terms of shape [24].

Applying the MoC to an initial set of conditions and a desired M_a (or total-to-exit pressure ratio) provides a suitable contour for a nozzle to facilitate the expansion of a fluid.

Stator Design

Reasons for arguing that designing supersonic radial inflow stators requires unconventional methods have been presented in the previous sections. Nonetheless, proposals for such methods are scarce in the literature [17]. Due to the complexity of the flow behavior present in these components under such operating conditions, the trend in research in the past years has been to resort to CFD-based optimizations.

Recently, work in this line of work has demonstrated the potential of coupling CFD simulations to intelligent optimization procedures, thereby improving the performance of the mean-line geometry of turbo-machinery components [27]. Although encouraging results were obtained, its computationally intensive nature makes it a costly method to explore the preliminary design space. Similarly, the lack of understanding of the underlying physics of the processes occurring inside unconventional turbines limit the generalized usability of the designs.

A different approach, based on flow physics, is to start from a nozzle constructed on the solution of the MoC. Such a strategy has recently been successfully developed, extending the original method to account for NICFD [10]. To compare the effectiveness of different methods, the resulting Mach and pressure gradient contour plots from CFD simulations of stator vanes designed using traditional methods, CFD-based optimizations and the MoC method are presented in Figure 2.6.

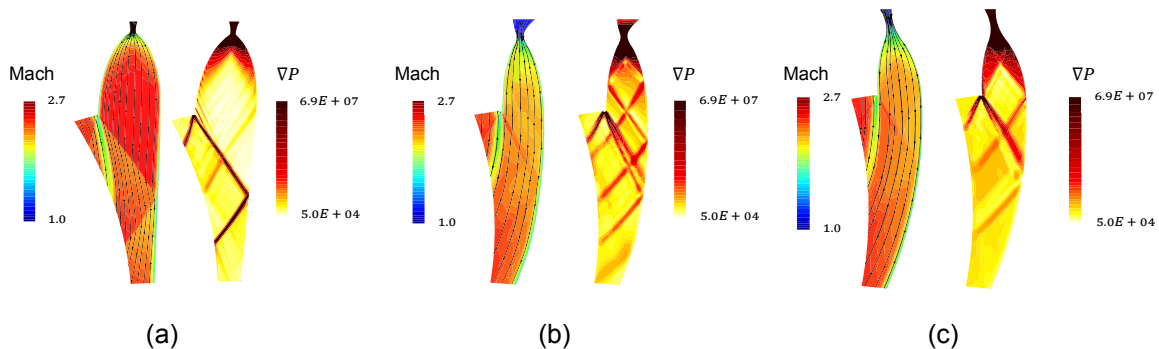


Figure 2.6: CFD results of Mach number (left images) and pressure gradient (right image) contours of stators designed using different methods. (a) Base design (b) CFD-based optimization (c) MoC-based design. Adapted from [10].

Although only a basic qualitative analysis can be done using the plots in Figure 2.6, what is important to extract from these images is the reduction in the number of shock-waves (dark red lines on the pressure gradient contours) as well as an increase in the flow uniformity (regularity of the streamlines at the exit on the mach contours) achieved by utilizing unconventional methods. This can lead to assert that a physics-based model can accomplish similar results to CFD-based optimizations, while being computationally inexpensive.

Despite the MoC-based design strategy showing a substantial improvement in the performance of the preliminary design of stator blades, it was found that the method on itself cannot guarantee the optimal fluid-dynamic behavior of an arbitrary configuration. The method requires some initial inputs to carry out the calculations, for which the optimal value must be known. In other words: the method will provide the best geometry of a certain configuration for the given inputs, but it will only deliver the optimal design when the provided inputs belong to the optimum.

2.2. Turbomachinery Performance

One of the main goals when designing turbomachinery is achieving the highest efficiency possible. As already stated in the previous section, this can be roughly summarized as attempting to produce an expansion process as close to the theoretical ideal as possible. In practice however, this task can be extremely complex and require immense knowledge and time to be accomplished; the following subsections provide a glimpse of this reality.

Traditional turbomachinery refers to the devices having classical architectures, and using well understood fluids such as air or water. The operating conditions for these machines is usually in the subsonic regime and they have already been extensively studied and improved in the past; a vast amount of knowledge on how these machines work and what affects their performance is available. An example of such knowledge is the theory of the loss causing characteristics of internal flows.

It has been customary to breakdown the losses in traditional turbomachinery into three main broad categories: “profile loss”, “end-wall loss”, and “leakage loss”. This categorization is still widely used although it is nowadays clearly recognized that due to the complex behavior of the internal flows, the loss mechanisms are rarely independent. However, using this categorization can simplify the problem of losses and provide insights for useful strategies to mitigate them.

Profile loss is usually considered to be the loss produced in the blade boundary layer at a vast distance from the end walls. It is frequently assumed that the flow exhibits planar behavior (i.e. 2D), so the loss predictions may be based on 2D cascade tests or boundary layer calculations. The additional decrease in performance arising at the Trailing edge (TE) is usually lumped together with the profile losses [28].

End-wall losses are often referred to as “secondary” loss because they in part emerge from the secondary flows generated when annulus boundary layers traverse a blade row. However, it is important to note that the loss is not a direct effect of the secondary flows but arises from a combination of several factor. Moreover, it is oftentimes difficult to distinguish end-wall losses from profile losses and leakage loss. Additionally, the title “secondary loss” is sometimes used to refer to all the losses that otherwise cannot be explicitly accounted for [28].

Tip leakage loss originates from the leakage of fluid over the tips of rotor blades and the hub clearance of stator blades. The details of the loss mechanisms depend strongly on whether the blades are shrouded or not. The interaction between end-wall loss and leakage loss may be substantial [28]. A diagram summarizing the categorization of the aforementioned losses can be visualized in Figure 2.7.

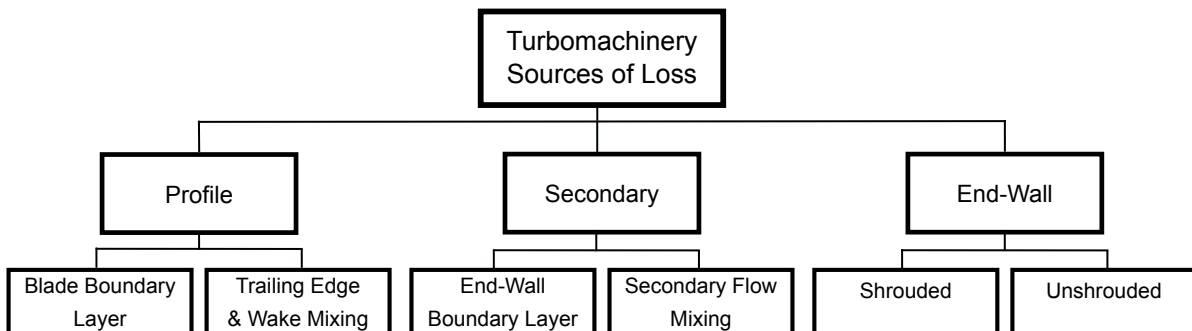


Figure 2.7: Diagram summarizing classification of loss characteristics in turbine. Adapted from [29]

Given the fact that this research project focused on the preliminary design stages of turbines, most of the analysis will be based on 2D mean-line geometries. In this context, secondary and end-wall losses, which are predominantly three-dimensional in nature and occur mainly far away from the blade mean-line, can be neglected. It can also be intuitively determined by observing the planar shape of the blades (cf. for example Figure 1.2 that the main loss mechanisms should remain constant along the z-plane. For these reasons, this work will mainly be considering profile losses and its effect on turbine performance.

2.2.1. Loss Accounting

When studying losses, the ability to quantify and account for all the relevant loss mechanism is critical. In turbo-generators, the isentropic efficiency is defined as the ratio of the actual work output to the theoretical isentropic work. Referring to Figure 2.2 this parameter can be expressed mathematically as

$$\eta = \frac{h_1 - h_2}{h_1 - h_{2s}}, \quad (2.2)$$

for stator stages specifically. This is arguably the most important metric in determining the performance of turbines. However, because enthalpy cannot be measured directly, determining this parameter is not always a straightforward process. For this reason dimensionless ratios, better known as loss coefficients, have been developed by scientists and designers to determine performance in more practical ways. There are various definitions of loss coefficients commonly used for individual blade rows, some of which have different variations depending on the application. For the sake of clarity, the chosen definition of the most important coefficients have been gathered below.

Due to its definition, the only factors that can influence η are deviations from isentropic behavior. These may be caused either by heat transfer or to irreversible thermodynamic processes. For most machines the flow closely assimilates adiabatic conditions and therefore only entropy creation due to irreversible behavior can contribute significantly to loss of efficiency [30].

For this reason, it can be concluded that only entropy generation can be considered a rational measure of loss under adiabatic conditions. Any irreversible flow process creates entropy and so inevitably leads to a reduction in isentropic performance. It should therefore be common practice to define loss coefficients of individual row losses in terms of entropy rather than stagnation pressure or kinetic energy loss. Entropy production is a convenient measure, because unlike other physical properties, its magnitude does not depend on the chosen frame of reference.

For adiabatic flow through a stationary blade row, stagnation temperature is constant and so entropy changes depend only on stagnation pressure changes via

$$\Delta s = -R_g \ln\left(\frac{P_{o2}}{P_{o1}}\right), \quad (2.3)$$

where R_g is the gas constant, and the other variables use the same nomenclature as present in Figure 2.2. For small changes in stagnation pressure this becomes

$$\Delta s = -R_g \left(\frac{\Delta P_o}{P_o}\right), \quad (2.4)$$

hence for stator blades and cascade flows loss of stagnation pressure can be taken to be synonymous with increase in entropy [30]. An entropy loss coefficient can be defined by

$$\zeta_s = \frac{T_2 \overline{\Delta s}}{\overline{h_{o2}} - \overline{h_2}}, \quad (2.5)$$

where T represents the temperature at which the process occurs and the overline denotes the average value of the parameter at a given location. Nonetheless, a simpler version which can be implemented in calculations more easily is

$$s_{gen} = \frac{\overline{s_{out}} - \overline{s_{in}}}{\overline{s_{in}}}, \quad (2.6)$$

In the case of stator vanes, the frame of reference remains constant, reducing the relative importance of entropy production as method of accounting for losses. Moreover, it has been found in previous studies based on numerical simulations that all the relevant loss coefficients present similar trends with respect to performance [31]. These considerations provide some arguments for the possibility of employing other well-known coefficients.

Possibly the most widely used is the stagnation pressure loss coefficient; referring again to Figure 2.2 this is defined by

$$\zeta_p = \frac{P_{o1} - P_{o2}}{P_{o2} - P_2}. \quad (2.7)$$

Likewise, the kinetic energy loss coefficient is also among one of the popular loss coefficients, and is usually defined as follows

$$\zeta_k = \frac{\bar{h}_2 - \bar{h}_{2s}}{(\bar{u}_{2s})^2}, \quad (2.8)$$

where u is the fluid velocity.

Finally, another common and conceivably more appropriate loss coefficient for design purposes is the energy or enthalpy loss coefficient, defined as

$$\zeta_h = \frac{\bar{h}_2 - \bar{h}_{2s}}{\bar{h}_{o2} - \bar{h}_2}. \quad (2.9)$$

All of the definitions presented above are relevant when studying turbomachinery performance and can be therefore used for the loss bookkeeping of radial stator stages.

2.2.2. Two-Dimensional Loss Mechanisms in Turbine Vanes

Due to the planar nature of the stator geometry in RITs, such as the one present in Figure 1.2, out of the main loss categories present in the introduction of this section, profile losses will be the focus of this work. As briefly stated in the introduction of this section, these losses are related to the dissipation of energy on the blade surfaces far enough from the end-wall.

This group can be broadly subdivided between the viscous dissipation occurring mainly in the blade boundary layer, and the mixing losses occurring at the TE and the wake of the blades, where flow discontinuities such as shocks can appear. This last subcategory may include the effects of the possible interaction between shocks and boundary layer.

Boundary Layer Losses

Viscous dissipation usually confines itself to a region near the walls enclosing the flow known as boundary layer. Assuming turbulent conditions on a blade surface, such as the one shown in Figure 2.8, an expression can be derived for the rate of change of entropy flux in a 2D boundary layer as [30]

$$\dot{s}_{irr} = \frac{d}{dx} \int_0^\delta \rho u (s - s_\delta) dy, \quad (2.10)$$

which would be a direct measure of the loss generated in the area. Here ρ is the fluid density and δ represents the thickness of the boundary layer, which is defined as the limit where the fluid velocity is 99% of the free stream value.

For practical use, it is convenient to turn the entropy production rate into a dimensionless dissipation coefficient, which is defined by [30]

$$C_d = \frac{T \dot{s}_{irr}}{\rho v_{ref}^3}, \quad (2.11)$$

where T is the temperature at which the process is taking place. The exact magnitude of the dissipation coefficient cannot be calculated without knowing full details of the state of the boundary layer. However, correlation of much experimental work has led to some general results [30]. It has been suggested that for several turbomachinery blades where the boundary layer is turbulent, a reasonable approximation is to take [33]

$$C_d = 0.002 = const. \quad (2.12)$$

It is still important when making this assumption to take into consideration that there can be a substantial difference between laminar and turbulent boundary layers. It should also

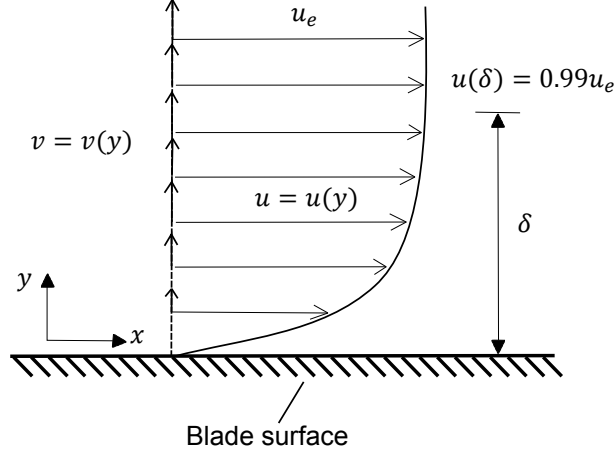


Figure 2.8: Schematic diagram of a turbulent boundary layer in a blade surface. Adapted from [32]

be noted that there are no known results for the effect of Mach number on the dissipation coefficients.

Making use of the definition of the kinetic energy loss coefficient in Equation 2.8, the losses due to viscous dissipation in a boundary layer can be expressed as

$$\zeta_{k,BL} = \frac{\dot{m}\Delta h}{\frac{1}{2}\dot{m}u_{ref}^2} = \frac{\dot{m} \int T ds}{\frac{1}{2}\dot{m}u_{ref}^2} = \frac{\int T \dot{m} ds}{\frac{1}{2}\dot{m}u_{ref}^2} = \frac{\int T \dot{s}_{irr}}{\frac{1}{2}\dot{m}u_{ref}^2} = \frac{\int C_d \rho u_\delta^3}{\frac{1}{2}\dot{m}u_{ref}^2}, \quad (2.13)$$

where \dot{m} is the mass flow in the system.

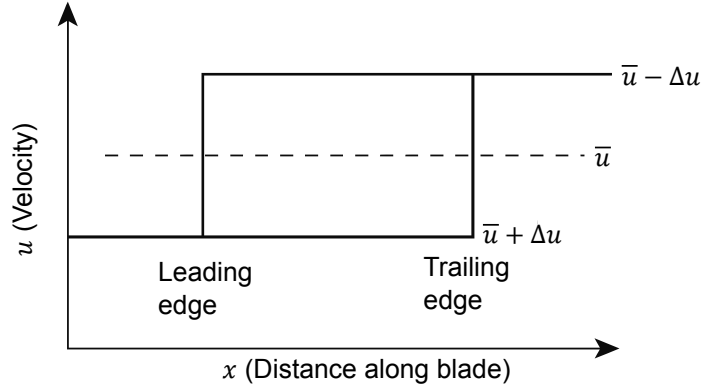


Figure 2.9: Idealized flow distribution along blade. Adapted from [34]

Assuming incompressible flow and a rectangular (idealized) velocity distribution, as the one shown in Figure 2.9, the numerator in Equation 2.13 can be written as

$$\int C_d \rho v_\delta^3 = C_d \sum_{PS+SS} \int_0^1 \rho u_\delta^3 d\left(\frac{x}{C}\right) = C_D \rho C (2\bar{u}^3 + 6\bar{u}\Delta\bar{u}^2), \quad (2.14)$$

where C is the blade chord and PS , SS refer to the suction and pressure side respectively. This therefore converts Equation 2.13 into

$$\zeta_{k,BL} = \frac{C_D \rho C (2\bar{u}^3 + 6\bar{u}\Delta\bar{u}^2)}{\frac{1}{2}\dot{m}\bar{u}^2} = \frac{C_d \rho (2\bar{u}^3 + 6\bar{u}\Delta\bar{u}^2)}{\frac{1}{2}\dot{m}\bar{u}^2} \frac{C}{L}, \quad (2.15)$$

where L is the pitch length of a blade. Equation 2.15 predicts that the viscous losses on the blade walls will be a function of the velocity profile, as well as the mass flow in the system and the ratio C/L , also known as the blade solidity.

Lastly, it has been found through analytic studies of viscous losses [35] that the throat Reynolds number, defined as

$$Re_t = \frac{Ou_t}{\nu_o}, \quad (2.16)$$

where O is the throat width, subscript t denotes conditions at the throat and ν_o is the stagnation kinematic viscosity, can be related to the conditions of the blade-wall boundary layer.

Trailing Edge Mixing or Post-Expansion Losses

For turbine blades with thin TE operating under subsonic conditions, the trailing edge loss is often small compared to the viscous dissipation at the boundary layer and is usually neglected. However, when the exit Mach number approaches unity the loss coefficients increase sharply. The boundary layer losses frequently decrease with higher flow velocities, so the additional loss should be a consequence of the shock formations emanating from the trailing edge.

In general, the efficiency will continue to decrease with rising Mach numbers when the outlet flow is in the low supersonic regime ($M_2 < 1.2$), but for some type of blade, this trend may disappear and even reverse at highly supersonic exit flows [36].

The flow pattern at a supersonic trailing edge is been thoroughly studied and is well documented. The general features of the flow in the region has been sketched in Figure 2.10. The flow immediately after the trailing edge is a region where the fluid possesses a relatively low velocity at nearly uniform pressure. This pressure has been defined to be the base pressure [36].

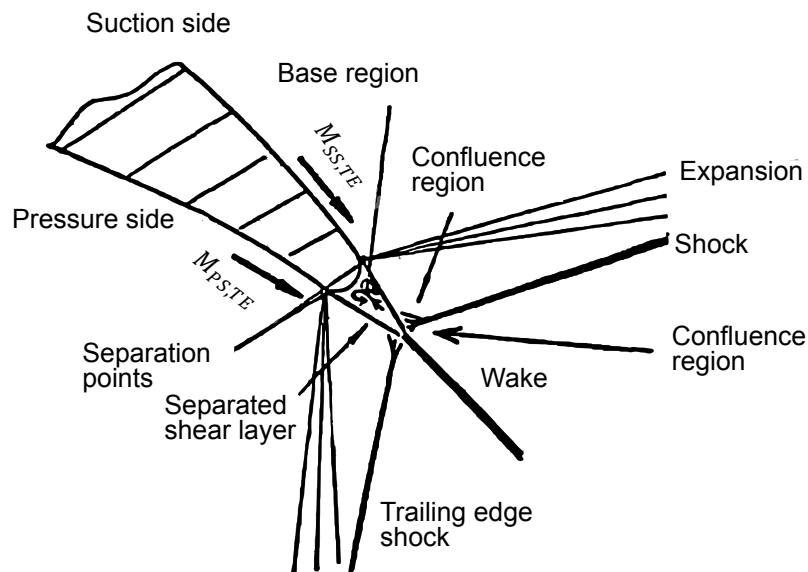


Figure 2.10: Supersonic flow structure around a blunt blade trailing edge. Adapted from [36]

Despite the basic aspects of the flow being well understood, the characteristics of the base pressure and its value are difficult to predict. Having determined the base pressure however, the resulting inviscid flow pattern can be constructed using techniques such as the MoC.

The losses generated in this region can then be obtained from a continuity, energy and momentum balance in the region between the trailing edge and a virtual mixed out uniform flow far downstream of the blade. Previous analyses have demonstrated that, ignoring local errors in the results, the Euler solutions can be effectively used for a correct quantification of the overall loss [36].

Considering the case of a cascade of staggered thick plates, as shown in Figure 2.11, can be useful to determine the relevant geometrical parameters influencing the trailing edge losses.

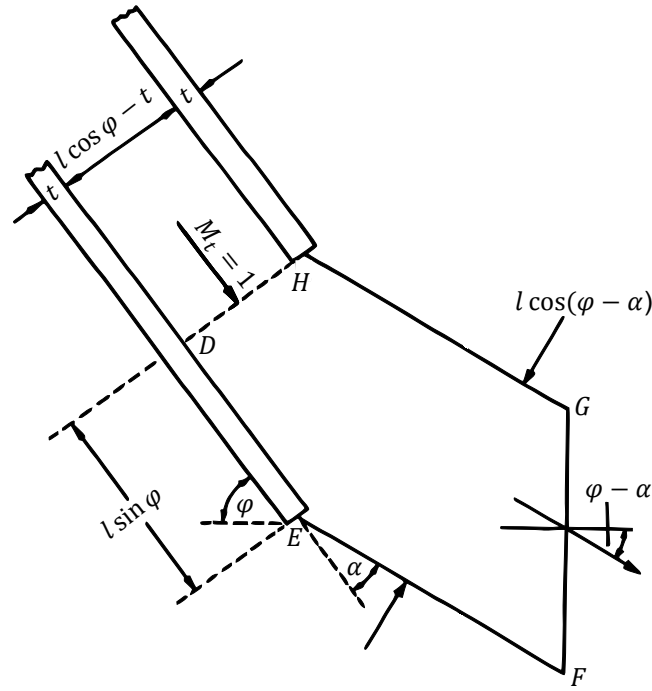


Figure 2.11: Schematic diagram of staggered plates with control volume for trailing edge analysis. Adapted from [36]

In this diagram, l is the gap between the plates (analogous to the pitch length L in actual turbine blades) and t is their thickness. The stagger angle is φ and the deviation angle is α . Plane GH refers to a theoretical surface far downstream of the cascade with a uniform flow profile. On the other hand, lines FG and HI , representing surfaces, are periodic boundaries whereby all pressures and fluxes would cancel each other out [36].

Assuming the flow in the channel between the plate walls to be choked and uniform, the surface boundary layers can be neglected for this analysis. A consequence of the choked flow condition is that the mass flow is fixed throughout the system, which allows the following conservation equations to be derived [36]

$$\frac{\dot{m}\sqrt{c_p T_o}}{(l \cos \varphi - t)P_{o1}} = f(1) = \text{const.}, \quad (2.17)$$

$$\frac{\dot{m}\sqrt{c_p T_o}}{(l \cos(\varphi - \alpha)P_{o2}} = f(M_2), \quad (2.18)$$

where c_p is the isobaric heat capacity. Dividing Equation 2.17 by Equation 2.18 leads to

$$\frac{P_{o2}}{P_{o1}} = \frac{f(1)(l \cos \varphi - t)}{f(M_2)l \cos(\varphi - \alpha)}, \quad (2.19)$$

a result which directly relates the losses in a staggered cascade of blades with the mixed out exit Mach number and the ratio between the throat and exit areas.

(Isolated) Wake Mixing

A similar analysis can be carried out for the wake mixing losses, which will also be affected by the boundary layer formation and the flow behavior at the TE. It is useful to start by considering the unstaggered plates shown in Figure 2.12. Despite the configuration differing from an actual blade row, the model remains a useful fundamental study for reference purposes. In order to further simplify the analysis, the blade trailing edge has been assumed to be blunt in shape and incompressible flow theory has been assumed to be valid. Similarly, station (2) represents an area where the flow has reached a fully mixed-out state.

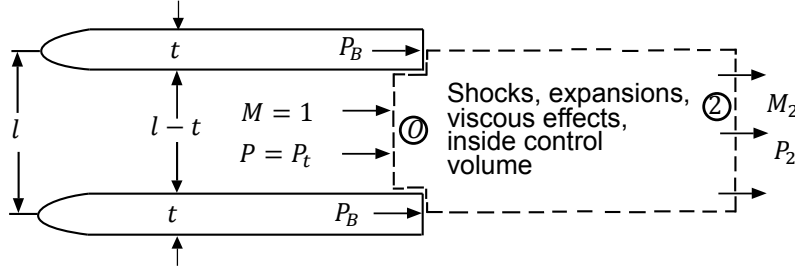


Figure 2.12: Schematic diagram of unstaggered plates with a proposed control volume. Adapted from [36]

The dashed area shown in Figure 2.12 can be taken as a control volume. In such a case the balance equations can be determined, starting from a mass balance

$$\rho_1 u_1 (l - t - \delta) = \rho_2 u_2 l, \quad (2.20)$$

where δ refers to the boundary layer thickness already presented in Figure 2.8. Following with a momentum balance

$$(l - t)P_1 + tP_B + \dot{m} - \rho_1 u_1^2 \varphi = lP_2 + \dot{m}u_2, \quad (2.21)$$

where φ is again to the geometric deflection angle, which is added to extend the analysis for more general blade configurations. Then defining a base pressure coefficient

$$C_{P_B} = \frac{P_B - P_1}{\frac{1}{2}\rho_1^2 u_1^2}. \quad (2.22)$$

Equation 2.22 can then be rearranged to get

$$(P_1 - P_2) = -\rho u_1^2 \left(1 - \frac{t}{l} - \frac{\delta}{l} - \frac{\varphi}{l}\right) + \rho u_2^2 + (P_1 - P_B) \frac{t}{l}, \quad (2.23)$$

and finally, after some manipulation

$$\frac{P_{o1} - P_{o2}}{\frac{1}{2}\rho_1^2 u_1^2} = \frac{u_2^2}{u_1^2} - 1 + 2\left(1 - \frac{t}{l} - \frac{\delta}{l} - \frac{\varphi}{l}\right) - C_{P_B} \frac{t}{l}, \quad (2.24)$$

which can also be rewritten as the stagnation pressure loss coefficient [32] using the definition of Equation 2.7

$$\zeta_{P,mix} = -C_{P_B} \frac{t}{l} + \frac{2\varphi}{l} + \left(\frac{\delta + t}{l}\right)^2. \quad (2.25)$$

By taking l to be analogous to L , Equation 2.25 shows that the losses due to the contribution of the wake mixing will be proportional to the TE-thickness-to-pitch-length ratio and to the state of the boundary layer. The latter can also be quantified by Re_t for more complex geometries such as turbine blades.

2.2.3. Unconventional (Radial) Losses

Similar to traditional turbines, the goal when designing unconventional turbines is to provide power with the highest efficiency possible. Although these atypical architectures are intrinsically more complex, the basics covered in the previous section generally remain relevant for this type of devices. Nevertheless, for an accurate prediction of the losses, the analysis needs to be extended to take other more intricate concepts into account; these will be covered in the remaining of this chapter.

Loss Distribution

In recent years, it has been possible to replace expensive tests using actual turbomachinery with experimental computer simulations. This has been possible both due to the ever expanding availability of computing power and the increasing accuracy of CFD solvers.

The trend of losses in generic turbo-generators for the most common and traditional configurations are known from years of practical applications. These trends generally predict a high concentration of the losses in what could be considered the rotor stage. It should be noted, however, that these results are generally not representative for machines operating in transonic or supersonic flow regimes.

For these reasons, attempts to replicate the operation of supersonic turbines have been undertaken. The unsteady simulation carried out in [16] is an interesting case study, as the authors not only calculated the entropy generation of a complete radial turbine stage, but also sought to perform a break-down of the losses and to portray a detailed profile of its distribution along the different components. The most relevant illustration of these results can be found in Figure 2.13.

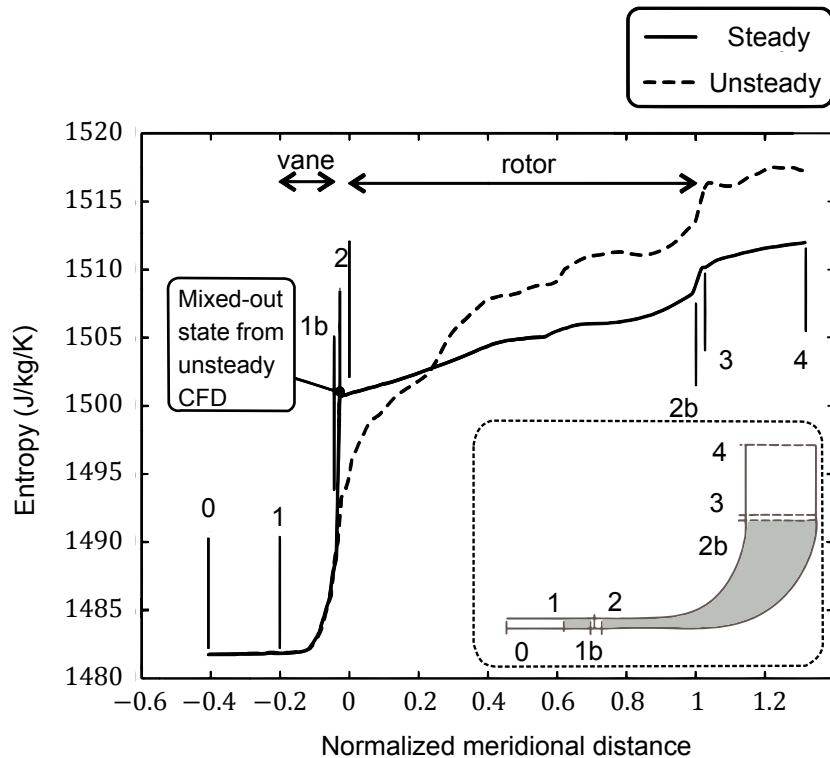


Figure 2.13: Predicted increase in mass-averaged entropy along meanline distance for a test case, for steady and unsteady simulations. Adapted from [16]

In the figure, the mean-line mass-average entropy for both the steady and unsteady simulation of a supersonic turbine has been plotted against the normalized meridional distance of the turbine, while marking the limit of each component along this variable.

Although these results are for a specific turbine configuration, there are two general and relevant considerations that can be made. Firstly, it can be observed that for a supersonic turbine, the majority of the entropy will be produced in the stator vanes, between stations 2 and 4 in the figure. Second, a mixed-out steady state simulation of the flow can conservatively predict the entropy production in the stator stage of the vane.

These findings are relevant because they highlight the importance of the stator design in the context of supersonic turbines. This result was found without even quantifying the effect of the flow exiting the stator on the rotor losses. Taking aside the fact that losses from the stator will travel downstream and possibly magnify in the process, the uniformity of the flow incident on the rotor should also be considered.

Although flow uniformity cannot be directly attributed to lower entropy production [34], intuition points out that a well-designed stator will provide the rotor with better operating conditions. Consequently, as opposed to traditional turbines, the design focus will shift from

the rotor towards the stator.

Flow Structure & Behavior

Approaching the losses using control volumes, the core technique employed in the analysis presented in subsection 2.2.2 is a useful method to unravel the relevant parameters influencing the performance of turbomachinery blades. However, for more complex or unconventional application, such as C-D radial stators, some relevant information can be left out during the analysis.

Some of these details can be determined by studying the flow structure within the blade channels. Unsteady CFD simulations of the operation of these type of devices can provide this information. A useful example is the successful attempt of such a simulation undertaken by [15].

An instantaneous pressure gradient contour resulting from this work is exhibited in Figure 2.14. Here both stator and rotor stages are shown, which also helps illustrate the influence of the stator on the rotor performance.

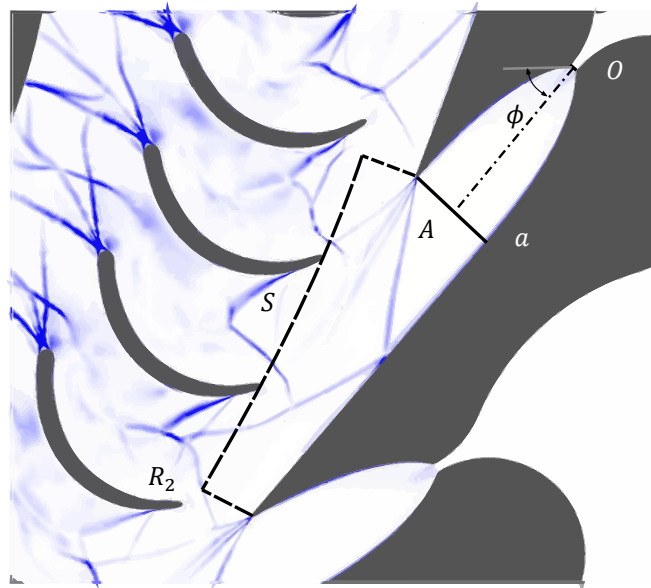


Figure 2.14: Instantaneous entropy generation rate of the unsteady simulation of a highly supersonic radial ORC turbine. Light shading represents minimum values and dark shaded areas are the maximum. Relevant variables have been added and the boundaries of the stator stage have been marked for reference purposes. Adapted from [15]

In Figure 2.14 the shocks are clearly visible as lines of darker shade (higher entropy production). The main features of the flow field characteristic of C-D stators can be identified; the trailing edge shocks are visible, as the theory in section subsection 2.2.2 had anticipated. The main oblique shock stemming from this region also reflects on the adjacent wall, where it heads downstream to the rotor. A strong shock incident on the blade wall can eventually lead to flow separation in this area, creating a more violent, and therefore less efficient, mixing in the stator wake.

Simulating the rotor together with the stator is a very useful exercise as it portrays how the loss generating mechanisms of the stator influence the rotor operation. It can be seen how some shocks and structures emanating from the stator TE interact with the rotor geometry, generating more discontinuities and less flow uniformity.

When the C-D section of the blade is designed correctly, the flow in this region should be shock free. Its performance should then be mainly influenced by viscous dissipation in the boundary layers. This can be visualized by observing the thin shaded lines along the blade walls.

An additional post-expansive process will then occur downstream of the nozzle in the semi-bladed region and the mixing plane, the area between the stator and the rotor. This

process will be dominated by heavy mixing from the TE, wake and possible interaction of the shocks with the boundary layer.

The C-D nozzle embedded in the channel between adjacent blades provides a degree of freedom in the design of C-D stators [10]. This comes in the form of the pressure ratio between the throat and nozzle exit. The effect of this parameter on the blade performance can however not be fully accounted for with a traditional analysis; these effects occur within the control volume.

This intermediate expansion ratio, controlled by the throat-to-nozzle-exit area ratio, has two simultaneous effects: it determines how much of the expansion will occur in the semi-bladed region and the mixing plane, the so called post-expansion, and it controls the velocity of the flow (by fixing the outlet Mach number), therefore determining the velocity profile of the blades. These effects will in turn affect the state of the boundary layer, the discontinuities at the TE and the conditions of the wake mixing.

Based on the nomenclature presented in Figure 2.14, the post-expansion can be given a mathematical definition

$$\beta_{PE} = \frac{P_a}{P_2}, \quad (2.26)$$

which will aid in quantifying its effects on the blade performance.

Moreover, as the nozzle expansion process is fixed by the area ratio O/A (and thereby implicitly by M_a), the total pressure ratio can be split into two main components as well

$$\beta_{tot} = \beta_a(M_a) \cdot \beta_{PE}, \quad (2.27)$$

where β_{tot} is the total-to-outflow pressure ratio defined as

$$\beta_{tot} = \frac{P_0}{P_2}. \quad (2.28)$$

When β_{tot} is assumed to be constant, Equation 2.27 can be rewritten as

$$\beta_{PE} = \frac{\beta_{tot}}{\beta_a(M_a)} = f(M_a), \quad (2.29)$$

which can be used as the argument to quantify the performance and behavior of the blades based on the post-expansion ratio.

The importance of the amount of post-expansion in these type of blades has already been remarked in the literature [22, 23], in which guidelines for determining the optimal value of M_a based on its resulting degree of post-expansion in stator blades have been derived. However, these results are mainly focused on supersonic convergent axial architectures. For that specific case, it has been concluded that achieving no post-expansion will result in optimal designs. There are however no further accounts of this type of research related to radial C-D stator blades.

2.3. Research Hypothesis

An overview of the fundamental theory of RITs and their most relevant loss mechanisms has been presented in the previous sections of this chapter. As already mentioned, planar losses are the main group of loss mechanisms taken into consideration in the analysis. Similarly, strong reasons to assume that 2D steady simulations could conservatively used to predict the performance of these blades have been given.

In order to answer the posed research question, it is however necessary to take the generalized analysis a step further. Based on the information gathered in this chapter, it is possible to relate the important parameters of a radial stator blade to its performance.

It has been stated that the main contributors to reductions in efficiency will be the viscous dissipation occurring at the boundary and mixing losses primarily arising in the wake and Post-expansion (PE) region. In this last group, a detailed look at the flow structure revealed that shock-wave and shock-boundary layer interaction are expected to play a dominant role.

Taking a general ζ , which can be based on any of the previously presented definitions in subsection 2.2.1, the stator losses can then be divided into what is expected will be its two main components. This can be expressed mathematically as follows

$$\zeta_{stator} \approx \zeta_{2D} \approx \zeta_{visc} + \zeta_{PE}. \quad (2.30)$$

Given that all the expressions present in subsection 2.2.2 are non-dimensional, similarity analysis can be used to assume the conditions found in the fundamental examples can be extended to more specific cases. It is useful to then consider each of the components separately and determine the parameters which should influence the value of the corresponding loss coefficients.

Starting with the viscous term, Equation 2.15 and Equation 2.16 reveal that the relevant parameters expected to influence the viscous losses in the boundary layer are the velocity profile, blade solidity, throat Reynolds number and mass flow in the system. ζ_{visc} can therefore be written as a function with the relevant arguments as

$$\zeta_{visc} \approx f(\Delta u, \frac{C}{L}, \dot{m}, Re_t). \quad (2.31)$$

Assuming the velocity profile is directly proportional to the nozzle exit Mach number, which in turn, as can be deduced from Equation 2.1, should be a function of the relevant area ratio, gives

$$\Delta u \approx f(M_a(\frac{O}{A})). \quad (2.32)$$

Inserting Equation 2.32 into Equation 2.31 will lead to

$$\zeta_{visc} \approx f(M_a, \frac{C}{L}, \dot{m}, Re_t). \quad (2.33)$$

In a similar way, the loss coefficient related to the PE losses can be derived. The fundamental analysis led to the derivation of Equation 2.19 and Equation 2.25. Hence, the ratio of the area lengths O and A are expected to be directly involved in the development of the flow behavior, in this due to its control over the nozzle exit Mach, which will determine the strength of possible shocks forming at the TE.

Moreover, the the gauging angle, the ratios of throat-to-outflow and TE-thickness-to-pitch areas and the state of the boundary layer (which for simplicity will be represented by the throat Reynolds number) are also appearing as influential variables in the equations. Therefore the relevant component of these losses can be written as

$$\zeta_{PE} \approx f(M_a, \frac{O}{S}, \phi, \frac{t}{L}, Re_t). \quad (2.34)$$

Yet, as the throat-to-outflow area ratio can be split into

$$\frac{O}{S} = \frac{O}{A} \cdot \frac{A}{S} \quad (2.35)$$

and as the ratio $\frac{O}{A}$ already appears implicitly in the term M_a , Equation 2.34 can also be presented as

$$\zeta_{PE} \approx f(M_a, \frac{A}{S}, \phi, \frac{t}{L}, Re_t). \quad (2.36)$$

By inserting Equation 2.33 and Equation 2.34 into Equation 2.30, leads to a generalized expression of the stator losses with all the arguments which are expected to be relevant

$$\zeta_{stator} \approx \zeta_{visc}(M_a, \frac{C}{L}, \dot{m}, Re_t) + \zeta_{PE}(M_a, \frac{A}{S}, \phi, \frac{t}{L}, Re_t). \quad (2.37)$$

Moreover, assuming constant throat conditions and fixed blade dimensions allow to simplify the expression further to

$$\zeta_{stator} \approx \zeta_{visc}(M_a) + \zeta_{PE}(M_a). \quad (2.38)$$

From Equation 2.38 follows that the nozzle design Mach number is expected to be the only remaining degree-of-freedom and parameter affecting the relevant stator losses. However, the relation between M_a and each component is expected to be inverse: higher velocities in the nozzle region should lead to a reduction in viscous losses, while this same behavior will also increase the strength of the shocks appearing in the post-expansive region.

Hence, an trade-off is anticipated between this parameters and the stator performance. which would in turn implicate the existence of a minimum in the losses for a certain optimum value of M_a . This hypothetical relation is sketched in Figure 2.15 to provide a visualization of the concept.

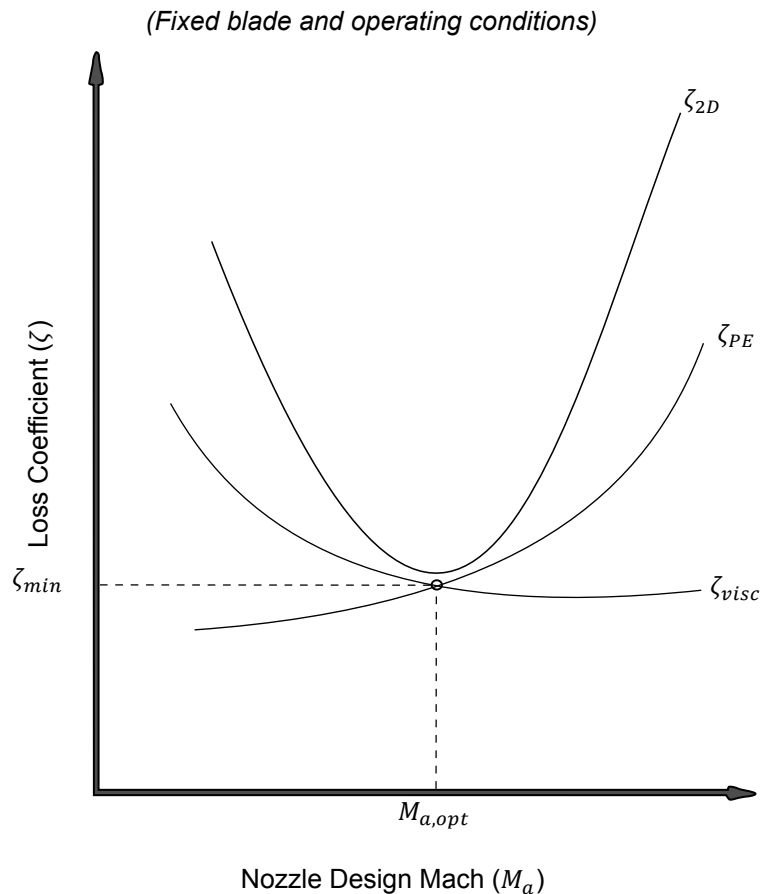


Figure 2.15: Sketch of the expected optimum existing for the profile losses of C-D stator blades based on the variation of the nozzle design Mach number

It should be noted, however, that another implicit assumption was made in the simplification of Equation 2.38: the total-to-outflow pressure ratio along the blades is fixed by choosing the total conditions (from the operating conditions of the turbine) and the back pressure (which is also the inlet pressure of the rotor). This will also be an important assumption that should be maintained if the optimum sketched in Figure 2.15 is to be found.

In order to prove this hypothesis it is necessary to investigate the performance of blades with varying degrees of post-expansion. Hereby is important that the assumed conditions can also be maintained while performing these experiments. The process of testing and collecting results in order to perform this task are detailed in the subsequent chapters of this report.

3

Methodology

The literature study and theoretical analysis presented in the previous chapter revealed certain parameters which are expected to exert a greater influence on the losses of radial C-D stators. In this chapter the method used to test the hypothesis formulated in section 2.3 will be addressed in detail. First the simulation based parametric study devised for this purpose will be explained, followed by an in-depth description of the tools necessary to carry out such an effort. Finally, the actual details of the design chain used to perform the simulations will be revealed.

3.1. Parametric Study

Following the analysis of section 2.3, a need to study the effect of the variations of a single parameter on the performance of stator blades arose. It was deemed appropriate to approach the problematic by carrying out a parametric study of these blades. In this project, this entails the monitoring of performance and behavior of the component of interest in a systematic fashion. A suitable range and number of steps for the variation has to be determined, and for each value of the parameter a different configuration can be built and tested.

CFD simulations have been chosen as the method of predicting the performance of the designs, as it allows to test several different configurations in a cost and time-effective manner; without the need of building actual devices and having the expensive measurement infrastructure required to collect results. The details of the workings of this mathematical tool will not be reviewed in this report. Numerous authors have written about this technique and the reader is encouraged to review some literature for a better understanding of how the results are produced.

The workflow of the process of generating a single geometry and simulating its operation can be visualized in Figure 3.1. Four major steps are required, which are aided by four separate computational tools.

In order to find trends, which are required to produce a result resembling the hypothetical plot presented Figure 2.15, several of these simulations are needed. This process has been semi-automated aided by developing a fifth tool, which will be explained more thoroughly in section 3.3.

Independent Variables

The hypothesis based on Equation 2.38 provides a strong argument for studying the effect of varying the nozzle design Mach M_a of C-D stator blades in search of the expected optimum value. Likewise, information present in subsection 2.2.3 makes it reasonable to consider analyzing the performance of the generated configurations based on their post-expansion ratio β_{PE} . It will become clear in the subsequent chapter that variations of this parameter can be achieved by either changing the value of M_a or the imposed pressure ratio on the stage β_{tot} .

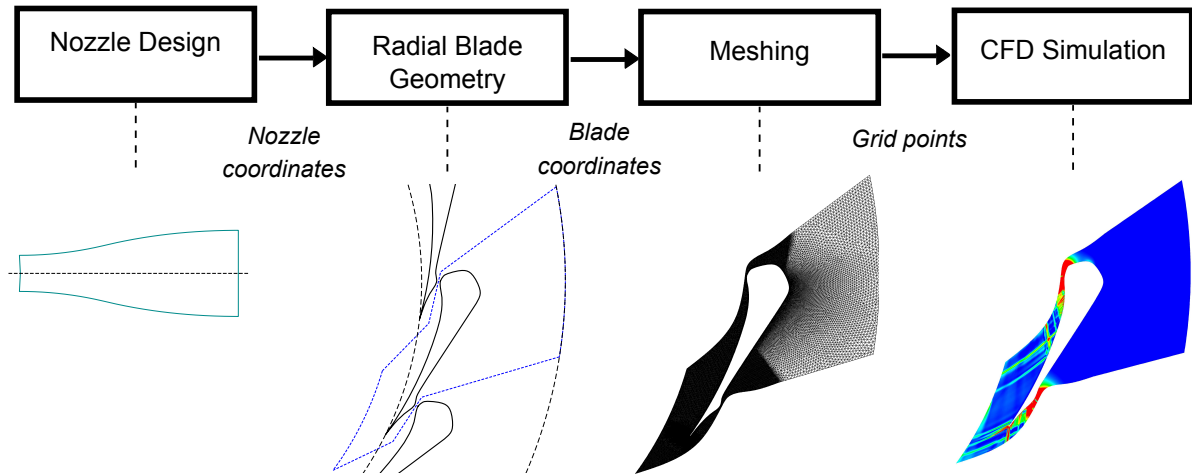


Figure 3.1: Flow diagram depicting the steps required to build and simulate a blade configuration

Dependent Variables

To quantify the performance of the different blade configurations, some variables calculated using the CFD results will be monitored. To study the behavior of the blades, the stage pressure ratio β_{tot} and outlet Mach number M_2 will be determined.

Based on the considerations presented in subsection 2.2.1, a reasonable choice for establishing trends in blade performance is the entropy production. The simpler loss coefficient defined in Equation 2.6 was chosen for the analysis. The advantage of using this version of the coefficient is that it has been demonstrated to be directly correlated with losses, while being more easy to be calculated at different stations along the blade.

It will be important, as will become clear in the next chapter, that the performance of the blades has to be placed in context with the resulting deviation of the flow. This parameter has been defined as the difference between the gauging angle ϕ and the outlet flow angle ϕ_2 . This can be expressed mathematically as

$$\Delta\phi = \phi - \phi_2, \quad (3.1)$$

from which follows that negative values represent a deviation towards the outflow boundary and a positive value towards the blade itself.

Other monitored values can be directly extracted from the CFD solver calculations at the inflow and outflow boundaries. However, for some calculations, values at the nozzle exit needed to be known. These have been determined by extracting a sample of points lying at this location, and performing an area average for pressure values and mass averages for other variables.

3.2. Blade Design & Simulation Tools

Producing a suitable blade contour for a specific application requires the use of two tools: a MoC-based nozzle design solver, which will be MoC tool and a radial C-D stator blade geometry generation procedure, referred to in short as the Radial Stator Tool (RST). To carry out a single 2D steady simulation for a given blade geometry, two tools are required: a meshing tool, and the CFD solver. These four important tools will be explained in separate subsections below.

3.2.1. Inverse Methodology Nozzle Design (MoC Tool)

As already treated in the previous chapter, a suitable starting point for the design of unconventional supersonic stator blades is the creation of an appropriate C-D nozzle. For this purpose the MoC-based solver mentioned in subsection 2.1.2 has been employed, which will be referred to as the MoC tool. Figure 3.2 displays a plot of the resulting characteristic lines used to generate the diverging nozzle section.

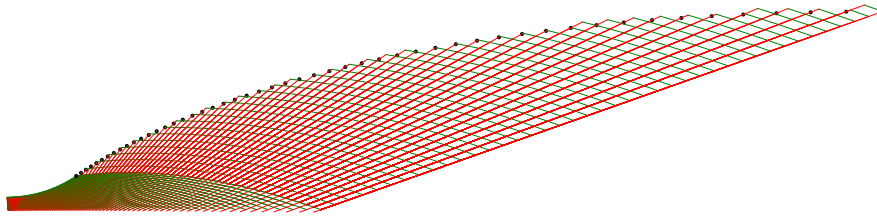


Figure 3.2: Plot of the characteristic lines used for the calculations to design the diverging region of a nozzle

The resulting lines can be compared with the basic sketch contained in Figure 2.5 used to explain the MoC in subsection 2.1.2. In this plot however, more lines can be observed than in the sketch, given that several points are needed to produce a smooth contour. This is controlled by the number of points on the throat. Likewise, the positive and negative characteristics have been differentiated from each other by using green lines for the former and red for the latter.

For practical reasons, the solver has been adapted, adding the CoolProp library to perform the thermodynamic state calculations of the fluid. This C++ library "implements pure fluid equations of state and transport properties" for several components [37], while having the advantage of being open-source.

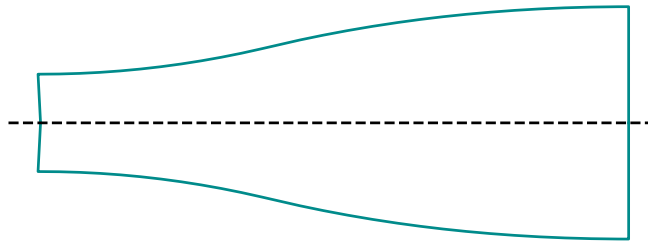


Figure 3.3: Plot of the nozzle coordinates resulting from the MoC-solver

Several input parameters are required for the solver to produce an appropriate C-D nozzle geometry. The most important parameters have been listed in Table 3.1. However, in the context of this project, for given set of stagnation conditions, throat length and working fluid, the only degree of freedom is the pressure ratio along the nozzle, or equivalently, the nozzle exit Mach number M_a . With the correct inputs, the solver will provide the raw data of the coordinates of the axi-symmetric nozzle solution; an example of such can be found in Figure 3.3

Table 3.1: Input parameters required to run MoC solver

Parameter	Description
Fluid name	Working fluid to be used in the nozzle
Gas equation*	Thermodynamic model used for calculations
P_o	Inlet total pressure [bar]
T_o	Inlet total temperature [K]
M_a	Nozzle exit Mach number [-]
y_t	Half throat length [m]
$R_{kern} \dagger$	Kernel region radius [m]
n_t	Number of points on the half throat line [-]

*Additional inputs related to thermodynamic conditions required when using certain gas equation.

†Refer to [38] for the exact details of this parameter

3.2.2. Radial Stator Tool

Using the coordinates of the diverging region of a C-D nozzle as input, a radial blade can be constructed. The procedure to generate the blade geometry is based on the steps proposed in [38]. In this work however, the procedure was adapted, restructured and extended to limit the degrees of freedom of the design. This was done to facilitate the implementation of this tool in an automatic simulation workflow, as will be explained in section 3.3. The implementation of a versatile and robust tool to generate radial stator blade geometries formed a large share of the work carried out during this project.

Design Procedure

In broad terms, seven steps are required to build the mean-line geometry of a stator blade. Step six is the main addition to the original procedure and necessary to reduce the minimum number of required input parameters. Moreover, a specific algorithm has been devised to execute the steps systematically in the necessary order if the required inputs are provided. The procedure has been outlined below, aided with the visualizations provided in Figure 3.4.

Step 1: the straight nozzle generated with the MoC tool is positioned on prescribed radius δR ;

Step 2: the nozzle is rotated to a pre-specified gauging angle ϕ ;

Step 3: conformal mapping of rotated nozzle is performed. This procedure is explained in more detail below;

Step 4: rotation of lower section of the nozzle by the pitch angle ($\theta = 2\pi/n$, where n is the number of blades) with respect to the origin;

Step 5: the nozzle is scaled, by a scaling factor F , to position the ending of the lower section on the prescribed radius, fixing the blade outlet limit;

Step 6: the converging section of the blade is built by connecting the upper and lower sections of the nozzle using a Non-uniform rational Bézier-spline (NURBS). This procedure is covered in more detail in at the end of this subsection;

Step 7: the fillet trailing edge is built based on the prescribed minimum distance t

An example of a geometry generated by the tool following the seven steps listed above can be found in Figure 3.5. Here the nomenclature used to describe the relevant geometrical parameters is also presented.

The chosen procedure requires the scaling of the nozzle to the prescribed radius R_{1b} , while maintaining the ratio O/A for the chosen gauging angle ϕ and minimum TE thickness t , which needs to be done in a curved frame of reference. This leads to a complex multi-parameter geometrical constraint problem relating F_g, M_a, ϕ and R_{1b} , which is solved by employing an optimization procedure, in the form of a minimization.

The cost function used to express the problem is based on the difference between the distance of the last point of both nozzle sections and the desired TE minimum distance. This function can be formulated mathematically as

$$\min_j J = d(n_a'(F), n_{1b}(F)) - t, \quad (3.2)$$

where the minimum allowable TE thickness t is often dictated by limitations in the manufacturing process.

Conformal Mapping

In general, the shape of the stator vanes depends on the flow condition upstream of the turbine, which is in turn determined by whether the designer employs a volute or a simple

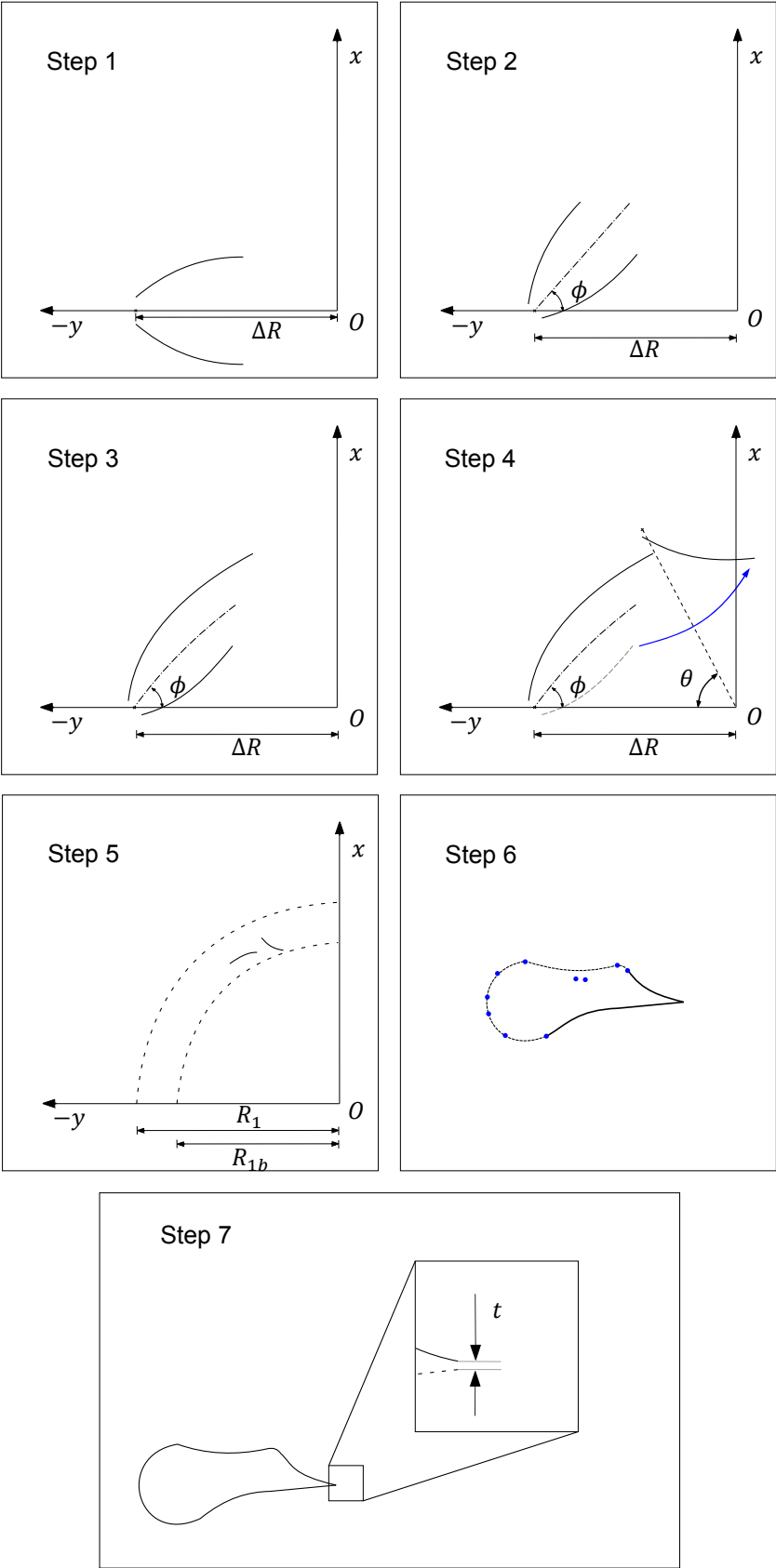


Figure 3.4: Schematic diagrams of the steps required to generate a radial blade geometry contour. Adapted from [38].

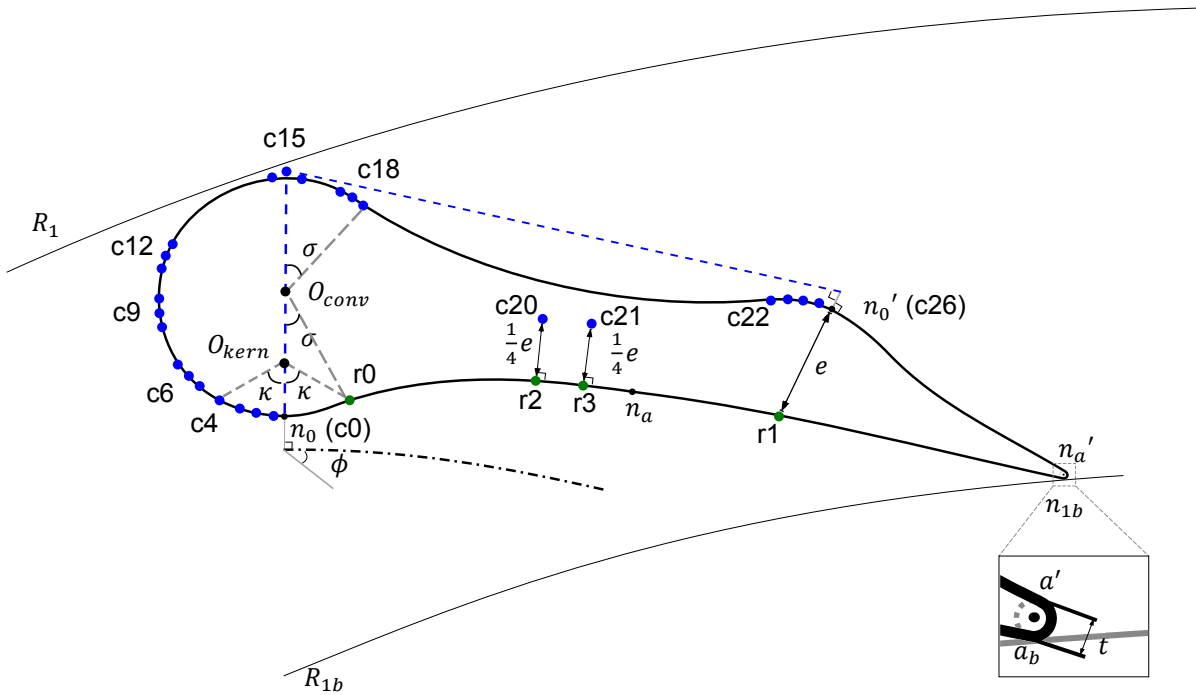


Figure 3.5: Schematic diagram of a stator vane geometry generated using the RST, including the chosen control points for the NURBS

collector. Volute inducers induce swirl in the flow, which may be sufficient to lead the fluid into the rotor blades at the correct flow angle. When a simple collector is employed, the swirl generation must be provided by other means, usually by curving the guide vanes [38].

A technique called conformal mapping has been employed to add this curve to the blades. An illustration of this process can be found in Figure 3.6. This transformation is deemed to be necessary for vanes used in the type of application relevant to this work [38].

Since the gas-dynamic behavior is dependent on the stream-wise cross-sectional area between the blades, it is important to maintain the area ratio prescribed by the MoC-tool. For this reason, conformal mapping is not applied directly to the nozzle geometry; instead, the nozzle center line is conformally mapped and the wall distance perpendicular to the center line is fixed by determining the wall distance along the main axis of the straight nozzle [38].

An important feature of this conformal mapping procedure is that it keeps the centerline of the nozzle at a constant angle with respect to the origin, as it has been illustrated in Figure 3.7. This is a desirable, given that the stator is designed to provide predictable flow conditions for the rotor blades.

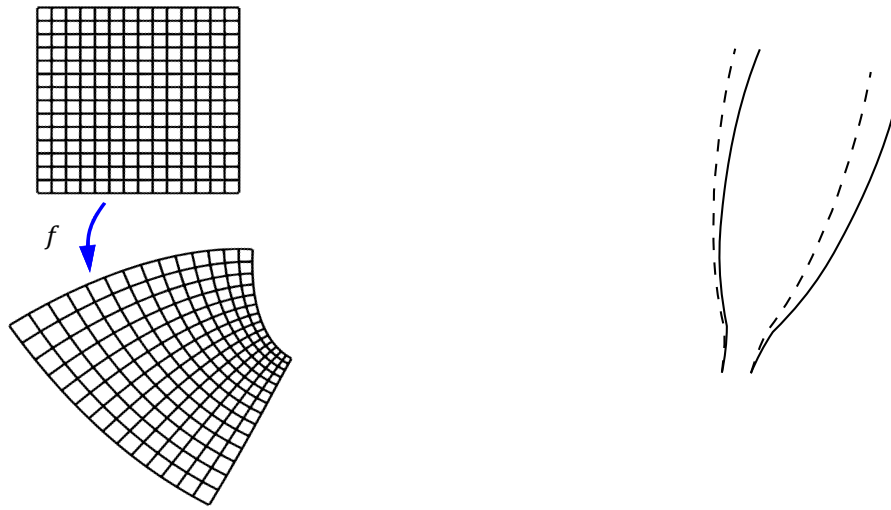
The final result of this process, which is equivalent to the resulting geometry after step 4 in Figure 3.4 has been illustrated in Figure 3.8.

Convergent Section Contour

As already stated in subsection 2.1.2, the converging section of the blade does not need to induce any specific fluid-dynamic behavior. Therefore, this area does not have a specific requirement in terms of geometric shape [24], except a gradual reduction in cross-sectional area; the main function of this region is to smoothly guide the incoming fluid into the blade throat.

As it can be observed in Figure 3.4, after step 5 the radially curved upper and lower sections of the nozzle are placed on the desired positions. This is the starting point of step 6, where a single curve, a NURBS, is generated to connect both nozzle sections, completely closing the blade contour.

“NURBS is a mathematical model commonly used in computer graphics for generating and representing curves and surfaces” [39]. A full account of the theory of NURBS curves can be found in several references; recommended reading is [40].



(a) Representation of Conformal Mapping

(b) Example of mapped nozzle

Figure 3.6: Visualization of the conformal mapping procedure [38]

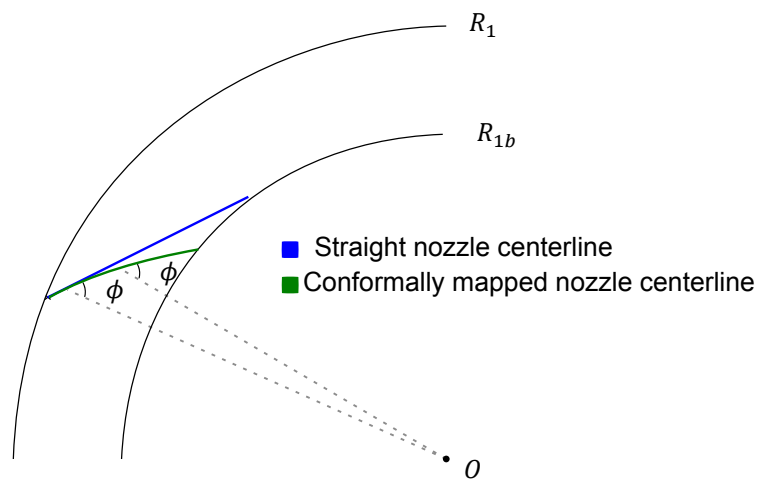


Figure 3.7: Visualization of the change of nozzle centerline after conformal mapping procedure within the radial limits of the stage. Adapted from [38]

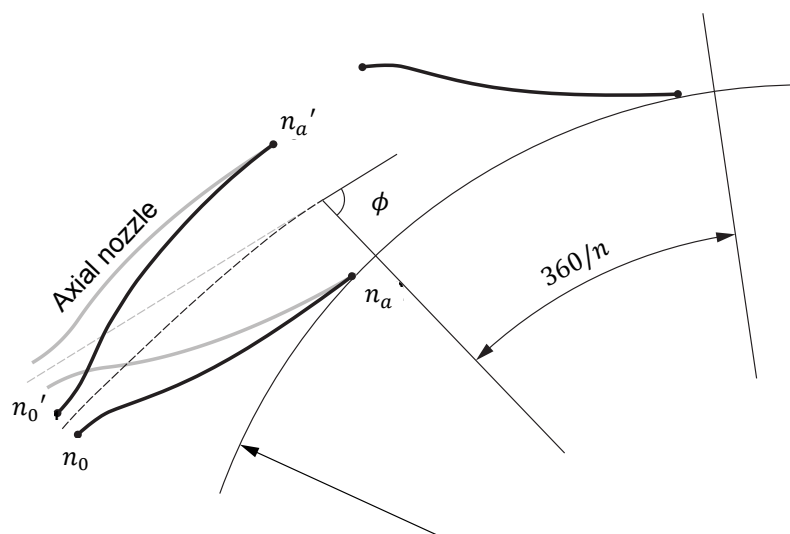


Figure 3.8: Visualization of the final product of the conformal mapping and nozzle positioning procedure. Adapted from [38]

Briefly described, a NURBS curve $N(g)$ of degree k can, in general, be written as

$$N(q) = \frac{\sum_{i=0}^n w_i B_{i,k}(q) P_i}{\sum_{i=0}^n w_i B_{i,k}(q)}, \quad (3.3)$$

where P_i is one of the $n + 1$ control points and $n \geq p$. w_i are the control points' weights and $B_{i,p}$ are basis functions. The variable q is varied within the interval $Q = [q_0, q_m]$, where q_0 and q_m are the initial and final values of a monotonically increasing sequence of size $m + 1$; the so-called knot sequence [27].

Moreover, the degree of the curve, the number of control points and the size of the knot sequence are associated mathematically by the relation

$$m = n + k + 1. \quad (3.4)$$

To completely define a curve, the knot sequence must be determined. In general, for a given set of control points, several valid sequences are possible. A *Python* based object-oriented NURBS curve and surface evaluation library [41] has been used to carry out this process, which includes a built-in function for auto-generating of the knot sequence.

The first step to setup the curve is to determine the necessary control points to achieve the desired shape. A plot of a blade geometry produced by the RST, including the position of the chosen control points with respect to the shape of the resulting curve can be found in Figure 3.5.

The contour of the leading-edge section of the blade is constructed using an arc, which will ensure smooth flow of the liquid towards the throat of the blade. The sizing and aspect ratio of the converging region is based on rules of thumb and experience of previous designs. A careful positioning of the control points is required to ensure that for any given specifications the blade can retain its desired features and properties.

The first and last control points (c_0 and c_{26}) are placed on the location of the initial point of the upper (n_0) and lower (n_0') nozzle sections respectively. A first reference point (r_0) is defined at the end of the expansion section of the upper nozzle contour. Flow continuity is provided by extending the line segment backward far enough for it to have the same length as the expansion section line. The kernel origin (already defined in the MoC procedure) is the center of the this newly formed arc. Four points (c_1 - c_4) are used to define the curve in this region. The continuity of the lower nozzle section is achieved by mirroring these points and rotating them by the pitch angle with respect to the origin (c_{22} - c_{25}).

A second reference point, also defined as a control point (C_{15}), is determined by finding the intersection of two virtual lines: the first perpendicular to the nozzle centerline and the second passing through the nozzle centerline of an adjacent blade (dashed blue lines in Figure 3.5). The middle of this line segment is chosen as the origin of the *convergent* circle.

Three additional points (c_6 , c_9 , c_{12}) are positioned by rotating n_0 by $\pi/4$, $\pi/2$ and $3\pi/4$, respectively, around the origin of the convergent circle. Two more points are added to each side of these points to ensure the 2nd order continuity (N^2) of the final curve as proposed by [27]. Finally, point c_{18} is found by rotating n_0 by the angle $2(\pi - \sigma)$ (where σ is the angle defined in the figure), again with respect to the origin of the arc.

To find the remaining two control points (c_{19} and c_{20}) another reference point (r_1) is defined at the perpendicular intersection between n_0' and the lower nozzle section, which also defines the length e . The final reference points (r_2 and r_3) are found at half the distance between c_0 and r_4 ; the control points are then located perpendicularly to them at a distance $\frac{1}{4}e$. This results in a total of 26 control points needed to build the curve.

Having chosen the required control points, the curve degree is chosen to be 25, a unit less than the number of selected control points. Weights must be chosen in order to ensure the curve will follow the control points close enough as required to achieve the desired shape. Their values have been determined mainly by means of trial and error. An overview of these points, including a short description and the value of the weights can be found in Table 3.2.

Geometrical Relations

It has already been established that there are some geometrical features which are expected to play an important role in the performance of these blades. The procedure that has been

Table 3.2: Summary of control points including short description and corresponding weight value

Point	Weight	Position
r1	-	End of upper nozzle expansion section
r2	-	Point on upper nozzle directly perpendicular to n_0'
r3	-	45% of line distance between n_0 and r2
r4	-	55% of line distance between n_0 and r2
c0	1	Start of upper nozzle (n_0)
c1	10	First point in backward upper nozzle continuity
c2	15	Second point in backward upper nozzle continuity
c3	20	Third point in backward upper nozzle continuity
c4	25	Rotated n_0 counter-clockwise by κ with respect to O_{kern}
c5	1	Adjacent to c6 to ensure N^2
c6	5	Rotated n_0 counter-clockwise by $\pi/4$ with respect to O_{kern}
c7	1	Adjacent to c6 for to ensure N^2
c8	1	Adjacent to c9 for to ensure N^2
c9	20	Rotated n_0 counter-clockwise by $\pi/2$ with respect to O_{kern}
c10	1	Adjacent to c9 to ensure N^2
c11	1	Adjacent to c11 to ensure N^2
c12	5	Rotated n_0 counter-clockwise by $3\pi/4$ with respect to O_{kern}
c13	1	Adjacent to c11 to ensure N^2
c14	1	Adjacent to c15 to ensure N^2
c15	20	Intersection of perpendicular to centerline and adjacent nozzle centerline
c16	1	Adjacent to c15 to ensure N^2
c17	1	Adjacent to c18 to ensure N^2
c18	1	Rotated n_0 counter-clockwise by $(\pi - 2\sigma)$ with respect to O_{kern}
c19	1	Adjacent to c18 to ensure N^2
c20	1	Located perpendicular to r3 at a distance of $1/4e$
c21	1	Located perpendicular to r4 at a distance of $1/4e$
c22	25	c4 mirrored on centerline and rotated by pitch with respected to origin
c23	5	c3 mirrored on centerline and rotated by pitch with respected to origin
c24	25	c2 mirrored on centerline and rotated by pitch with respected to origin
c25	5	c1 mirrored on centerline and rotated by pitch with respected to origin
c26	1	Start of lower nozzle section (n_0')

laid out in this section has shed light onto how these specifications are determined. In this context, it is also useful to find the link between design parameters and the resulting geometry. A simple sketch featuring the relevant geometrical aspects is contained in Figure 3.9 (cf. Figure 3.4).

Although the geometry becomes considerably more complex in a radial frame of reference due to the conformal mapping procedure, the analytic relations which determine the system should exist. However, the application of the optimization procedure provides a numerical solution to the problem. Nevertheless, this brings some additional uncertainty to the final design specifications.

In any case, the geometrical relations of certain parameters can be easily determined. This is the case of the pitch length L and the outflow area S , which are nothing more than arc lengths given by

$$L = \frac{2\pi R_{1b}}{\theta} = \frac{2\pi R_{1b}}{\frac{2\pi}{n}} = \frac{R_{1b}}{n}, \quad (3.5)$$

and

$$S = \frac{2\pi R_2}{\theta} = \frac{2\pi R_2}{\frac{2\pi}{n}} = \frac{R_2}{n}. \quad (3.6)$$

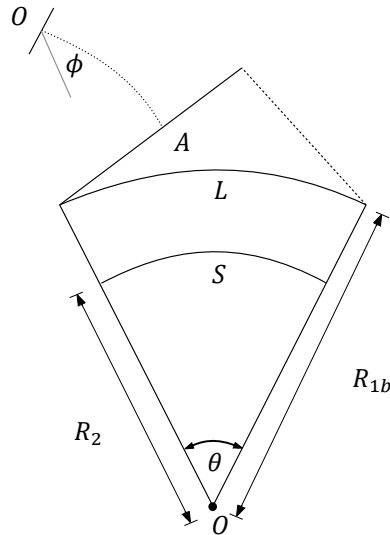


Figure 3.9: Schematic diagram of the relevant geometric features of a C-D radial stator blade

It should be noted that due to the radial nature of the turbine

$$S < L, \quad (3.7)$$

holds, which can have unforeseen effects on the stage behavior.

Complications arise for the other area lengths. As already known, the ratio O/A is fixed by the prescribed value of M_a in the MoC tool. However, the planar nozzle will be scaled to be positioned at the desired blade outlet radius R_{1b} , and this fixes the length A due for the given number of blades n and gauging angle ϕ . This can be expressed mathematically as the two area lengths being separate functions with the relevant parameters as arguments

$$O = \frac{O}{A}(M_a) \cdot A(n, \phi, R_{1b}) = f(M_a, n, \phi, R_{1b}) \quad (3.8)$$

given that O will be scaled to preserve O/A . These considerations will be useful when studying the influence of different parameters on the geometry behavior.

Computational Domain Delimitation

Due to the fact that the geometries will be tested with CFD simulations, it is required to delimit the computational domain around the blade contour where the fluid will flow. Given that a stator stage actually consists of equal blades operating under the same conditions, which are expected to behave in almost the exact same manner, simulating a single blade should suffice to predict the properties for the entire stage.

Therefore a single blade has to be enclosed between the inflow and outflow boundaries with two lateral equal lateral sides, being a rotation around the origin by the pitch angle from each other. When done correctly, a simulation domain could be duplicated and rotated by the pitch angle about the origin, and the domains would fit against each other. Repeating the process for the number of blades should then result in a simulations of the entire stage. More details about the mesh creation for this computational region will be given in the subsequent section.

3.2.3. Computational Domain Discretization (Meshing)

The computational domain for the experimental simulations is the region enclosing the blade shown in Figure 3.10. This region is discretized using an unstructured grid composed mainly by tri-lateral shapes, generated by a collection of tools called *UMG2*, which were made available for this project. The plot of generated mesh using the program can be compared to the chosen region in Figure 3.10.

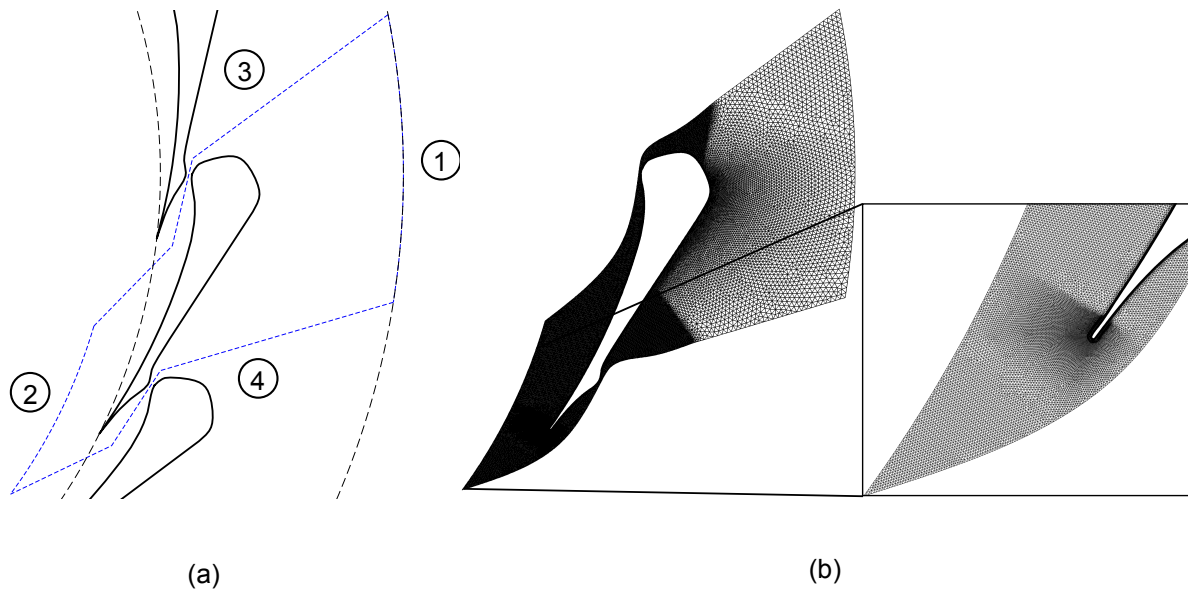


Figure 3.10: Plots of (a) computational region and (b) the resulting output of the meshing tool, including a close-up of the TE and outflow regions

Due to the expected subsonic flow that should be encountered between the inflow boundary and throat, this region has a relatively larger element size. This is done to preserve processing power, avoiding to perform extensive calculations in an area where the relevant flow structures can be captured by a coarser grid.

Tetrahedral cell elements are added around the blade walls, to resemble the structure of the boundary layer that is expected to form. These elements are clustered and enlarged along the blade boundary, using a growth function to increase the cell sizes in the direction perpendicular to the walls. This is required to increase the result accuracy when the simulations are setup to take the effects of viscosity into account; the y^+ value should be kept around unity. The boundary layer thickness is taken to be a percentage of the throat length O of each configuration.

As laid out in subsection 2.2.2 the trailing edge of the blade is a critical region in terms of flow behavior. For this reason, the cell elements enclosed within a radius a factor times the TE thickness t have been refined. This can be better visualized in the close-up of the region presented in Figure 3.10. Moreover, the cell dimensions are also reduced towards the outflow boundary plane due to the expected complex behavior of the fluid in the mixing plane.

UMG2 is a versatile and simple mesh-grid generator. However, in the context of sequential mesh generation, the program requires customized inputs for each different geometry. For this reason, an additional script has been written to manipulate the necessary configuration files and execute the programs. Two minimization functions have also been implemented to change the number of mesh elements and the TE refinement; the former allows to maintain constant grid conditions for the different configurations, while the latter will improve the aspect ratios of the resulting meshes.

3.2.4. Numerical Solver

Flow solutions are obtained by solving the Reynolds-averaged Navier-Stokes equations within the computational domain. The chosen solver to perform this task was the open-source *SU2 CFD* [42] software suite. Capabilities of the software to deal with the numerical simulation of viscous flows over unstructured grids have been extended to handle NICFD, the effects of which are typically encountered in planar nozzles similar to the ones studied in this project. Results obtained from test cases have demonstrated that *SU2* is suited for the analysis of flow devices operating under these extreme conditions [43].

For the simulations, the thermo-physical properties of the working fluid are computed

with the Peng-Robinson equations of state [44]. Furthermore, a constant viscosity and conductivity model have been used for these fluid characteristics. A Roe scheme has been chosen for the convective numerical method. The spatial integration occurs using a 2nd order scheme, while the time discretization is integrated using an Euler implicit solver.

Viscous flow will inevitably lead to turbulence for the operating conditions of the blades. The two-equation eddy-viscosity Shear Stress Transport [45] model has been used to close the turbulence equations. This model is solved spatially using 1st order integration and the time scheme is again Euler implicit. All of these solver capabilities have been previously implemented in *SU2* by different contributors.

Boundary conditions are also part of the input parameters that must be specified for the CFD solver to function correctly. A stator stage usually consists of a row of several blades acting together, as displayed in Figure 3.11. These blades should however be operating under the same conditions, which permits the possibility of simulating a single blade to represent the entire stage. As such, the computational domain shown in Figure 3.10 can be used, which consists of four major boundaries: the inflow (1), outflow (2), and the two lateral surfaces ((3) and (4)). Boundaries (3) and (4) are the same line segment duplicated at an angular distance equal to the blade pitch; they connect boundaries (1) and (2) together. For this reason boundaries (3) and (4) are of the periodic type, causing all fluxes to cancel each other out.

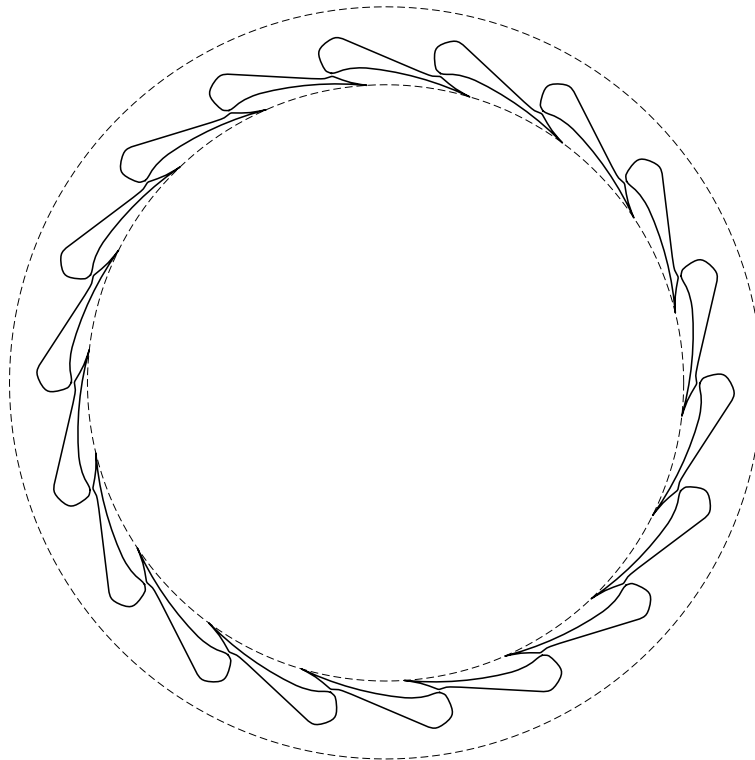


Figure 3.11: Plot of an eighteen blade stator stage including radial limits

Non-reflecting boundary condition (NRBC), previously implemented in *SU2*, have used imposed on the inflow and outflow. NRBC prevent the formation of non-physical boundary reflections [31]. This implementation is based on solving the incoming characteristics using 2D non-reflecting theory proposed in [46].

SU2 requires several other inputs to perform the calculations correctly. These must be provided in a configuration file with a specific format. The file used for all the simulations in this work, which can also provide additional information about the details used for the calculations can be found in Appendix A.

3.2.5. Additional Post-Processing

Although in a technical sense not part of the simulation workflow shown in Figure 3.1, additional post-processing tools were used to provide the desired trends. These have to be differentiated from the internal post-processing already included in *SU2*. These tools consist mainly of the point extraction and the final property calculation and data collection scripts made for the purpose of this work.

The point extraction script allows to obtain points in the geometrical throat and nozzle exit boundary lines. This is done commanding the a commercial visualization program *TecPlot360* to generate a certain number of points between a set of given coordinates. The process has been automated to some extent using a *Python* script to produce macro files which are sent as batch instructions to *TecPlot360*. Because the boundaries are split at each side of the blades, the extraction occurs in two separate steps.

A second script is able to do additional calculations of properties based on the totality of data produced in each of the design steps, by the different tools. One important utility added to this script is the area average and mass average line integration procedures used to determine properties such as pressure and entropy production at the nozzle exit. Results used to verify the accuracy of these integration procedures can be found in Appendix C.

Once the relevant calculations are done, the script proceeds to print the important results into a *result summary* data file. Repeating the process for every configuration in a given set provides enough that to plot the relevant trends.

3.3. Semi-Automated Design Chain

To perform a single simulation, the four main tools presented in the previous sections have to be used sequentially, with each tool in the processes receiving input data from the previous step. To test the hypothesis presented in section 2.3, a parametric study is required to determine the effect of varying a single parameter on the stator performance. Therefore, in order to find the necessary trends, several simulations of configurations with variations of a certain parameter are required. Such a string of simulations will be henceforth referred to as a simulation *run*.

This process has been automated as far as the scope of this project permitted it. A script bundle written for the rotor optimization of the same type of turbine the stator belongs to, was provided for the project and adapted to control the setup of the simulations. This script bundle is based on the *Python* programming language, which has the advantage of being open-source. A flowchart of the framework has been laid out in detail in Figure 3.12.

Based on the structure of the original code, the workflow hierarchy has been defined as follows: an *executable* is the elementary unit, representing each of the basic steps that can be carried out. A set of executables performed in a sequence is called a *job*. A *run* is then the name given to a batch of jobs in which a specific parameter is varied discretely.

In a run, any input parameter Z can be chosen and fed into the design chain, together with the variation range and the number of steps $i + 1$. The main tool also has access to templates of all the necessary configuration files. Using this information, the script will modify the necessary parameters in these templates and create new configuration files for a given value z of parameter Z . In Figure 3.12, the relevant parameters associated with each of the configuration files have been added for reference purposes.

Once all the necessary files are set in place, in a separate job directory, the tools can be ran sequentially, with each tool generating output for the next step and also overall specification data used for further analysis. Repeating the process $i + 1$ times results in the specified run. These steps can be carried out in a local computer, but the original script could handle sending jobs to external servers. This functionality was taken advantage of and in this case most simulations were performed in the Reynolds cluster of the 3mE faculty at the Delft University of Technology.

Finally, when a run has successfully been completed, a separate post-processing script collects all the relevant data for each value of Z , which can then be used to produce the necessary trends portraying the effects of the variable of the blade performance and behavior.

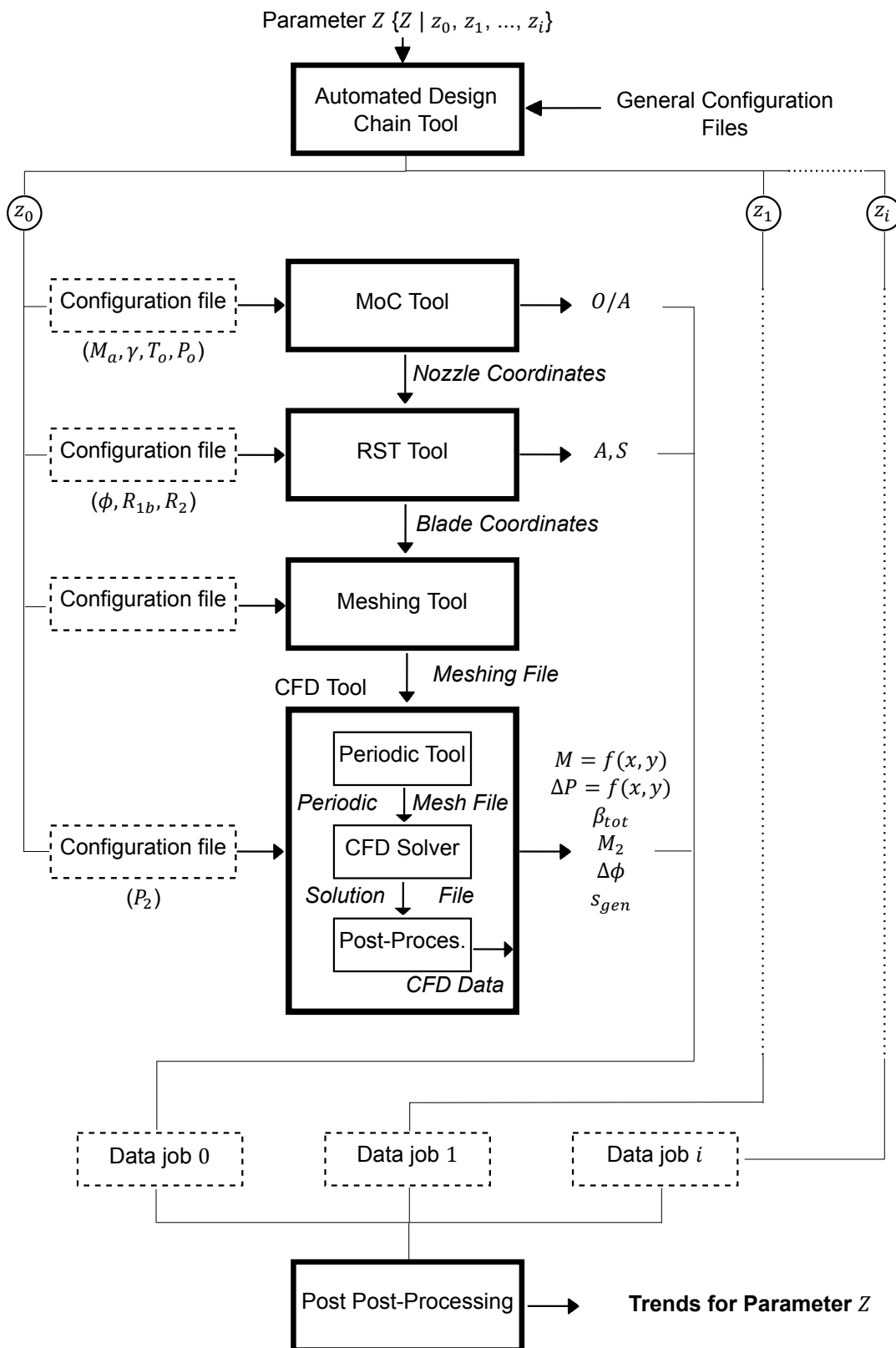
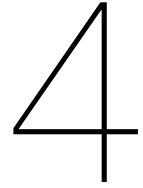


Figure 3.12: Flow diagram illustrating the structure and workflow of the semi-automated design and simulation chain



Method Application

Given its generic structure, the parametric study of C-D radial stator vanes presented in the previous chapter can be applied to a wide range of cases. To evaluate the hypothesis of section 2.3, it has been deemed useful to carry out the study starting from an existing design. In this chapter, the previously proposed method has been applied to a candidate test case. Due to the exploratory nature of the project, results and discussion have been merged, presenting the findings in separate sections based on the underlying *theme*.

4.1. Case Study

It is possible to employ the generalized semi-automated design chain presented in section 3.3 to different types of stator vanes; it can even be extended to axial and sub- and transonic architectures if the blade geometry generator and the corresponding meshing is adapted accordingly. To simplify the task and limit the scope of the project, a commercial device has been chosen as the starting point of the study.

4.1.1. Test Case

An existing design belonging to a manufacturer which has been involved in the development of compact ORC power systems has been made available for this project. Using this test case provides continuity to the research work, as this is the same device used to test the effectiveness of the MoC tool in [10].

An overview of the relevant parameters and conditions of the test case have been summarized in Table 3.2. This set of conditions will be referenced as the *base case* and the corresponding values as Base value (BV). The subscript BV will be used to reference the original value of variables which cannot be made explicit to protect the intellectual property of the manufacturer.

4.1.2. Simulation Details

Though the fundamental structure of the parametric study has already been presented in section 3.1, there are some case specific details that need to be determined to perform a case study.

Following the assumptions used for the analysis in chapter 2, the experimental simulations will remain planar and therefore all the variables will present changes in the horizontal direction; the meridional (z-vector) value is assumed to remain constant. In this context, based on the previous findings, the main independent variable will be the nozzle design Mach for the experiments. The relevant test range for this variable is within the interval $\{M_a \mid 1.4 \leq M_a \leq 3.0\}$; the lower limit is based on the design guide line mentioned in subsection 2.1.2, while the upper limit is based on the magnitude of this variable that the tool which generates the stator geometry can handle.

Relevant meshing parameters have been chosen using a simple mesh convergence study, the details of which can be found in Appendix B for reference purposes. In this case an

Table 4.1: Overview of important design parameters of the test case and their original base value

Parameter	Value
Nominal Power	200 kW _e
Fluid	Toluene
β_{tot}	40
P_o	$P_{o,BV}$ * bar
T_o	$T_{o,BV}$ * K
M_a	$M_{a,BV}$ *
ϕ	ϕ_{BV} °*
R_1	$R_{1,BV}$ * m
R_{1b}	$R_{1b,BV}$ * m
R_2	$R_{2,BV}$ * †m

*Confidential data

†Not specified in the original case

average overall number of elements $\sim 1 \cdot 10^5$ has been taken, with a boundary layer thickness (H_{BL}) of $0.15 \cdot y_t$ and a TE refinement radius (R_{TE}) of $5 \cdot t$. Similarly, the total number of iterations per simulation used was $1 \cdot 10^4$ to ensure convergence for even the most troublesome configurations. All solutions were assumed to convergence if *SU2* did not diverge during the iterations.

Values used for the constant parameter models (specific heat ratio, viscosity and conductivity) in the CFD simulations have been taken as the average of the inlet and isentropic outlet conditions. This takes the form

$$V = \frac{V_1 + V_{2s}}{2}, \quad (4.1)$$

where V represents any of the abovementioned constant parameters.

The importance of the relationship between design parameters and the relevant geometrical features has already been remarked before. However, these relations are complex, especially when considered in a radial frame of reference and with the added uncertainty of the optimization procedure implemented in the RST tool (cf. subsection 3.2.2).

For this reason, a geometry sensitivity analysis has been carried out. It consisted of varying the main design parameters found to be affecting the contour of the blades in subsection 3.2.2, namely the nozzle design Mach, the flow angle and the blade outlet radius. These parameters have been varied within the following intervals: the main $\{M_a \mid 1.4 \leq M_a \leq 3.0\}$, along with $\{\phi \mid 45^\circ \leq \phi \leq 85^\circ\}$ and $\{R_{1b} \mid 0.76 \leq \frac{R_{1b}}{R_{1b,BV}} \leq 1.17\}$ respectively.

As an additional measure, variations in solidity, throat length size and the error of the blade radial position and TE thickness have been monitored for these runs. The latter three have been non-dimensionalized by taking the ratio $\frac{\sigma}{\sigma_t}$ of the actual length to the original MoC half throat value, and defining the error

$$\epsilon = \frac{\Delta V}{V}, \quad (4.2)$$

where V again here can represent any variable to be considered in the analysis.

Supplementary to the main experimental simulations, runs for the same range of M_a but for different total-to-outflow pressure ratios have also been performed. Likewise, the exercise was repeated for the base case, but for three different radial positions of the stator outlet (R_2), to determine if the area length of this outflow boundary has any influence on the stage behavior.

Likewise, runs for a blade configuration with fixed nozzle design Mach have been carried out by varying the back pressure, P_2 . This was done to determine the relevance of the PE ratio

as a design parameter for the blades, which can be manipulated by changing the pressure ratio that is imposed along the blade row. The range of pressure ratios are dependent of the blade configuration, as will become clear in the subsequent sections.

Finally due to the expected variations in throat size resulting from varying M_a , it was decided to monitor the mass flow in the system for each configuration, as a precautionary study to analyze the possible effect on the viscous losses based on the variation of the throat Reynolds number. This was achieved by artificially varying the viscosity of the fluid in the CFD solver in a logarithmic range of $\{\mu \mid 10^{-12} \leq \mu \leq 10^{-1} \text{ Pa s}\}$.

An overview of all the performed runs for this study, including the step size of the variation of each parameter, can be found in Table 4.2. Some jobs only included the generation of a blade geometry, needed for the sensitivity analysis. Runs consisting only of this kind of job are denoted by the type "Geometry". Jobs which also performed meshing and simulation of the generated geometries are of the "Simulation" type.

Table 4.2: Summary of all the runs and the respective jobs performed to collect the necessary data for the analysis

Variable	Range	Step Size	Type	Modifications	Jobs
M_a [-]	1.4 – 3.0	0.05	Simulation	(Main run)	33
M_a [-]	1.4 – 3.0	0.05	Geometry	$\phi = 70^\circ$	33
M_a [-]	1.4 – 3.0	0.05	Geometry	$\phi = 75^\circ$	33
ϕ [°]	45 – 85	1	Geometry	$M_a = 1.4$	41
ϕ [°]	45 – 85	1	Geometry	$M_a = 2.2$	41
ϕ [°]	45 – 85	1	Geometry	$M_a = 3.0$	41
$R_{1b}/R_{1b,BV}$ [-]	0.76 – 1.18	0.04	Geometry	$M_a = 1.4$	11
$R_{1b}/R_{1b,BV}$ [-]	0.76 – 1.18	0.04	Geometry	$M_a = 2.2$	11
$R_{1b}/R_{1b,BV}$ [-]	0.76 – 1.18	0.04	Geometry	$M_a = 3.0$	11
Iterations [-]	20000	1	Simulation	$M_a = 3.0$	1
H_{BL}/O [-]	0 – 0.3	0.01	Simulation	$M_a = 3.0$	31
R_{TE}/t [-]	0 – 20	1	Simulation	$M_a = 3.0$	21
Mesh Elements [-]	$4 \cdot 10^4 - 20 \cdot 10^4$	10^4	Simulation	$M_a = 3.0$	17
μ [Pa s]	$10^{-12} - 10^{-1}$ (log)	$10^{\frac{1}{2}}$	Simulation	$M_a = 3.0$	23
M_a [-]	1.4 – 3.0	0.05	Simulation	Riemann BC	33
M_a [-]	1.4 – 3.0	0.05	Simulation	$\beta_{BC} = 20$	33
M_a [-]	1.4 – 3.0	0.05	Simulation	$\beta_{BC} = 80$	33
M_a [-]	1.4 – 3.0	0.05	Simulation	$\beta_{BC} = 160$	33
M_a [-]	1.4 – 3.0	0.05	Simulation	$R_2/R_{2,BV} = 1.05$	33
M_a [-]	1.4 – 3.0	0.05	Simulation	$R_2/R_{2,BV} = 0.95$	33
β_{BC} [-]	2.5 – 20.0	0.5	Simulation	$M_a = 1.8$	36
β_{BC} [-]	5 – 80	1	Simulation	$M_a = 2.2$	76
β_{BC} [-]	10 – 60	5	Simulation	$M_a = 2.4$	26
β_{BC} [-]	10 – 160	10	Simulation	$M_a = 2.8$	31
Total Jobs					715

It should be noted that it was only possible to run such a large amount of simulations due to the added capabilities of the RST and the functionality semi-automated design chain. Manually carrying out all of the separate jobs would have probably restricted the amount of data that would have been possible to produce in the time frame of the project.

4.2. Results & Discussion

As previously stated in the chapter introduction, the exploratory essence of this work led to the investigation of different parameters resulting in some interesting insights, which differ sometimes substantially in theme. Some of the findings are also better understood once some preliminary results are presented and described. For this reason, the results have been presented together with the corresponding discussion in separate *thematic* sections;

these have been ordered to present the reader with what was deemed the most coherent "story" in this research.

4.2.1. Geometry Sensitivity Analysis

A sensitivity analysis has been carried out to study the effect of M_a and ϕ on the the throat length O , blade solidity C/L (used to track changes in blade dimensions), the TE thickness t and R_{1b} in this complex system. As already mentioned in subsection 3.2.2, monitored parameters have been non-dimensionalized to ensure the generalization of the results. The first set of data, related to the variation of M_a can be found in Figure 4.1.

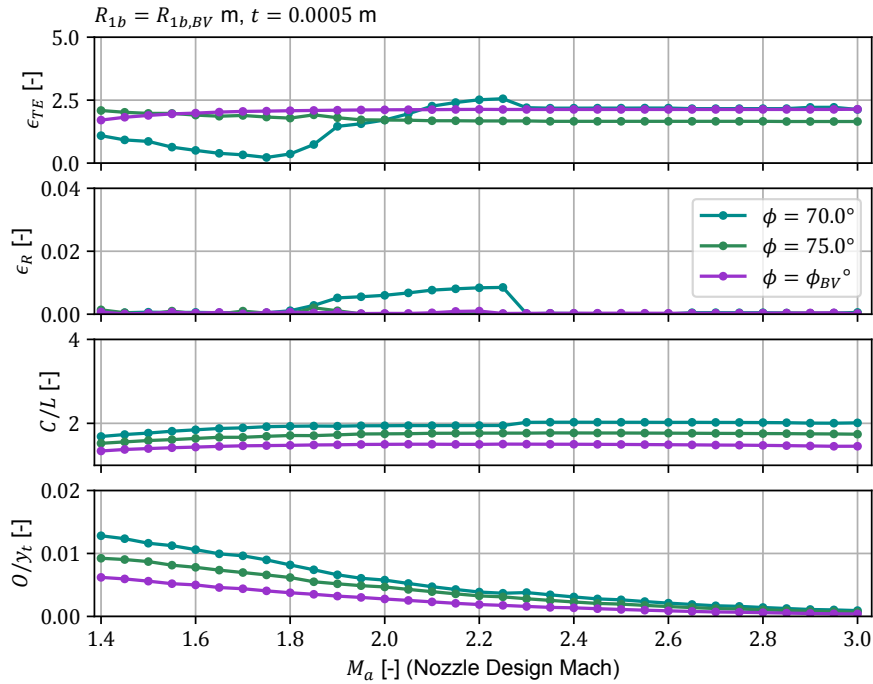


Figure 4.1: Plot of the TE thickness and blade outlet radius errors, solidity and throat scaling (from top to bottom) for varying values of the nozzle design Mach

The variation of M_a was done for three different values of ϕ . It can be observed from the behavior of the lowest ϕ value trend, that lower gauging angles will start causing unexpected geometrical behavior. Similarly, it can be seen that the optimization procedure converges convincingly well towards the specified R_{1b} , although this seems to occur at the expense of the accuracy of t .

The solidity trends show that for this variable the sizes of the blades do not change substantially, however, because A is fixed for chosen R_{1b} and ϕ , the size O decreases substantially to maintain the nozzle area ratio. This already raises concerns regarding how controlled an experiment will remain when changing M_a if such a vital parameter changes simultaneously with it.

A final remark regarding the results for this parameter is that through out the variations the area length A has remained constant. This would in practice mean for a complete stator stage that the ratio A/S would also be maintained when varying M_a .

The exercise was repeated for a range of flow angles for three blade geometries with different M_a , the results of which have been plotted in Figure 4.2.

These trends shows that the stability of the optimization procedure is reduced when varying ϕ . In the first place, for lower values of M_a , the procedure cannot converge for low values of ϕ . The scaling of O is once again present, becoming less steep with each increasing value of M_a ; this could be attributed to the scaling which is already induced on the blades by the change in this variable (cf. the previous figure).

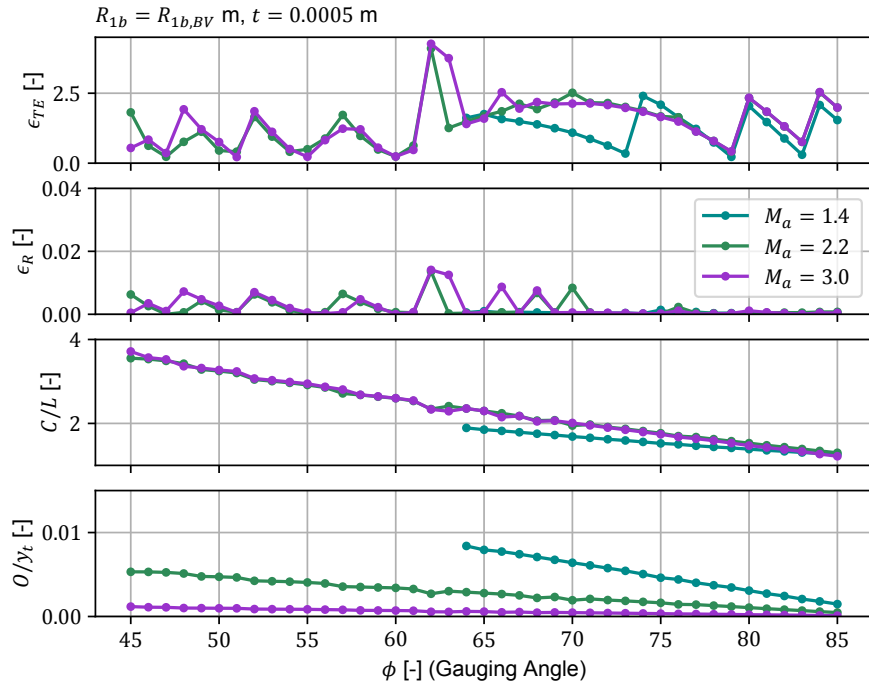


Figure 4.2: Plot of the TE thickness and blade outlet radius errors, solidity and throat scaling (from top to bottom) for varying values of the flow angle

There is however an inverse relationship between the flow angle and the throat length. More importantly is to note that changes to ϕ will incur in blade size and aspect ratio variations of great magnitude, as it can be asserted from the solidity trends of this figure. These modifications might lead to changes in the viscous losses, because of the change in total blade wall surface area.

Lastly, following the same procedure, the effect of varying R_{1b} on the final geometry can be found in Figure 4.3.

It can be noted that the variations in this case seem to be more stable than the previous plots in terms of errors. Although size changes were expected to take place when varying this parameter, the throat scaling trends show small changes in value. Moreover, the solidity of the blades was expected to change, as L is fixed by the pitch angle and the radial location of the blade TE (R_{1b}). Remarkably, the resulting solidity trends could be considered to be constant, meaning that the process scales the value of the blade chord at the same rate.

One trend present for all three variables is the large TE thickness error values. This could signify that manufacturing limitations might not be the only constraint existing for this specification. Finally, some qualitative aspects of these trends can be better visualized in Figure 4.4, where some blade examples for the changes in variables have been gathered.

A careful study of the figure can provide some further insights not attainable from the trends. First of all, Figure 4.4(a) contains plots of three blades which show the severity of the throat scaling for the different blades; the left blade, which has a low M_a has therefore a relatively large throat width, leading to some kind of indentation in the blade, while the blade having a high M_a value shows a steep change in profile close to the throat region. Both effects are not desirable in terms of geometry smoothness. Nonetheless, the rest of the geometry seems to remain relatively constant, as predicted by the trends of Figure 4.1.

In turn, Figure 4.4(b) shows the clear change in throat width and aspect ratio of the blades which already appeared in Figure 4.2. The large error in TE can be appreciated in the left plot. It is expected that the optimization procedure compensates for errors in the minimization function by fluctuations in the value of t . What becomes clear from this image is that variations in this parameter lead to the largest overall changes in geometry.

Finally, the three plots in Figure 4.4(c) illustrate the change in size with constant aspect

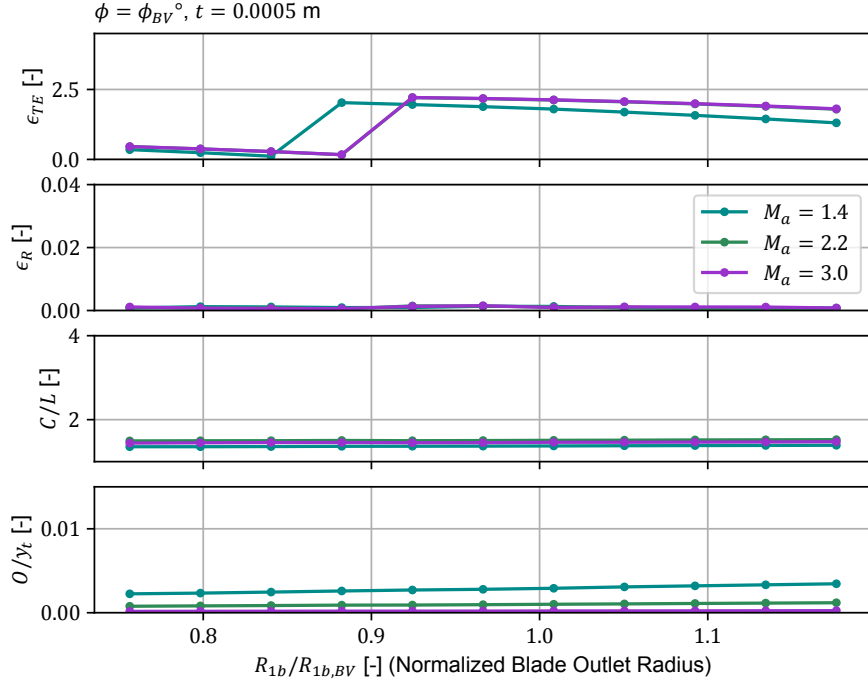


Figure 4.3: Plot of the TE thickness and blade outlet radius errors, solidity and throat scaling (from top to bottom) for varying values of the blade outlet radius

ratio which is enabled by the variation of the blade R_{1b} value.

In general terms, it can be expected that changes to M_a will lead to simultaneous changes in throat width. This is also true for changes of gauging angle, although changes to this parameter also lead to changes in the blade aspect ratio. Finally, changes to the radial position of the blade outlet will produce a blade scaling with almost constant aspect ratio and throat width. Varying all three parameters simultaneously forms a design space with the possibility of generating a large range of geometries.

It becomes clear however, after reviewing the results of this preliminary study, that the original hypothesis, which was based on the assumption that the degree of expansion within the nozzle could be varied freely for a constant nozzle geometry, will become difficult to test.

Due to the critical role of the throat specifications on the system behavior, it will be problematic to isolate the effects of changing M_a with the simultaneous change in O . The only plausible means of countering the scaling induced by M_a would be to vary the gauging angle simultaneously. This would however lead to changes in blade dimensions and come at the cost of severe modifications to geometrical aspect ratios.

4.2.2. Stage Expansion Behavior

Although not the main subject of study, the calculations resulting from varying the main independent variable M_a showed some unexpectedly large variations between the ratio of the imposed pressures at the boundaries and the predicted value from the CFD simulations. This divergence is also a hurdle to prove the original hypothesis, given that it was initially expected the degree of expansion could be varied independently from the fixed pressure ratio between the system boundaries. Hence, it became necessary to study why this assumption could not hold and how it would affect the experiments.

Therefore this difference will henceforth be referred to as $\Delta\beta$ and defined as

$$\Delta\beta = \beta_{tot} - \beta_{BC}. \quad (4.3)$$

This effect can be visualized by plotting the calculated pressure ratio for each blade configuration generated in the main M_a run. It follows from Equation 2.1, the Mach-area relation,

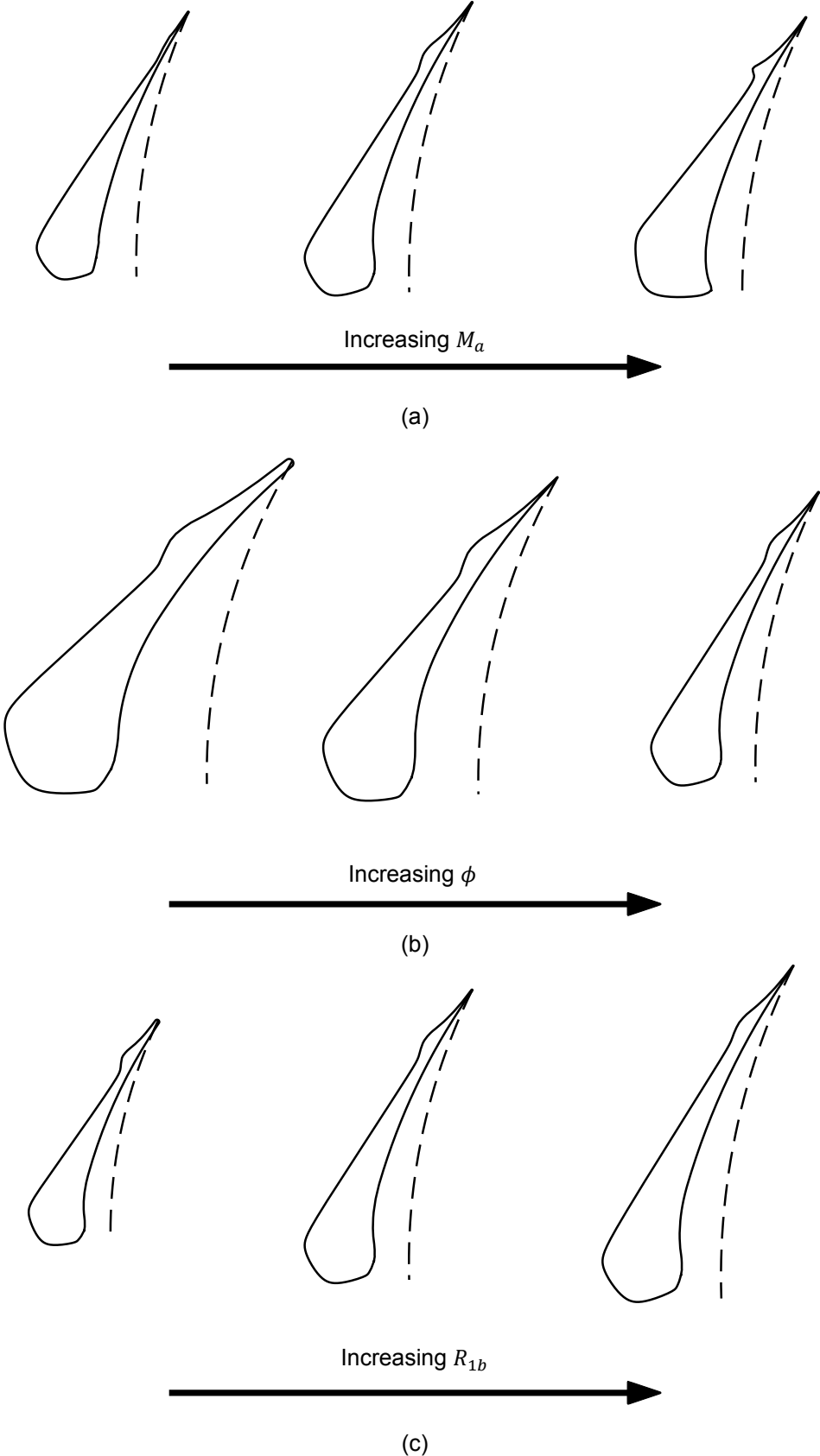


Figure 4.4: Plots of different blade configurations showing the sensitivity of the geometry with respect to (a) nozzle design Mach (b) gauging angle

that pressure ratio and exit Mach number in internal flows are physically related; for this reason the results of the calculated M_2 values have been added together with the previous plot in Figure 4.5.

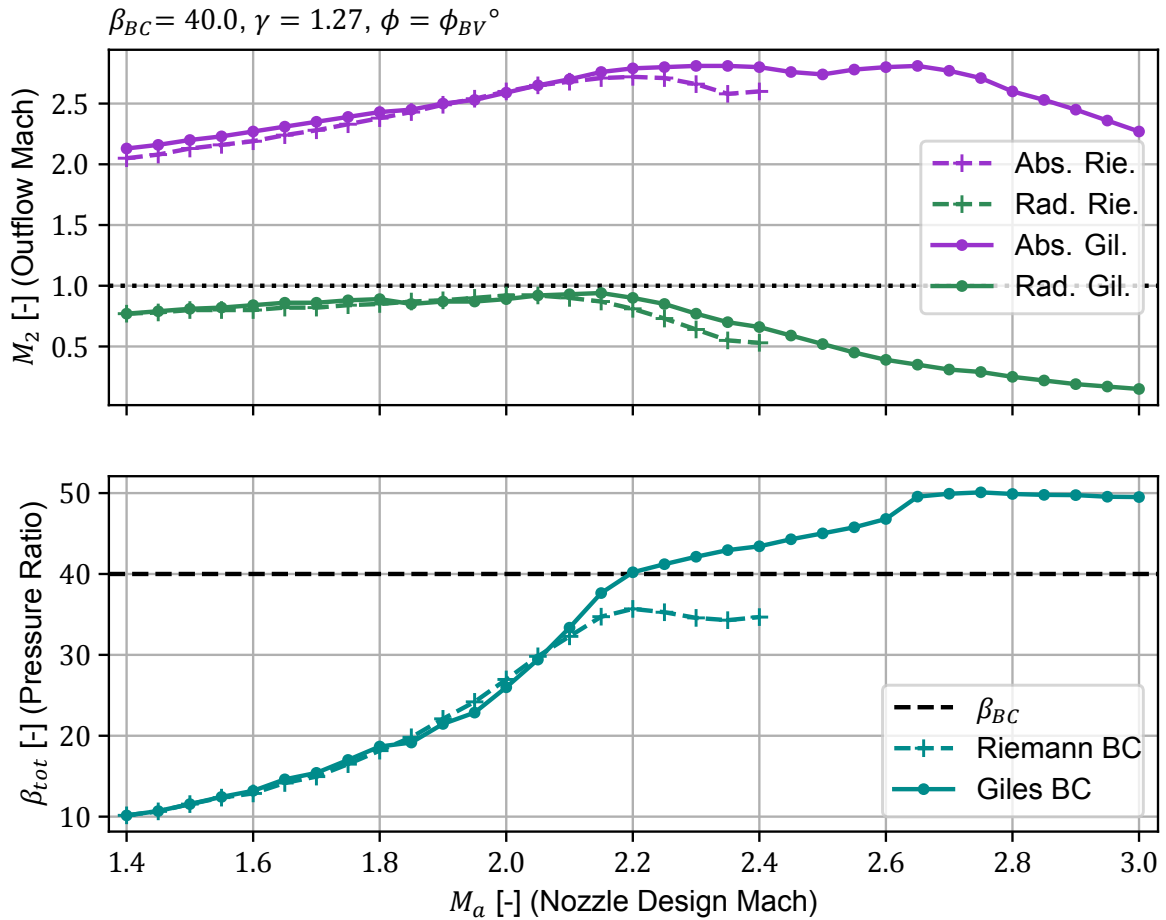


Figure 4.5: Simulation results of outflow Mach and total-to-outflow pressure ratio for blade configurations with varying value of M_a

This plot also contains results ran with Riemann BC for the inflow and outflow boundaries, a more common but reflective type of BC, which can be used as a basic validation for the found trends.

The first observation that can be made is that the simulations using a Riemann BC for this specific CFD configuration using second order integration only converge for $M_a \leq 2.4$. Nevertheless, simulations that do converge show reasonable agreement for both BCs until $M_a \approx 2.1$. This agreement provides some evidence signaling that the pressure ratio deviation can be expected to be physical.

To examine more closely the effects of changing the BCs, a qualitative analysis of the flow field based on the absolute pressure gradient (∇P) contour of two equal blade configurations having each a different BC; these plots are Figure 4.6. It can be clear by observing the flow structure that the Riemann BC leads to the appearance of additional discontinuities, which could be attributed to non-physical reflections at the outflow boundary. This result provides a strong argument for the implementation and usage of NRBCs for this type of simulations.

Returning to Figure 4.5 and now focusing on the Giles BC based results, it can be seen that for the chosen stage pressure ratio, there is apparently only one result where $\beta_{tot} = \beta_{BC}$, in this case $M_{a,\beta} = 2.2$. For values $M_a < M_{a,\beta}$ the stator stage is under-expanded, meaning that the calculated pressure value at the outflow boundary is higher than the imposed back pressure. Similarly for $M_a > M_{a,\beta}$ the flow is over-expanded, leading to a lower pressure

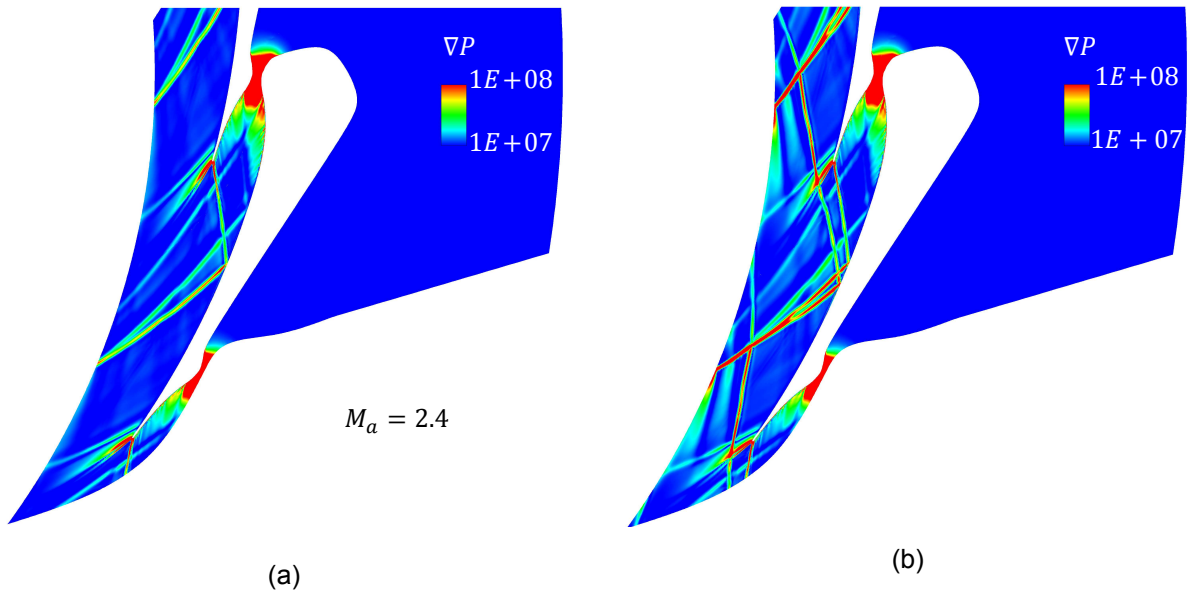


Figure 4.6: Pressure gradient contour of two equal configurations simulated using (a) Giles (NRBC) and (b) Riemann (Reflective) boundary conditions

level at the outflow than the imposed value.

Outflow Mach trends, showing both the value of the absolute and radial components, give some additional information regarding the previous observation. The radial component $M_{2,r}$ is near unity for all under-expanded configurations, reaching its highest value a step before $M_a = M_{a,\beta}$. After this point it decreases sharply for over-expanded geometries. It is unknown if the solver has a ceiling for $M_{2,r}$, restricting the flow from reaching supersonic radial velocities and which could therefore limiting the expansion process in the blades for $M_a < M_{a,\beta}$.

In any case, the decrease of $M_{2,r}$ seems to be related to the decreasing value of M_2 for over-expanded results. The latter trend might however seem counter intuitive, given that a greater expansion should lead to higher velocities at the outflow. A possible explanation for this behavior can be provided by doing a qualitative analysis of the flow field based on Mach and ∇p contours; both type of plots for an under-expanded, the matching and over-expanded configurations can be found in Figure 4.7.

It can be observed that for under-expanded configurations, the contour plots exhibit a flow structure assimilating an expansion-fan; an expected consequence of a higher pressure level at the nozzle exit than the back pressure. When the theoretical post-expansion ratio ($\beta_{PE,BC}$) is too large, it seems that the system simply cannot achieve the prescribed total expansion. Nonetheless, the flow in these cases also presents shock-wave and the overall structure could be described as cluttered.

The matching configuration shows a neater ∇p contour, assimilating the expected TE flow structure (cf. Figure 2.10 and Figure 2.14). There seems however that a separation bubble occurs in the semi-bladed area from the line emanating from the blade wall in that region, which probably represents a weak shock. Based on the reviewed literature, a separation bubble was expected to be caused by the incidence of the oblique shock from the adjacent blade. It would be important to retrieve the cause of this apparently unforeseen shock. Moreover, both under-expanded and matching configurations exhibit relatively high flow uniformity in the Mach contours.

Continuing the analysis, the over-expanded configuration shows a different flow structure altogether; a TE region with a strong shock oblique shock and smaller expansion-fan. The area where the shock impinges in the adjacent blade wall seems to be chaotic, and it can be expected that the BL separates in this region. The strength of the shock could serve as an explanation for the reduction of M_2 for over-expanded configurations: there is a large expansion in the nozzle region followed by a strong shock, which would return the flow to a

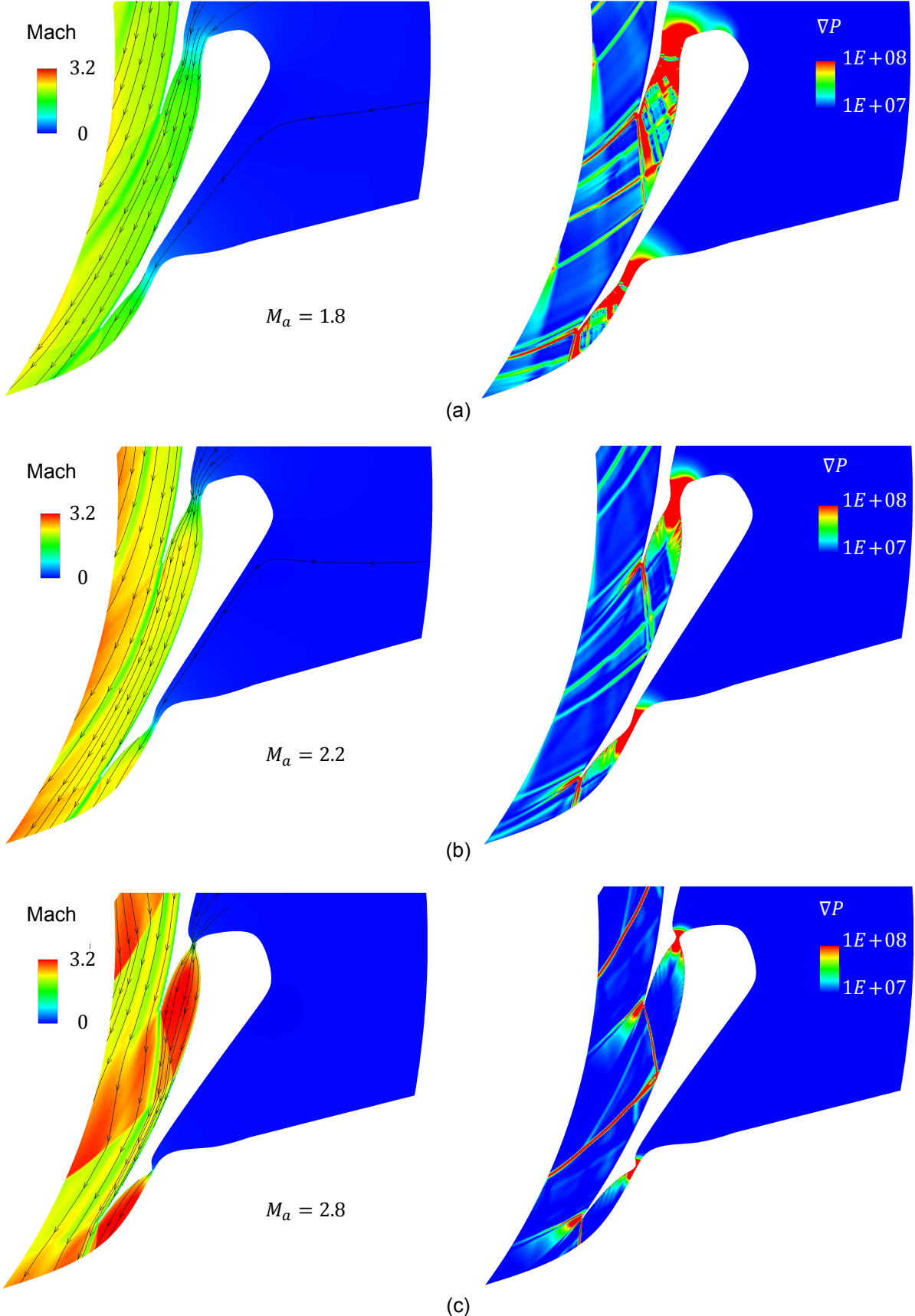


Figure 4.7: Mach and pressure gradient contours of an (a) under-expanded (b) matching and (c) over-expanded blade configurations

higher pressure level, but with a lower velocity.

Another, and arguably the most important, relation which can be derived from Equation 2.1 is the dependence between the expansion process and the corresponding cross-sectional area. To understand how this fundamental association is transposed in more complex radial geometries, the same data present in Figure 4.5 has been plotted against the relevant area ratio. In this case, it was expected to be the throat-to-outflow ratio O/S , which resulted in the plots found in Figure 4.8.

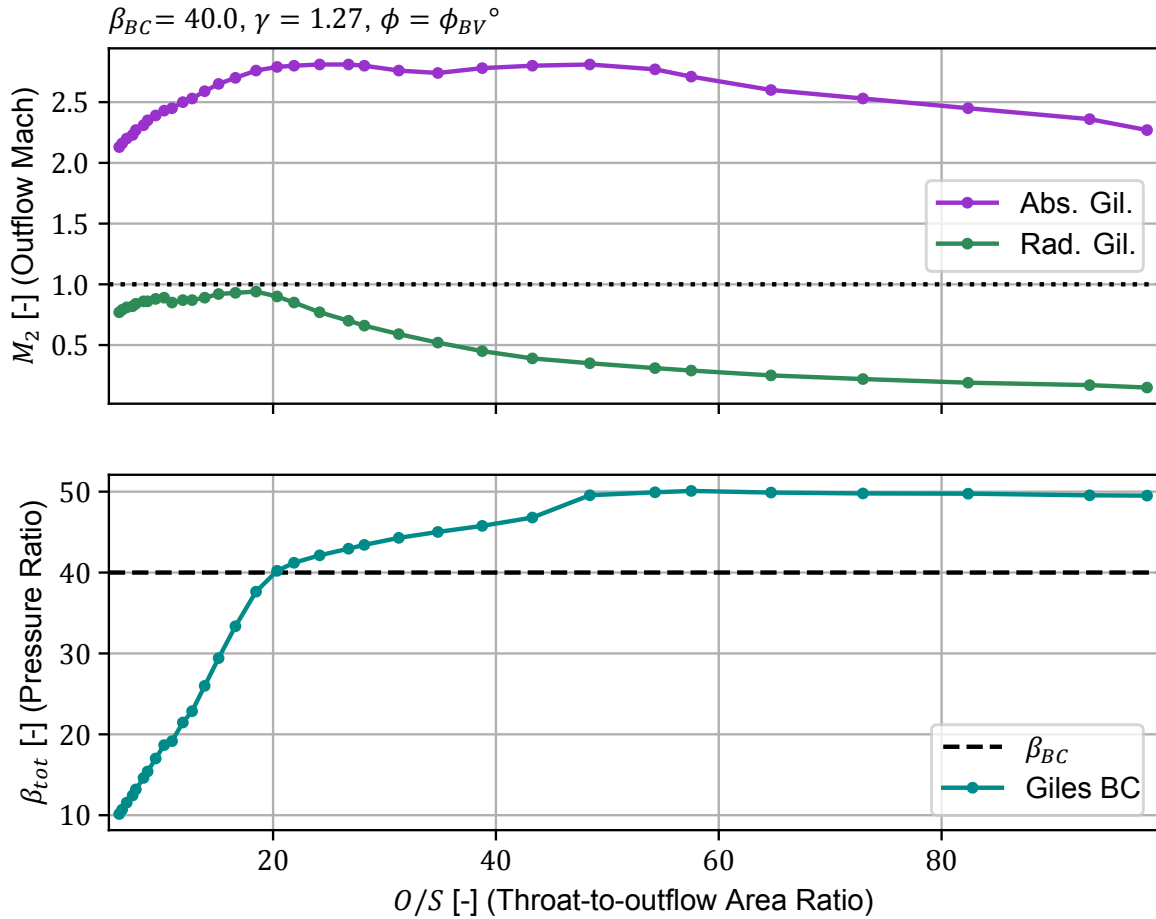


Figure 4.8: Simulation results of outflow Mach and stage pressure ratio for blade configurations with varying M_a plotted against the relevant area ratio

As expected, the change of variable modified the shape of the curve itself: the under-expanded region resembles the expansion line of an isentropic process, while the over-expanded region retains its shape. This would suggest that the area ratio is more relevant for the under-expanded region, while on the other hand, the over-expansion appears to be influenced by another property.

Under-expanded configurations would not be considered valid from a design point of view, given that they would lead to unusual high radial supersonic velocities. Nevertheless, it appears to be important to understand what exactly determines this behavior, to find geometries which will result in matching or over-expanding configurations. This is of course assuming that despite the pressure difference that would result in the rotor inlet, over-expanded configurations can be considered valid designs.

For this reason, four additional runs for the same variable within the same range were performed for different imposed pressure ratios. This was achieved by varying the back pressure prescribed in the outflow boundary. These results are shown in Figure 4.9.

It can be observed that as the imposed β_{BC} increases, more of the configurations be-

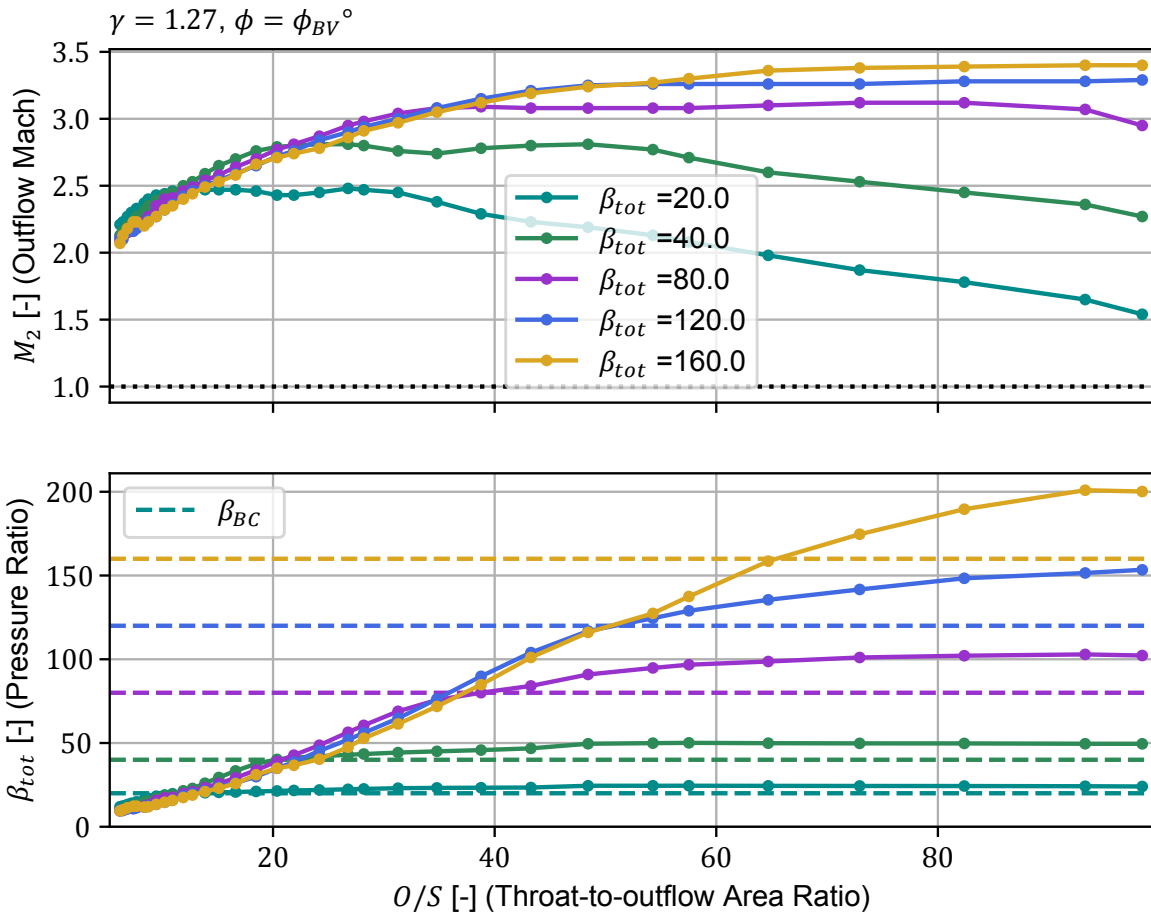


Figure 4.9: Simulation results of outflow Mach and stage pressure ratio for configurations with varying M_a , for different values of β_{BC} , plotted against the relevant area ratio

come under-expanded. Similarly, it can be seen in the figure that the overshoot of the over-expanded configurations becomes larger for higher values of β_{BC} . It can be noted that for larger imposed pressure ratios, when more configurations are under-expanded, the resemblance of the resulting trend with an isentropic expansion line becomes even larger. This leads to suspect that the shape of the curve for under-expanded blades is influenced by the fluid properties. The largest influence should come from the heat capacity ratio γ , which appears as an exponent in Equation 2.1.

To illustrate this more clearly, the data points of all the under-expanded results from each of the runs were plotted together as a scatter and fitted using polynomial functions. The result of this procedure can be found in Figure 4.10. A 2nd order polynomial was used to fit the data given that $1 < \gamma < 2$. The Mach values were also fitted, using a 3rd and 1st order function for the absolute and radial components respectively. These results add more evidence for the previously made claims regarding the expansion behavior of under-expanded blades.

As discussed previously in subsection 4.2.1, varying M_a only leads to changes in the throat width; the area lengths A and L are determined by other variables and the outflow boundary length S has been kept constant. Therefore the only ratio being varied would be O/S , hinting its role as a constraint in the expansion process.

Therefore, another study was done in order to substantiate the relevance of the ratio O/S . Because the relevance of the throat width on the system should be undisputed at this point of the study, varying S seemed as the obvious choice for this verification. For practical reasons it was decided to vary this parameter by modifying the radial position of the outflow boundary

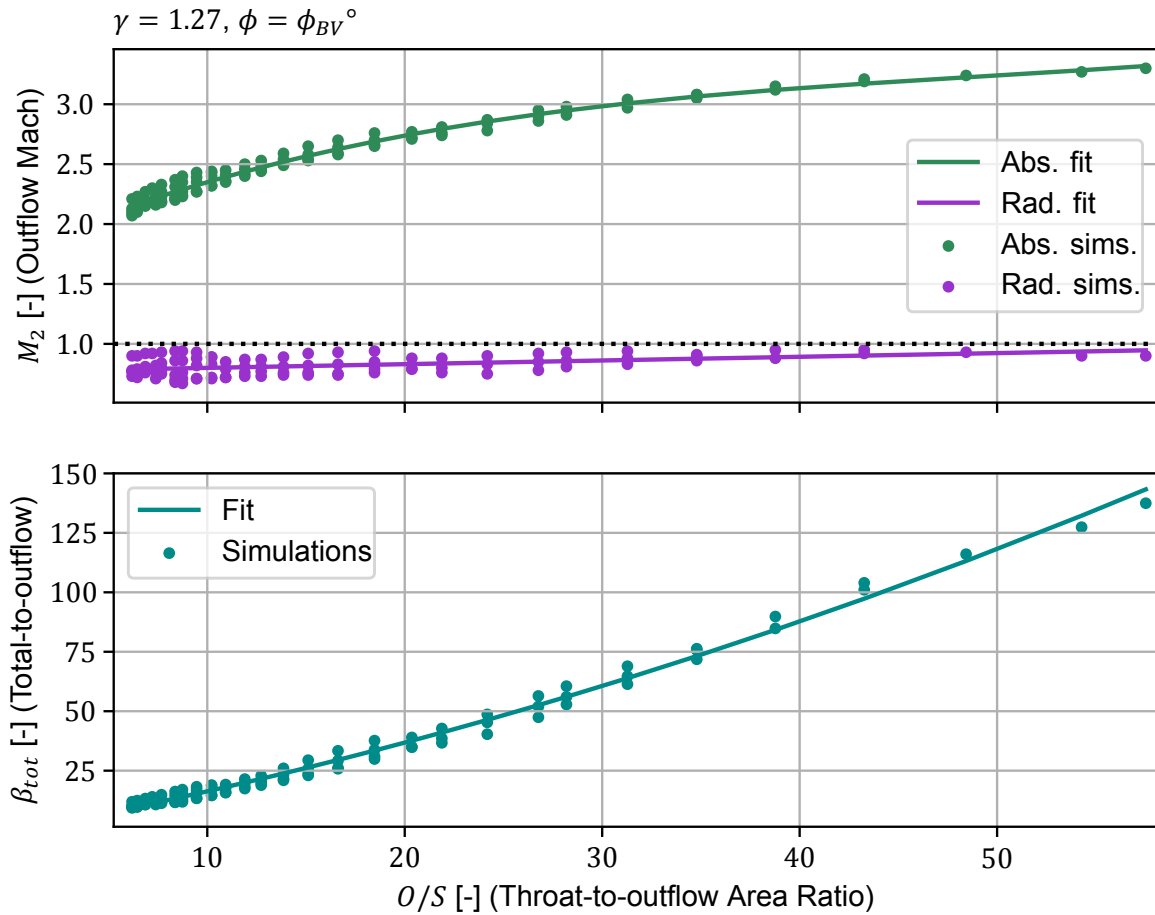


Figure 4.10: Fitted simulation results of outflow Mach and stage pressure ratio for under-expanded configurations

(R_2). The results for the original run and two other values of R_2 are visible in Figure 4.11.

The main disadvantage of changing R_2 is that small changes to O/S are possible. Additionally, the modification of R_2 also changes the size of the mixing plane, the effects of which cannot be easily discerned from the change in area length S on the flow behavior. In any case, the three lines show a similar trend for each of the tested values for under-expanded configurations, with the variations becoming larger for over-expanded ones. Looking more closely it can be observed that the lines are slightly shifted in the horizontal direction in the under-expanded region. This could be due to the previously discussed change in radial gap size.

Nevertheless, the three lines cross the β_{BC} line at almost exactly the same point. This assertion also remarks the importance of the previously defined $M_{a,\beta}$, mainly due to its influence on the geometry of the blades. All of this could suggest that the expansion behavior of the stage exhibits such a behavior due to an unexpected, but foreseeable effect: given the supersonic nature of the flows, information cannot travel upstream to influence the incoming flow, making the area ratio an additional geometrical constraint on the system. However, the claim of the expansion process only being influenced by the area ratio O/S cannot be made conclusive at this point.

Up to this moment, mainly under-expanded trends have been treated extensively. However, these lines are only relevant to find the configurations which will lead to matching or over-expanded pressure ratios. The over-expanded lines on the other hand do not seem to show behavior attributable to any of the previously considered parameters. The first piece of analysis related to this group is presented in Figure 4.12. This plot shows the calculated pressure ratio of a blade configuration with fixed degree of nozzle expansion (in this case

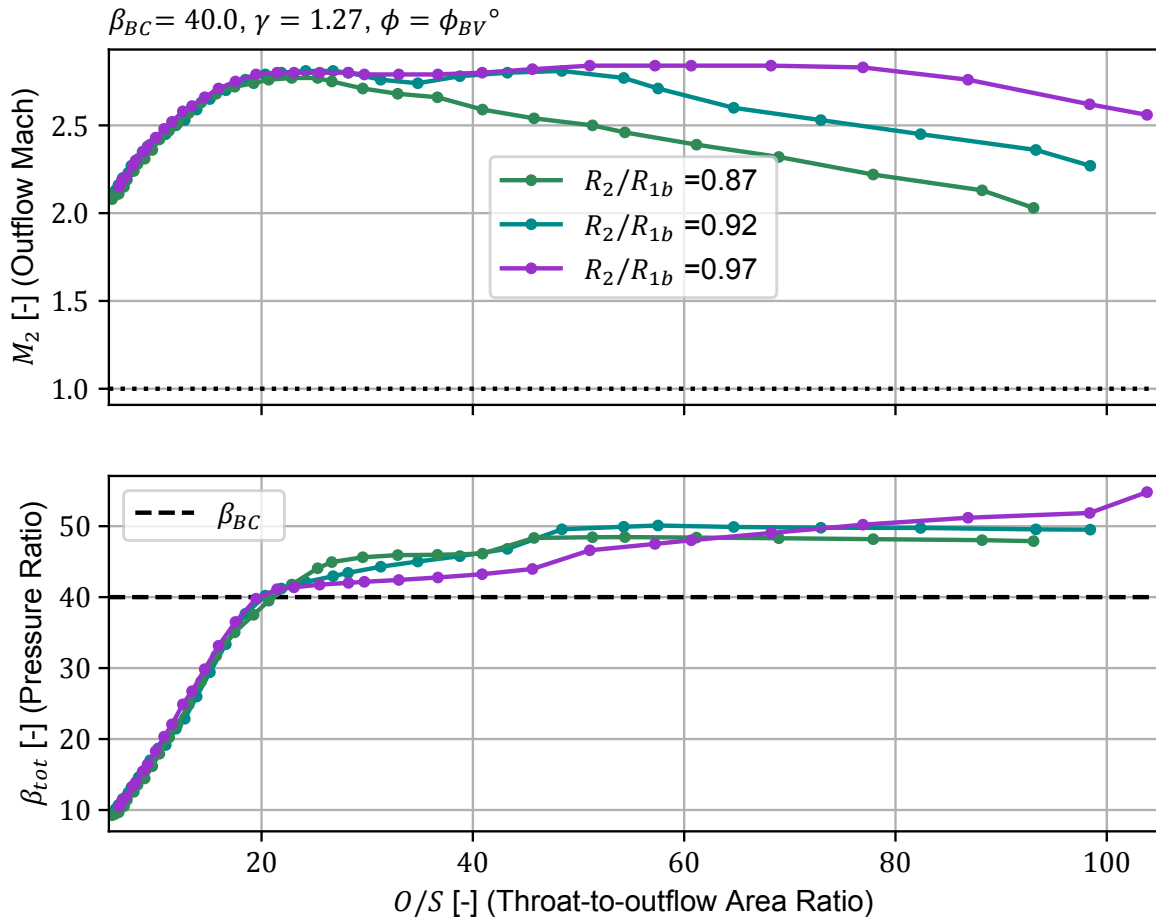


Figure 4.11: Simulation results of outflow Mach and stage pressure ratio for blades with varying nozzle design Mach and different outflow radius, plotted against the relevant area ratio

value $M_a = 2.2 = M_{a,\beta}$) for a range of different imposed back pressures, plotted against the resulting pressure ratio of the BCs.

What is interesting about this plot, is that this specific blade configuration matched the original imposed stage pressure ratio (cf. Figure 4.5). What can be observed in the results is that the calculated pressure ratio follows closely the $y = x$ line (delineated with dots in the figure), where the calculated value follows the imposed value, until the matching pressure ratio is reached. From that point on the calculated pressure ratio seems to attempt to converge to a certain value, in this case $\beta_{tot} \approx 40$, as depicted by the horizontal dotted line. Although no concrete claims can be made based on these results, it does provide more evidence about the additional constraint present in the system, which is expected to be geometric and which could be attributed to the supersonic nature of the flow.

Finally, the main concern with the overshoot of the expansion process exhibited by some configurations is that it removes the assumption that the nozzle expansion, and therefore the post-expansion ratio β_{pE} , can be varied independently for a constant pressure level between the inflow and the outflow boundaries. The latter was predicted using the derived expression in Equation 2.29.

To understand how these parameters are actually related in practice, the PE ratio and the pressure ratio difference for all over-expanded configurations can be determined and plotted together. The result of this process can be found in in Figure 4.13.

What is first interesting to notice about this plot, is that the behavior over the over-expanded line itself seems to be divided again into two sections (cf. Figure 4.5), depending on the degree of PE in the stage. On the left hand side of the vertical unity line are configu-

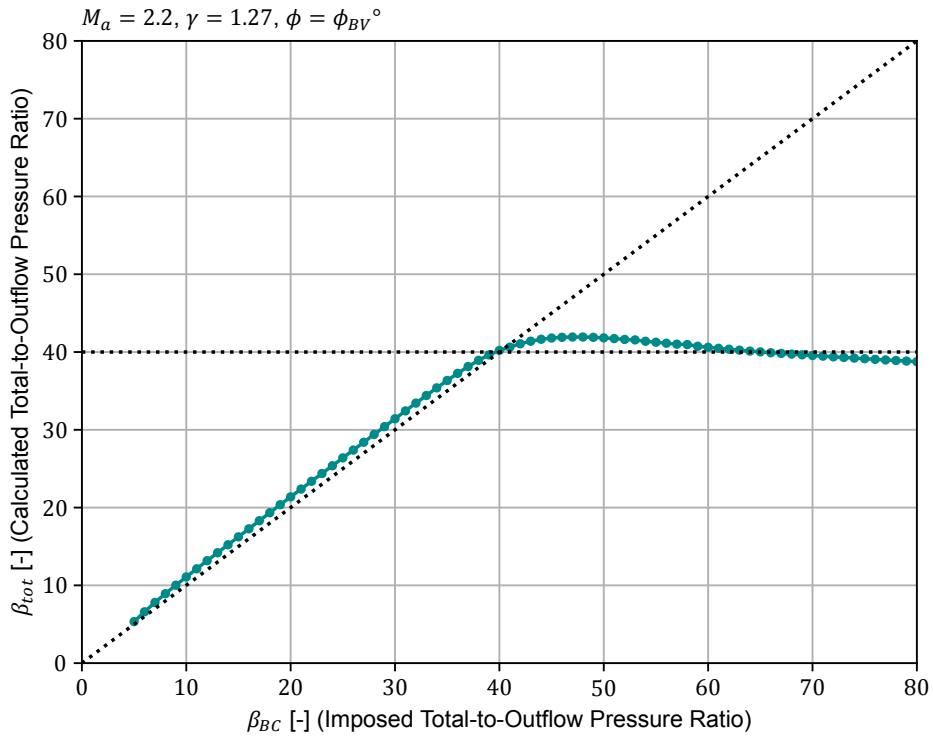


Figure 4.12: Simulation results of β_{tot} for a blade configuration tested under different stage pressure ratios (by varying P_2)

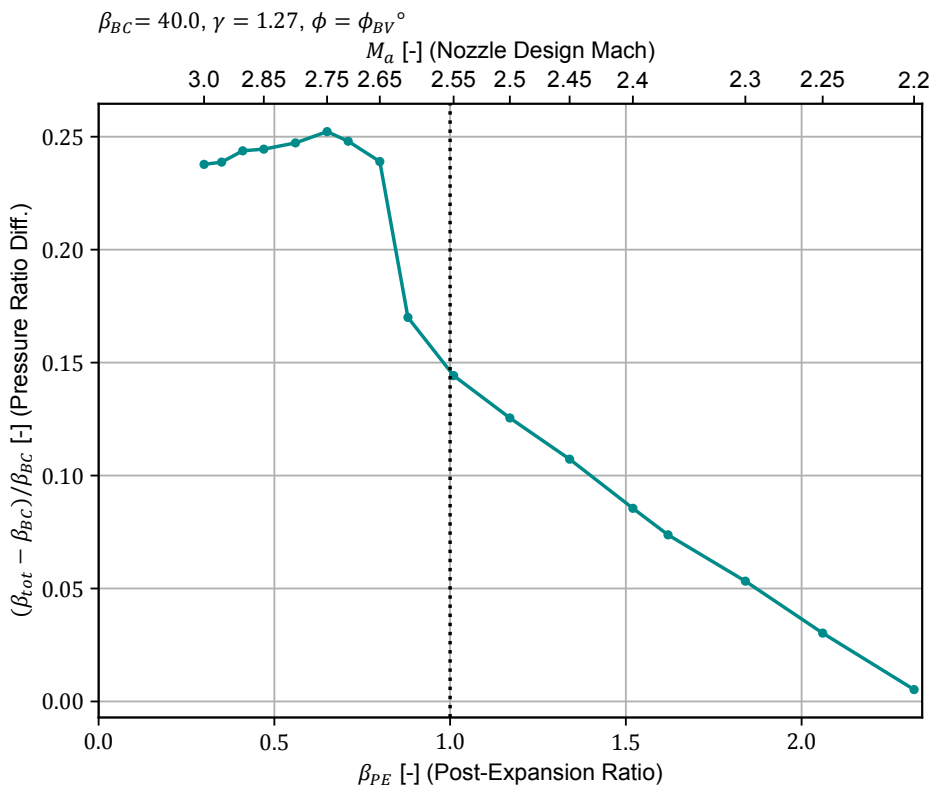


Figure 4.13: Simulation results of the difference between calculated and imposed total-to-outflow pressure ratio for blades with varying M_a plotted against the resulting post-expansion ratio

rations resulting in re-compression in the PE region; to the right are configurations having post-expansion. What is remarkable is that the over-expansion and post-expansion seem to be linearly related.

4.2.3. Stator Performance

Performance, quantified in this case by the flow deviation, entropy generation (using the coefficient s_{gen} previously defined in Equation 2.6) and the stage pressure ratio have been plotted against M_a , the variable of the main experimental run. The plots can be found in Figure 4.14.

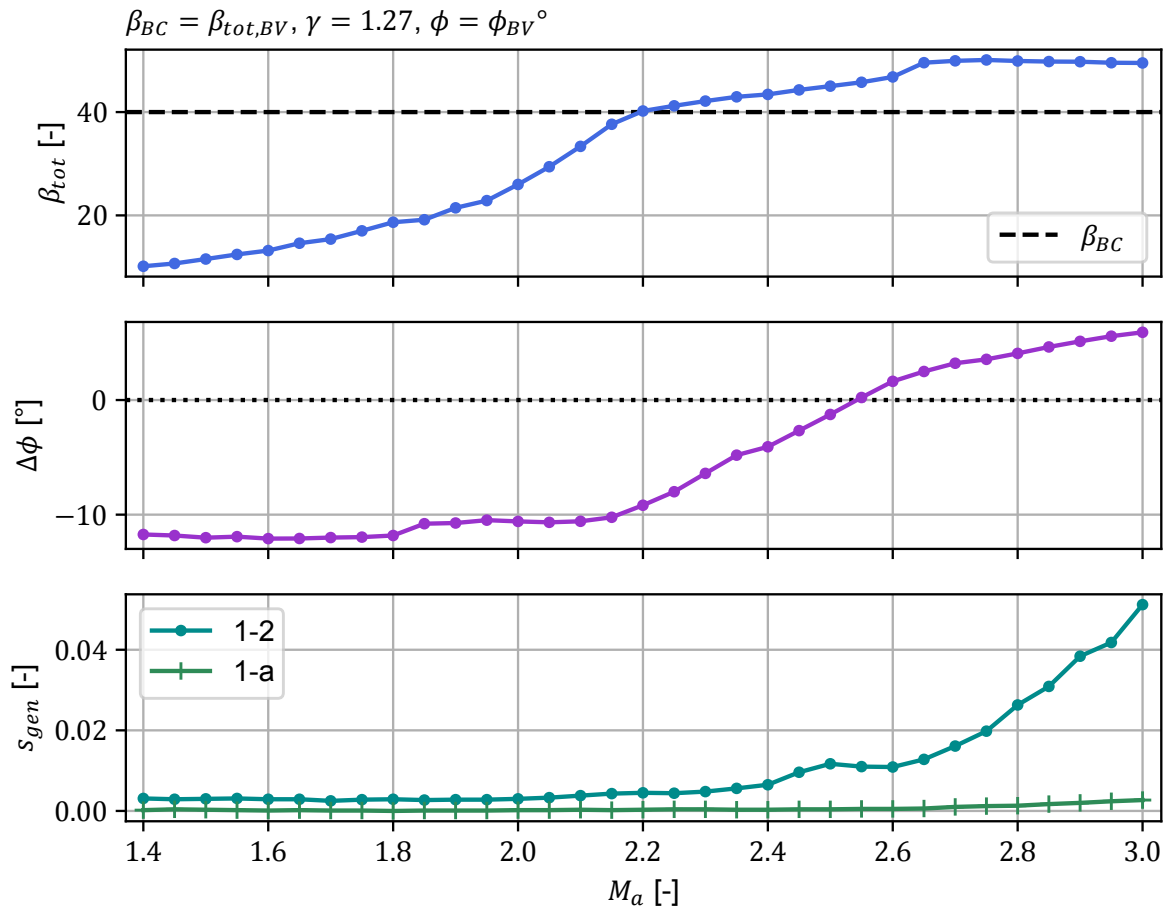


Figure 4.14: Simulation results of stage pressure ratio, flow deviation and entropy generation (from top to bottom respectively) for configurations with varying M_a

Firstly, it is interesting to notice that the flow deviation (mid plot) remains at a somewhat constant value, which in this case is highly negative (towards the outflow boundary). As M_a approaches the previously defined $M_{a,\beta}$, the deviation commences to increase, changing in its steepness at some point. Unsurprisingly, this change occurs when the overshoot in pressure ratio (upper plot) becomes constant. It can be stated that the flow deviation trend adds another piece of information to complete the picture of the expansion behavior discussed in the previous subsection: the high deviation towards the outflow boundary will inevitably lead to a larger component of the radial Mach.

The lowest plot in Figure 4.14 shows the entropy generation along the analyzed blades. In this plot both the intermediate loss generation until the nozzle exit and the complete stage losses have been plotted. It should be noted that the losses until the nozzle exit remain negligible with respect to the total entropy produced. This could however be attributed to the fact that the viscous losses, which are expected to be the largest share of the losses until the

nozzle exit, could only be measurable downstream where they become indiscernible from the mixing losses.

Focusing on the overall losses and referring back to the hypothesis presented in section 2.3 and illustrated in Figure 2.15, the plot for entropy generation shows a different trend than previously expected; there is a seemingly increasing trend of losses with increasing degree of expansion in the nozzle. Nevertheless, it has already been stated in subsection 4.2.1 and subsection 4.2.2, that several of the initial assumptions did not hold for the actual test conditions.

For this reason, it seems appropriate to only consider "valid" designs for the performance analysis. As previously mentioned, this definition entails only matching or over-expanded configurations. Likewise, it becomes now useful to continue the analysis in terms of the resulting post-expansion ratio β_{PE} . To proceed in this manner, the same data presented in Figure 4.14 has been plotted against the calculated β_{PE} and shown in Figure 4.15. This time the calculated pressure ratio has been replaced by the resulting outflow Mach.

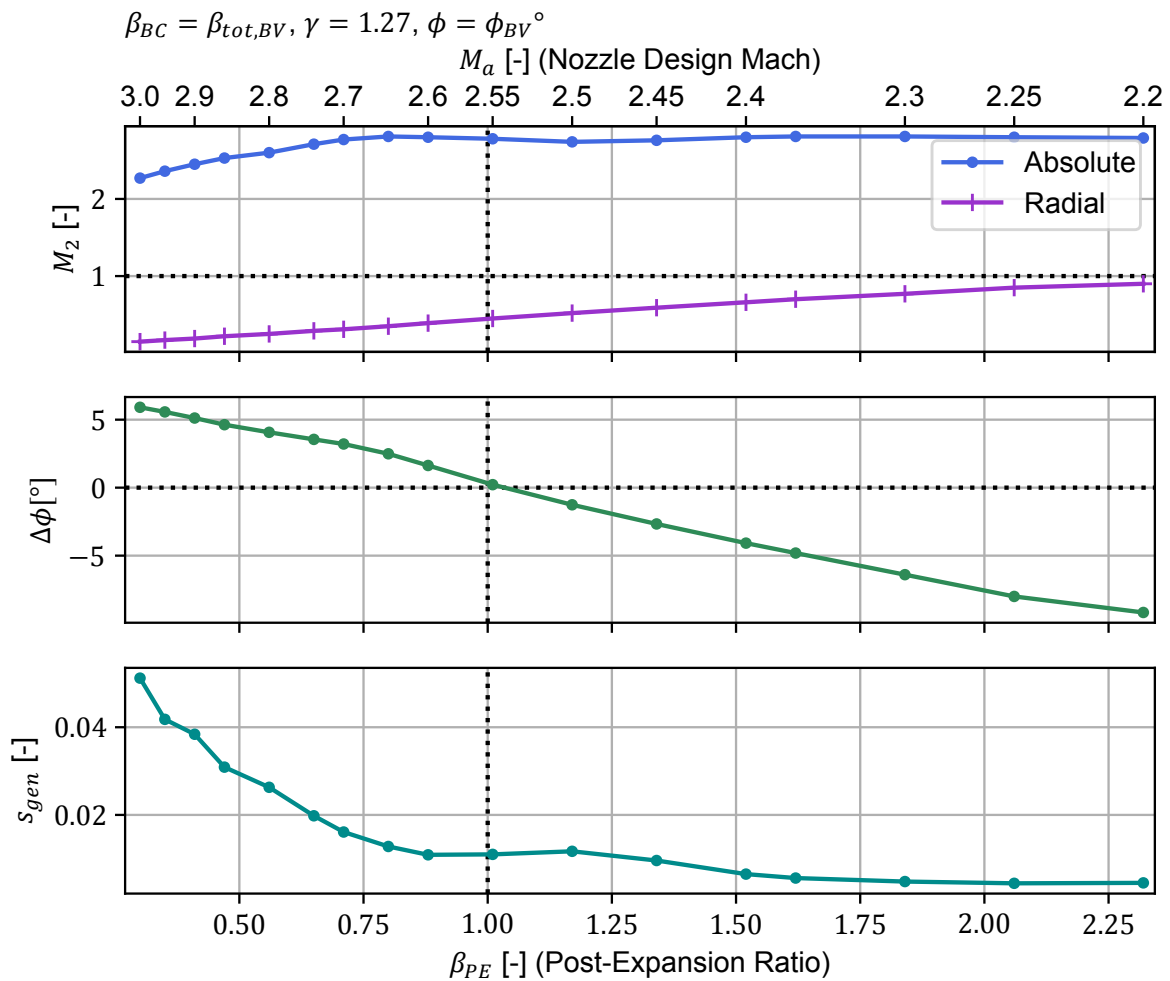


Figure 4.15: Simulation results of outflow Mach, flow deviation and entropy generation (from top to bottom respectively) plotted against the calculated post-expansion ratio, for blades with varying M_a

The vertical lines in each plot represent the points where the post-expansion ratio has a value of unity: in other words, the nozzle exit pressure equals the pressure level at the outflow. For each plot, the region located at the left hand side of this line, contains configurations which exhibit recompression in the PE region: the pressure level at the nozzle exit was lower than the back pressure. Similarly, configurations on the right hand side undergo an additional expansion in the semi-bladed region and mixing plane; the so called

post-expansion.

Although based on the same results, this plot provides further information regarding the blade performance. It is first interesting to notice that when plotted against this parameter, the flow deviation seems to exhibit linear behavior. It was expected from the analysis of convergent axial blades discussed in subsection 2.2.3 that at least the deviation should become zero for no PE ($\beta_{PE} = 1$).

Here again, additional information can again be retrieved from a qualitative study of contour plots for a recompressive, no PE and post-expansive configurations, which have been gathered in Figure 4.16. In a similar fashion to the previous contours (cf. Figure 4.7), the increasing value of M_a leads to an increase in the oblique shock emanating from the TE. What is remarkable however, is the existence of shocks when there is no post-expansion (Figure 4.16(b)): earlier studies for axial configurations suggested that $\beta_{PE} = 1.0$ would lead to no shocks as there would be no pressure difference between the nozzle exit and the stator outflow. However, this configuration does not seem to have the weak shock starting in the semi-bladed region before the impingement of the oblique shock.

The flow structure of the three type of Post-expansion does give some insights on the performance trends visible in Figure 4.15. Given that decreasing values of M_a lead to higher PE ratios and that it seems that expansion fans are more efficient than over-expansion and followed by recompression, that higher values of β_{PE} will be related to higher performance. This is also true for the flow uniformity. However, it remains difficult to assert the cause of the apparent plateau in entropy generation for both trends.

To establish the generality of the PE ratio as a determinant parameter in the design of C-D stators, the data resulting from simulating a selected configuration ($M_a = M_{a,\beta} = 2.2$) for varying values of imposed back pressure, and therefore differing stage pressure ratio, have been plotted against the resulting PE ratio in Figure 4.17.

Although an expected result, it remains remarkable that similar trends with respect to the variation of M_a (cf. Figure 4.15) are portrayed in this plot. First, in both cases the outflow Mach number seems to converge to a certain value, while the radial component always remains below unity. Similarly, the flow deviation retains its apparent linear behavior and a similar entropy production trend is visible: decreasing losses from re-compression towards no post-expansion and a higher performance plateau for larger PE ratios.

Again in this case, the analysis can be taken a step further aided by studying relevant contour plots. These can be found in Figure 4.18. Aside from what seem to be additional weak discontinuities in each of the ∇P contours and lower velocities in the Mach contours, each pair of plots resembles closely the corresponding couples already shown in Figure 4.16. This can be said both in terms of flow uniformity (in the Mach contours) and flow structure (in the ∇P contours).

Finally, the same exercise was repeated for different blades, ensuring to capture their entire range of possible PE ratios. These results have been collected and plotted in Figure 4.19.

As anticipated, similar trends are identifiable for each of the tested blades. Nonetheless, some important additional observations can be made using the information of these plots: the trends are shifted for differing values of M_a and the range of possible post-expansion ratios varies for a given degree of nozzle expansion. Regarding the first assertion, the trend shift is upward (and somewhat to the right) in the entropy production plot. This means that overall for a given ratio of post-expansion, blades with higher M_a will perform more poorly, while maintaining almost a constant level of flow deviation.

Given that the throat lengths are scaled for this change in parameter, it is not possible to discern between the effect of the increased shock strength due this parameter and the simultaneous decrease in mass flow, which according to Equation 2.15 should lead to a decrease in losses.

Furthermore, related to the second previously made assertion, the post-expansive high performance plateau is present in all the examined trends, including the main run for variable M_a . However, when varying the post-expansion by changing the back pressure of a fixed blade configuration, lower M_a nozzles will allow a larger range of possible post-expansions in the PE region, as can be observed in the plots. Hence, when only considering performance in terms of loss generation, there is some apparent freedom to choose back pressures which

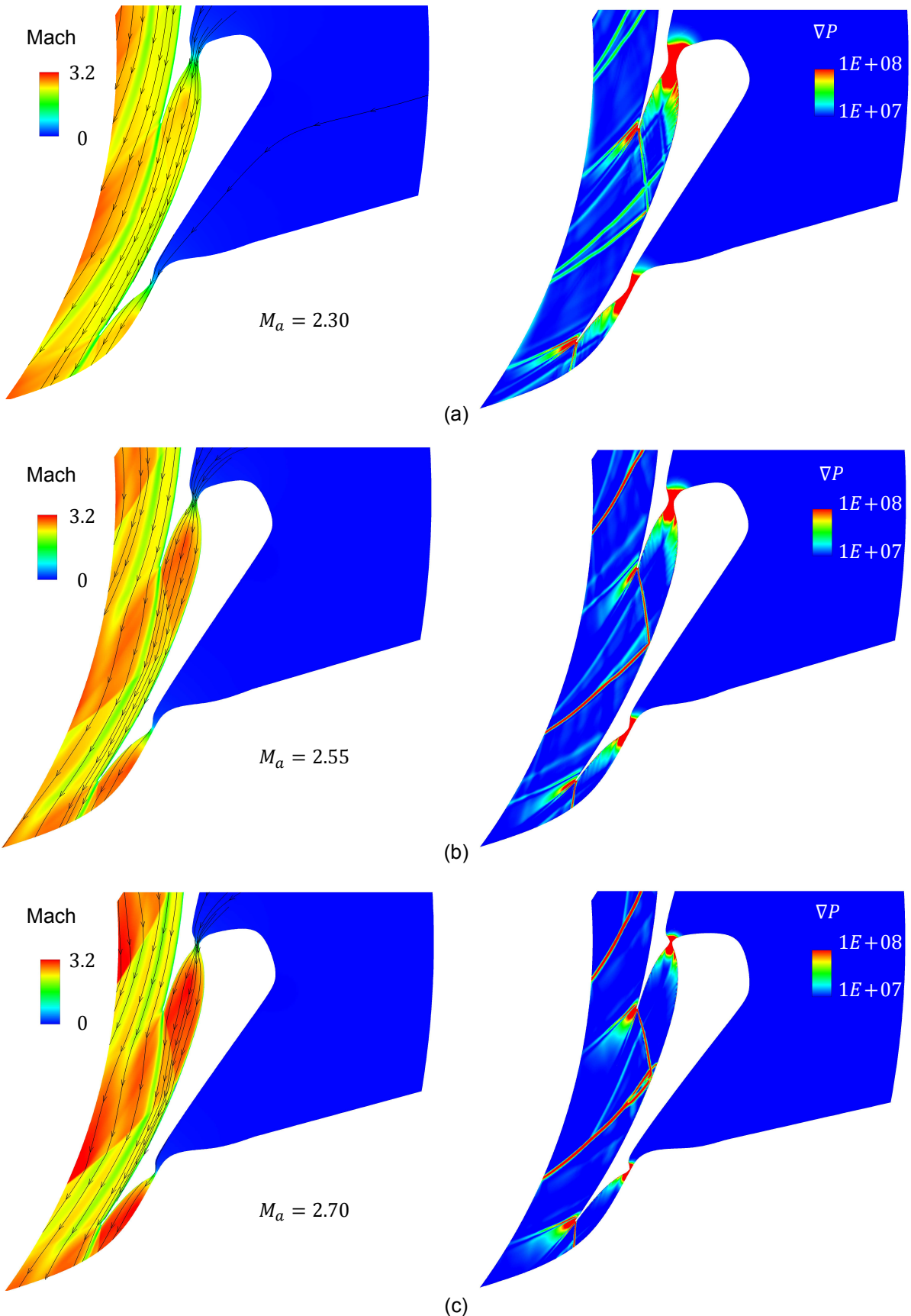


Figure 4.16: Pressure gradient and Mach contour plots of blade configurations with differing M_a leading to (a) re-compression (b) no post-expansion (c) post-expansion in the PE region

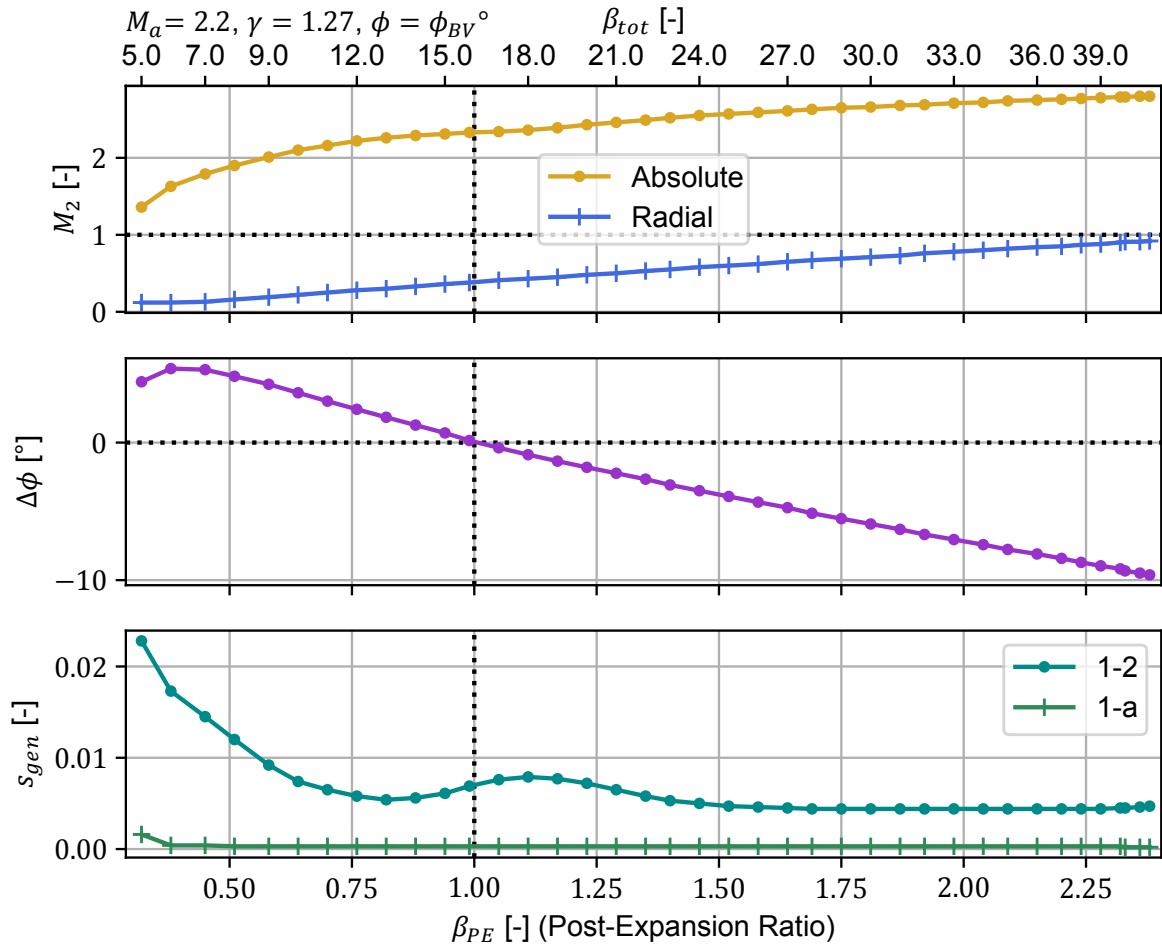


Figure 4.17: Simulation results of outflow Mach, flow deviation and entropy generation (from top to bottom respectively) plotted against the PE ratio (for varying imposed back pressures)

would lead to suitable designs. This in turn would translate into a larger space to choose the degree of reaction of this type of turbine.

Nevertheless, when looking at performance in terms of overall fluid conditions provided at the stator outflow, which could be considered the goal of stator design, to provide suitable flow conditions incident to the rotor blades, a lower flow deviation might be desirable. This would mean, that at least for this test case, the optimal configuration could be considered to be the first value which reaches the performance plateau: this configuration would have the lowest losses, together with a lower over-expansion and flow deviation.

4.2.4. Supplementary Variable Monitoring

Simplifications were possible in the analysis of section 2.3 by assuming that some variables could be kept constant throughout the experiments. However, already when describing the underlying procedure of the RST tool in subsection 3.2.2, some doubts about the feasibility of these assumptions arose. This was later confirmed in subsection 4.2.1, where the results showed that a simultaneous scaling of the throat width 0 occurs when varying some of the relevant design parameters. This subsection provides some additional information regarding the deviation from the original assumptions.

As expected from the previously derived Equation 2.31 in section 2.3, the changes in the throat dimensions will be mostly influential for the viscous dissipation losses. The main reasons for this presumption is that the throat width will influence the state of the boundary layers and fix the choked mass flow of the system. For this reason, the throat Reynolds

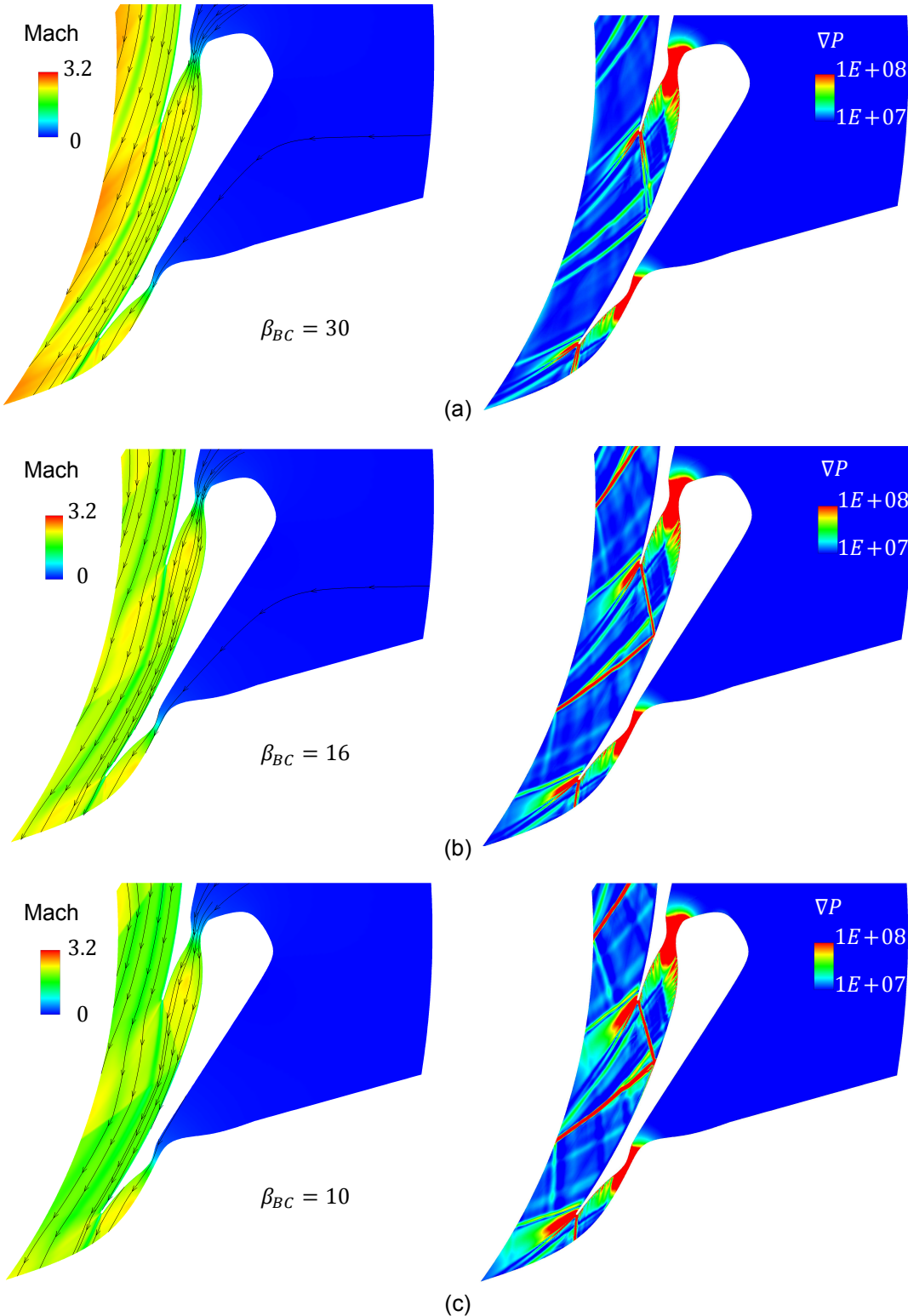


Figure 4.18: Pressure gradient and Mach contour plots of fixed blade configurations ($M_a = 2.2$) simulated for different stage pressure ratios (by varying the imposed back pressure), leading to (a) re-compression (b) no post-expansion (c) post-expansion in the PE region

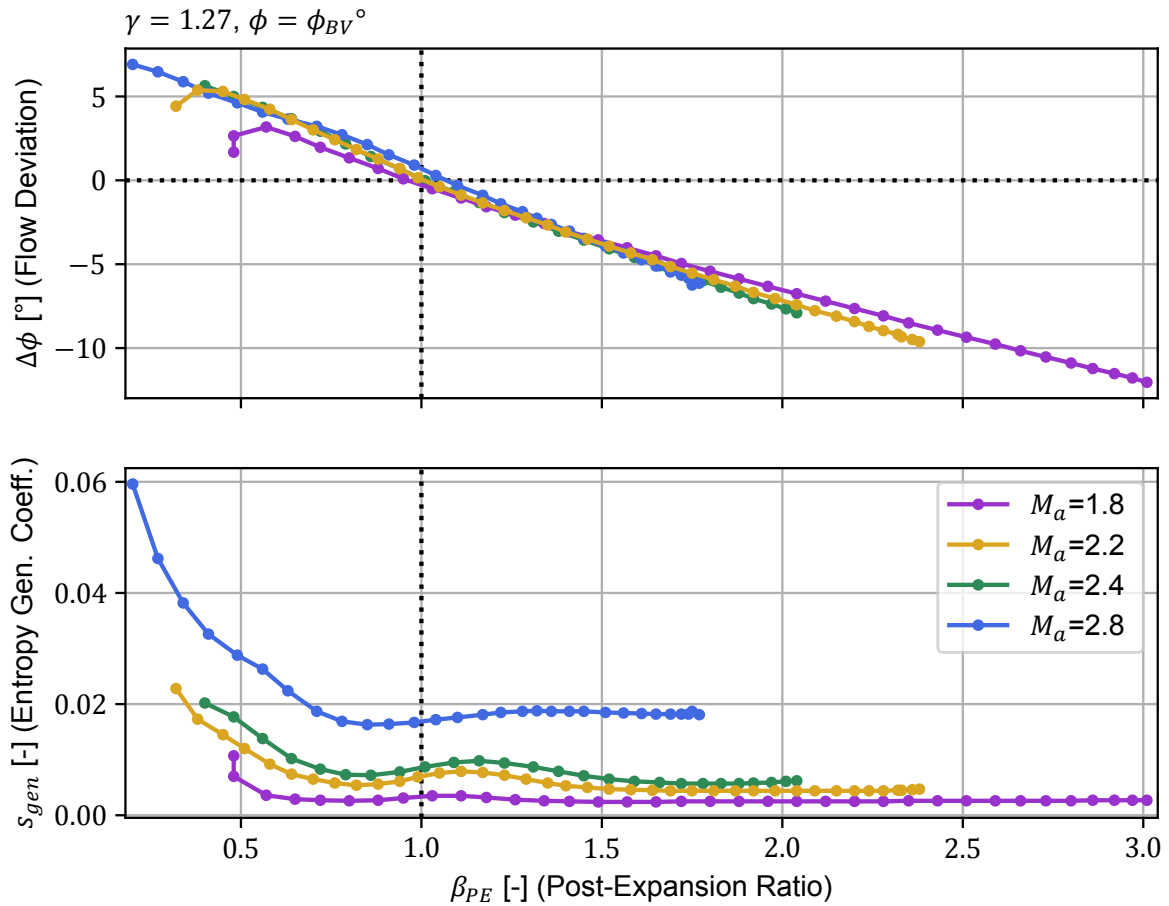


Figure 4.19: Simulation results of flow deviation and entropy production of different blades plotted against the res (for varying imposed back pressure)

number and the mass flow have been monitored for the main set of blades considered in this study, with varying M_a . These results have been collected together in Figure 4.20.

It can first be noticed that mass flow, mainly determined by the choked flow conditions and therefore directly dependent on the throat width, decreases to under 20% of the largest value, for the lowest M_a (widest throat). A quantification of the effects of this drop in mass flow could not be carried out during this project, but they should be taken into close consideration for future work. Second, although there is a substantial change in throat length in the set of configurations considered, the Re_t values are concentrated in the range between $10^5 - 10^7$ approximately.

To test the possible influence of this parameter, a run varying the fluid viscosity was performed, the results of which are shown in Figure 4.21.

It can be observed that there is a wide spread in terms of losses for this parameter. Although this variation was done artificially, it does provide some useful insights. For the range considered in Figure 4.20, it is safe to assume that this parameter will not cause as much variations in the performance. This can lead to conclude that the throat dimensions will mainly be relevant due to the induced changes in the mass flow magnitude.

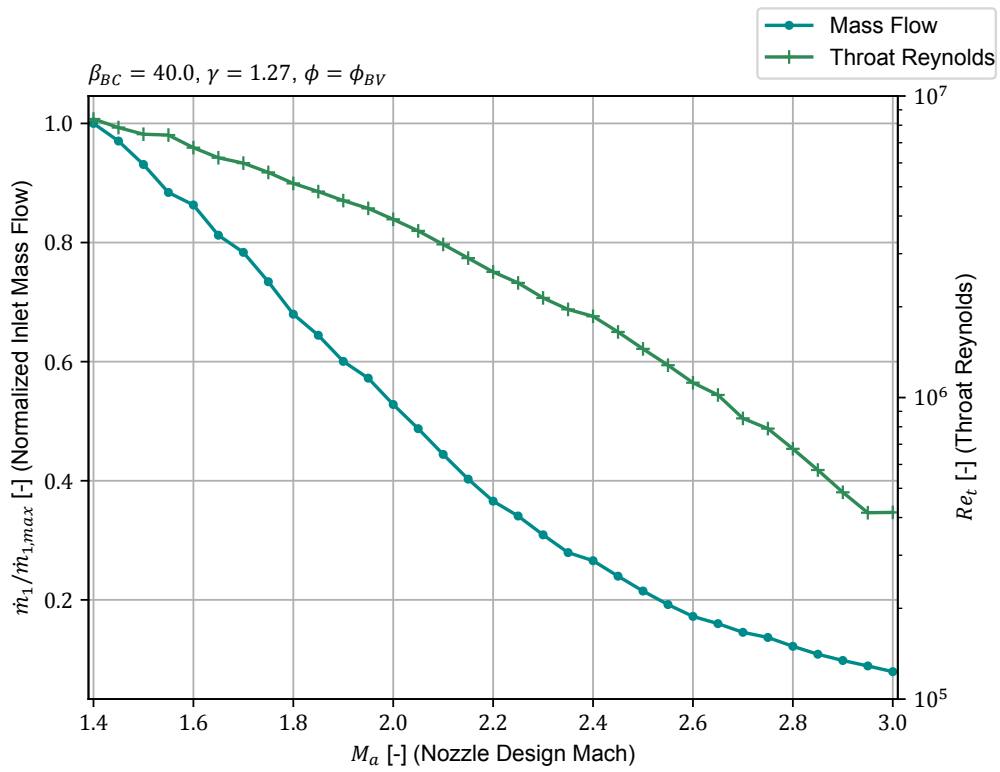


Figure 4.20: Simulation results of throat Reynolds number and normalized mass flow for variations of nozzle design Mach

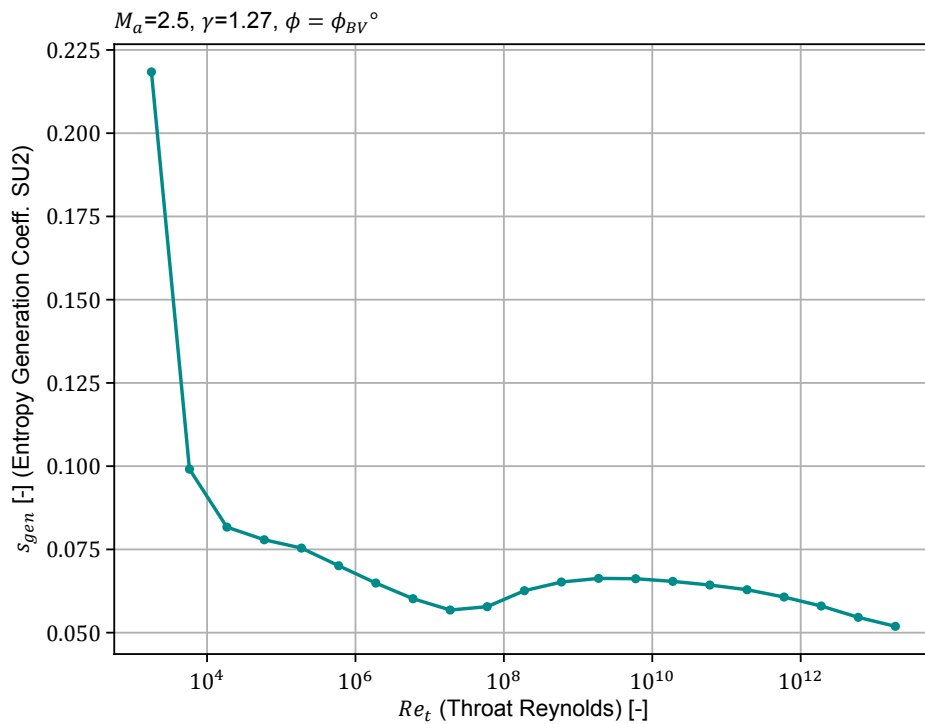


Figure 4.21: Simulation results of entropy generation for values of artificially varied throat Reynolds on a fixed blade configuration

5

Research Closure

To finalize this report, a summary of the findings stemming from answering the research questions and working towards the project goal are presented in section 5.1. Likewise, advice aimed at researchers planning to carry this work forward has been gathered in section 5.2

5.1. Conclusions

Referring back to chapter 1, the aim of this project was pursued using a set of research questions. A thorough review of the available literature provided information for answering the first question and led to the formulation of a research hypothesis. This was then the main tool for answering the second question.

To this end, an automated blade and simulation design chain has been developed and successfully implemented to produce numerous CFD simulations. This allowed a first of its kind exploratory parametric study of radial C-D stator blades, providing useful insights for achieving the original goal. The findings, with respect to the research questions and goal, can be summarized as follows:

What are the significant loss mechanisms affecting the performance and flow characteristics of radially inward supersonic stator vanes?

It was assumed that analyzing 2D loss mechanisms would be relevant to this research, given that the objective was related to the preliminary design level. Pertinent literature revealed that viscous dissipation at the boundary layers and the mixing losses in the wake and the trailing edge region should be significant. The latter is dominated by the appearance of shocks, which will also interact with the boundary layer of the adjacent blade wall, and in some cases even induce flow separation. Hence, a degree of dependence will exist between both components of the overall loss.

By taking the theoretical analysis a step further, it was possible to identify that the region spanning from the stage inflow until the nozzle exit should be mainly affected by viscous dissipation, given that this loss characteristic will occur on the blade walls. On the contrary, the loss generation in the region covering the semi-bladed area and the mixing plane should primarily be a consequence of the mixing process. A trade-off between these two loss components was expected to exist based on the variation of a key parameter: the degree of expansion in the nozzle.

What are the important design parameters and the corresponding geometrical features which influence the relevant loss mechanisms?

For a given blade configuration and set of operating conditions, the most critical geometrical feature from a theoretical point of view is the throat-to-nozzle-exit area ratio. The corresponding design parameter is the nozzle exit (or design) Mach number, which controls this area ratio when using the MoC to design the nozzle contour. Moreover it was predicted

that the effects of this parameter could also be quantified by the post-expansion ratio of the stage.

Yet in practice it was found that an undesired scaling of the throat width occurred when varying the nozzle exit Mach. This rises additional complications by invalidating some initial assumptions used in the theoretical analysis. In first place, it led to variations in the calculated pressure ratio as compared to the imposed value. This could be a result of the effect of certain geometrical features on the flow when supersonic conditions are reached; only variations to the throat-to-outflow area ratio were present, providing evidence pointing to the influence of this parameter. Secondly, the mass flow in each of the set of blades varied considerably with changes in throat width. The fundamental theory showed that this value should have an effect on the viscous loss component of the blades.

Formulate preliminary design guidelines for supersonic radial inflow turbine stator vanes by studying the effect of relevant parameters on the blade's performance based on numerical computer simulations

By taking blade configurations matching or with larger pressure ratios than the imposed value, a performance analysis was carried out. The results showed an increase in overall entropy production with increasing nozzle Mach number. Moreover, when quantifying the performance in terms of the post-expansion ratio, interesting trends emerged. The flow deviation portrayed a linear relation with respect to this parameter. On the other hand, the losses showed a sharp decrease for ratios below one, with a small increase when approaching unity, after which a plateau of higher performance was reached for larger ratios.

These trends persisted even when manipulating the PE by changing the back pressure of the system. However, fixed blades with larger nozzle Mach numbers showed comparatively overall higher losses for equal ratios of PE. It was not possible, however, to quantify the effect of the changes in mass flow on the overall efficiency.

In order to delimit the preliminary design space, a set of expressions correlating the value of blade performance and behavior with the relevant design parameters is desired. To achieve this, further studies should be conducted. However, using the findings presented above, a set of dependencies has been derived which could be used to formulate mathematical expressions in the future. These have been presented in Table 5.1.

Table 5.1: Summary of dependencies between performance, behavior and relevant design parameters for fixed geometrical and operating conditions

Parameter	Dependency
β_{tot}, M_2	β_{BC}, M_a^*
β_{PE}	β_{tot}, M_a
ϕ_2	β_{PE}, ϕ
ζ	$\beta_{PE}, M_a \dagger$

*Scaling on throat width expected to be relevant

†Induced change in mass flow expected to be relevant

Once these relations are verified and properly quantified, they could be inverted to find the optimal value of M_a for specific conditions. It should be noted that it is important to first have a proper definition of valid design and the design priority of the blades.

5.2. Recommendations

Due to the time and resource constraints inherent to a master thesis, this project became a first step, albeit a useful one, but none the less a first attempt to find the sought for design guidelines. Relevant insights have been gathered through the production and interpretation of simulation data. However, there are still efforts that should be undertaken to reach the

final objective.

Therefore a set of tasks, which are believed to be relevant, if not necessary, to carry this research work forward, are proposed. These can be separated into three main groups: related to the design and simulation tools, for verification purposes and to generate additional data. However, before proceeding with these tasks, it is advised to define properly the concepts of optimal blade behavior and performance. This will likely change the actual amount of work left to be done.

Regarding the design tools, the following tasks are advised to be performed:

- Improve the robustness of the RST tool by removing the optimization procedure. This could be achieved by solving the geometrical constraints analytically;
- Consider the implementation of a more flexible meshing tool in the design chain for the study of geometries with large differences;
- Due to the criticality of the properties at the nozzle exit, implement the integration of these values completely based on existing software. The usage of *ParaView* is suggested, to maintain the open-source condition of the design chain;
- Add a functionality to the design chain to monitor the convergence of the simulation based on the residuals of relevant properties.

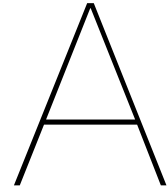
Similarly, additional verification of the results can be provided by doing the following:

- Verify the results, especially regarding the expansion process, using another CFD solver such as *ANSYS CFX*;
- Due to their simplicity, carrying out the simulations for a axial geometries of the same test case could provide a fundamental understanding of important relations;
- A more long term prospect, carry out experiments in a real test rig to validate the results.

Finally, in order to derive correlations to quantitatively predict the value of certain design parameters, more data is required. Some recommended experiments and tasks for this purpose are:

- Testing the effect of varying the throat-to-outflow area ratio by changing the number of blades;
- Perform additional inviscid simulations to break the losses down into its major components. This could aid in understanding the causes of the performance plateau;
- Determine the prevalence of the post-expansion ratio as a performance parameter by running simulations based on other test cases.

The first steps for finding suitable preliminary mean-line design guidelines have been set. If the proposed steps are undertaken with successful results, it would take the design of unconventional radial turbines one step closer to achieving its full potential.



SU2 Configuration File

```
%%%%%%%%%%%%%%%%%%%%%%%%%%%%%%%%%%%%%%%%%%%%%%%%%%%%%%%%%%%%%%%%%%%%%%%%
% %
% SU2 configuration file %
% Case description: Centrifugal turbine rotor %
% Author: M. Pini, S. Vitale %
% Institution: Delft University of Technology %
% Date: Feb 18th, 2013 %
% File Version 4.0.1 "cardinal" %
% %
%%%%%%%%%%%%%%%%%%%%%%%%%%%%%%%%%%%%%%%%%%%%%%%%%%%%%%%%%%%%%%%%%%%%%%%%
%
%
%
% ----- DIRECT, ADJOINT, AND LINEARIZED PROBLEM DEFINITION ----- %
%
% Physical governing equations (EULER, NAVIER-STOKES)
PHYSICAL_PROBLEM= RANS
%
% Specify turbulent model (NONE, SA, SST)
KIND_TURB_MODEL= SST
%
% Mathematical problem (DIRECT, ADJOINT, LINEARIZED)
MATH_PROBLEM= DIRECT
%
% Restart solution (NO, YES)
RESTART_SOL= NO
%
%
%
% ----- COMPRESSIBLE FREE-STREAM DEFINITION ----- %
%
% Mach number (non-dimensional, based on the free-stream values)
MACH_NUMBER= 0.05
%
% Angle of attack (degrees, only for compressible flows)
AoA= 0.0
%
% Free-stream pressure (101325.0 N/m^2 by default, only Euler flows)
```

```
FREESTREAM_PRESSURE= 3195000.0
%
% Free-stream temperature (273.15 K by default)
FREESTREAM_TEMPERATURE= 587.65
%
% Free-stream temperature (1.2886 Kg/m3 by default)
FREESTREAM_DENSITY= 1.2886
%
% Free-stream Turbulence Intensity
FREESTREAM_TURBULENCEINTENSITY = 0.1
%
% Free-stream Turbulent to Laminar viscosity ratio
FREESTREAM_TURB2LAMVISCRATIO = 100.0
%
% Free-stream option to choose if you want to use Density (DENSITY-FS) or
% Temperature (TEMPERATURE-FS) to initialize the solution
FREESTREAM_OPTION= TEMPERATURE_FS
%
% Init option to choose between Reynolds (default) or thermodynamics
% quantities for initializing the solution (REYNOLDS, TD-CONDITIONS)
INIT_OPTION= TD_CONDITIONS
%
%
%
% ----- REFERENCE VALUE DEFINITION ----- %
%
% Flow non-dimensionalization (DIMENSIONAL,
% FREESTREAM-PRESS-EQ-ONE, FREESTREAM-VEL-EQ-MACH, FREESTREAM-VEL-EQ-ONE)
REF_DIMENSIONALIZATION= FREESTREAM_PRESS_EQ_ONE
%
%
%
% ----- FLUID MODEL ----- %
%
% Different gas model (STANDARD-AIR, IDEAL-GAS, VW-GAS, PR-GAS)
FLUID_MODEL= PR_GAS
%
% Ratio of specific heats (1.4 default and the value is hard-coded for the
% model STANDARD-AIR)
GAMMA_VALUE= 1.06
%
% Specific gas constant (287.058 J/kg*K default and this value is
% hardcoded for the model STANDARD-AIR)
GAS_CONSTANT= 90.23
%
% Critical Temperature (273.15 K by default)
CRITICAL_TEMPERATURE= 591.75
%
% Critical Pressure (101325.0 N/m^2 by default)
CRITICAL_PRESSURE= 4126300.0
%
% Acentric factor (0.035 (air))
ACENTRIC_FACTOR= 0.2657
%
```

```

%
%
%
% ----- VISCOSITY MODEL ----- %
%
% Viscosity model (SUTHERLAND, CONSTANT-VISCOSITY).
VISCOSITY_MODEL= CONSTANT_VISCOSITY
%
% Molecular Viscosity that would be constant (1.716E-5 by default)
MU_CONSTANT= 1.644E-4
%
% Sutherland Viscosity Ref (1.716E-5 default value for AIR SI)
MU_REF= 1.716E-5
%
% Sutherland Temperature Ref (273.15 K default value for AIR SI)
MU_T_REF= 273.15
%
% Sutherland constant (110.4 default value for AIR SI)
SUTHERLAND_CONSTANT= 110.4
%
%
%
% ----- THERMAL CONDUCTIVITY MODEL ----- %
%
% Conductivity model (CONSTANT-CONDUCTIVITY, CONSTANT-PRANDTL).
CONDUCTIVITY_MODEL= CONSTANT_CONDUCTIVITY
%
% Molecular Thermal Conductivity that would be constant (0.0257 by
% default)
KT_CONSTANT= 0.08029
%
%
%
% ----- BOUNDARY CONDITION DEFINITION ----- %
%
% Navier-Stokes wall boundary marker(s) (NONE = no marker)
MARKER_HEATFLUX= (wall1, 0.0)
%
% Riemann boundary marker(s)
% Format inlet: ( marker, TOTAL-CONDITIONS-PT, Total Pressure, Total
% Temperature, Flow dir-x, Flow dir-y, Flow dir-z)
% Format outlet: ( marker, type, STATIC-PRESSURE, Static Pressure, 0.0,
% 0.0, 0.0, 0.0)
% MARKER-RIEMANN= (inflow, TOTAL-CONDITIONS-PT, 3195000.0, 587.65, -1.0,
% 0.0, 0.0, outflow, STATIC-PRESSURE, 1.0E+05, 0.0, 0.0, 0.0, 0.0)
%
% Non reflecting boundary marker
% Format inlet: ( marker, TOTAL-CONDITIONS-PT, Total Pressure, Total
% Temperature, Flow dir-x, Flow dir-y, Flow dir-z)
% Format outlet: ( marker, type, STATIC-PRESSURE, Static Pressure, 0.0,
% 0.0, 0.0, 0.0)
MARKER_GILES= (inflow, TOTAL_CONDITIONS_PT, 3195000.0, 587.65, -1.0, 0.0,
0.0, 0.0, 0.0, outflow, STATIC_PRESSURE, 0.8E+05, 0.0, 0.0, 0.0,
0.0, 1.0, 0.0)

```

```

%
% Kind of Average (ALGEBRAIC-AVERAGE, AREA-AVERAGE, MIXEDOUT-AVERAGE)
AVERAGE_PROCESS_KIND= MIXEDOUT
TURBOMACHINERY_KIND= CENTRIPETAL
NUM_SPANWISE_SECTIONS= 1
% Specify ramp option for Outlet pressure (YES, NO) default NO
RAMP_OUTLET_PRESSURE= YES
%
% Parameters of the outlet pressure ramp (starting outlet pressure,
% updating-iteration-frequency, total number of iteration for the ramp)
RAMP_OUTLET_PRESSURE_COEFF= (2000000.0, 10.0, 1000)
%
% Periodic boundary marker(s) (NONE = no marker)
% Format: ( periodic marker, donor marker, rot-cen-x, rot-cen-y,
% rot-cen-z, rot-angle-x-axis, rot-angle-y-axis, rot-angle-z-axis,
% translation-x, translation-y, translation-z)
MARKER_PERIODIC= (periodic1, periodic2, 0.0, 0.0, 0.0, 0.0, 0.0, 20.0,
0.0, 0.0, 0.0)
%
%
%
% ----- SURFACES IDENTIFICATION ----- %
%
% Marker(s) of the surface in the surface flow solution file
MARKER_PLOTTING= (wall1)
%
% Marker(s) of the surface where the non-dimensional coefficients are
% evaluated
MARKER_MONITORING= (wall1)
%
% Marker(s) between turbomachinery performance are evaluated. Use BLADE
% for single blade, STAGE for stage and TURBINE for a multi-stage.
MARKER_TURBOMACHINERY= (inflow, outflow)
%
%
%
% ----- GRID ADAPTATION STRATEGY ----- %
%
% Kind of grid adaptation (NONE, PERIODIC)
KIND_ADAPT= PERIODIC
%
%
%
% ----- DYNAMIC MESH DEFINITION ----- %
%
% Dynamic mesh simulation (NO, YES)
GRID_MOVEMENT= NO
%
% Type of dynamic mesh (NONE, ROTATING-FRAME)
GRID_MOVEMENT_KIND= ROTATING_FRAME ROTATING_FRAME
%
% Motion mach number (non-dimensional). Used for intitializing a viscous
% flow
% with the Reynolds number and for computing force coeffs. with dynamic

```

```

% meshes.
MACH_MOTION= 0.35
%
% Angular velocity vector (rad/s) about the motion origi. Example 1250 RPM
% >> 130.89969389957471 rad/s
ROTATION_RATE_X = 0.0 0.0
ROTATION_RATE_Y = 0.0 0.0
ROTATION_RATE_Z = 0.0 1990.0
%
%
%
% ----- COMMON PARAMETERS DEFINING THE NUMERICAL METHOD ----- %
%
% Numerical method for spatial gradients (GREEN-GAUSS,
% WEIGHTED-LEAST-SQUARES)
NUM_METHOD_GRAD= WEIGHTED_LEAST_SQUARES
%
% Courant-Friedrichs-Lewy condition of the finest grid
CFL_NUMBER= 40.0
%
% Adaptive CFL number (NO, YES)
CFL_ADAPT= NO
%
% Parameters of the adaptive CFL number (factor down, factor up, CFL min
% value, CFL max value )
CFL_ADAPT_PARAM= ( 0.3, 0.5, 1.0, 1000.0)
%
%
%
% ----- LINEAR SOLVER DEFINITION ----- %
%
% Linear solver or smoother for implicit formulations (BCGSTAB, FGMRES,
% SMOOTHER-JACOBI, SMOOTHER-ILU0, SMOOTHER-LUSGS, SMOOTHER-LINELET)
LINEAR_SOLVER= FGMRES
%
% Preconditioner of the Krylov linear solver (ILU0, LU-SGS, LINELET,
% JACOBI)
LINEAR_SOLVER_PREC= LU_SGS
%
% Min error of the linear solver for the implicit formulation
LINEAR_SOLVER_ERROR= 1E-4
%
% Max number of iterations of the linear solver for the implicit
% formulation
LINEAR_SOLVER_ITER= 5
%
%
%
% ----- MULTIGRID PARAMETERS ----- %
%
% Multi-Grid Levels (0 = no multi-grid)
MGLEVEL= 0
%

```

```

% Multigrid pre-smoothing level
MG_PRE_SMOOTH= ( 1, 2, 3, 3 )
%
% Multigrid post-smoothing level
MG_POST_SMOOTH= ( 0, 0, 0, 0 )
%
% Jacobi implicit smoothing of the correction
MG_CORRECTION_SMOOTH= ( 0, 0, 0, 0 )
%
% Damping factor for the residual restriction
MG_DAMP_RESTRICTION= 0.75
%
% Damping factor for the correction prolongation
MG_DAMP_PROLONGATION= 0.75
%
%
%
% ----- SLOPE LIMITER DEFINITION ----- %
%
% Reference element length for computing the slope and sharp edges
% limiters (0.1 m, 5.0 in by default)
REF_ELEM_LENGTH= 0.1
%
% Coefficient for the limiter
LIMITER_COEFF= 0.5
%
% Freeze the value of the limiter after a number of iterations
LIMITER_ITER= 999999
%
%
%
% ----- FLOW NUMERICAL METHOD DEFINITION ----- %
%
% Convective numerical method (JST, ROE, AUSM, HLLC)
CONV_NUM_METHOD_FLOW= ROE
%
% Spatial numerical order integration (1ST-ORDER, 2ND-ORDER,
% 2ND-ORDER-LIMITER)
SPATIAL_ORDER_FLOW= 2ND_ORDER_LIMITER
%
% Entropy fix coefficient (0.0 implies no entropy fixing, 1.0 implies
% scalar artificial dissipation, 0.001 default)
ENTROPY_FIX_COEFF= 0.001
%
% 1st, 2nd and 4th order artificial dissipation coefficients
AD_COEFF_FLOW= ( 0.15, 0.5, 0.02 )
%
% Slope limiter (VENKATAKRISHNAN, BARTH-JESPERSEN, VAN-ALBADA)
SLOPE_LIMITER_FLOW= VAN_ALBADA
%
% Time discretization (RUNGE-KUTTA-EXPLICIT, EULER-IMPLICIT,
% EULER-EXPLICIT)
TIME_DISCRE_FLOW= EULER_IMPLICIT
%

```

```
% Relaxation coefficient
RELAXATION_FACTOR_FLOW= 1.0
%
%
%
% ----- TURBULENT NUMERICAL METHOD DEFINITION ----- %
%
% Convective numerical method (SCALAR-UPWIND)
CONV_NUM_METHOD_TURB= SCALAR_UPWIND
%
% Spatial numerical order integration (1ST-ORDER, 2ND-ORDER,
% 2ND-ORDER-LIMITER)
SPATIAL_ORDER_TURB= 1ST_ORDER
%
% Slope limiter (VENKATAKRISHNAN)
SLOPE_LIMITER_TURB= VENKATAKRISHNAN
%
% Time discretization (EULER-IMPLICIT)
TIME_DISCRE_TURB= EULER_IMPLICIT
%
% Reduction factor of the CFL coefficient in the turbulence problem
CFL_REDUCTION_TURB= 0.01
%
% Relaxation coefficient
RELAXATION_FACTOR_TURB= 1.0
%
%
%
DV_KIND= SCALE
DV_MARKER=(airfoil, wall1, periodic1, periodic2, inflow, outflow)
DV_PARAM= 1, 1
DV_VALUE= 0.001
%
% ----- CONVERGENCE PARAMETERS ----- %
%
% Number of total iterations
EXT_ITER= 2501
%
% Convergence criteria (CAUCHY, RESIDUAL)
CONV_CRITERIA= RESIDUAL
%
% Flow functional for the Residual criteria (RHO, RHO_ENERGY)
RESIDUAL_FUNC_FLOW= RHO_ENERGY
%
% Residual reduction (order of magnitude with respect to the initial
% value)
RESIDUAL_REDUCTION= 6
%
% Min value of the residual (log10 of the residual)
RESIDUAL_MINVAL= -16
%
% Start convergence criteria at iteration number
STARTCONV_ITER= 10
%
% Number of elements to apply the criteria
```

```
CAUCHY_ELEMS= 100
%
% Epsilon to control the series convergence
CAUCHY_EPS= 1E-6
%
% Direct function to apply the convergence criteria (LIFT, DRAG,
% NEARFIELD-PRESS)
CAUCHY_FUNC_FLOW= DRAG
%
%
%
% ----- INPUT/OUTPUT INFORMATION ----- %
%
% Mesh input file
MESH_FILENAME= su2mesh_per.su2
%
% Mesh input file format (SU2, CGNS)
MESH_FORMAT= SU2
%
% Mesh output file
MESH_OUT_FILENAME= su2mesh_per.su2
%
% Restart flow input file
SOLUTION_FLOW_FILENAME= restart_flow.dat
%
% Output file format (PARAVIEW, TECPLOT, STL)
OUTPUT_FORMAT= TECPLOT
%
% Output file convergence history (w/o extension)
CONV_FILENAME= history
%
% Output file restart flow
RESTART_FLOW_FILENAME= restart_flow.dat
%
% Output file flow (w/o extension) variables
VOLUME_FLOW_FILENAME= flow
%
% Output file surface flow coefficient (w/o extension)
SURFACE_FLOW_FILENAME= surface_flow
%
% Writing solution file frequency
WRT_SOL_FREQ= 50
%
% Writing convergence history frequency
WRT_CON_FREQ= 1
```

B

Mesh Convergence Study

In contrast to applying CFD techniques to study a single geometry or flow in great detail, this project focused on the analysis of several blade configurations through the use of numerous simulations. It is customary to stop the calculations once certain residuals reach a previously specified tolerance.

In this work however, due to the possibility of using a previously validated solver for the specific application and the necessity of generating large amounts of data to produce trends, where accuracy is not a priority, a different approach was taken. A single configuration, the base blade with a single modification, the nozzle design Mach number taken to be the upper limit of the tested range ($M_a = 3.0$), was tested. This configuration was deemed to be representative for all other cases.

For the chosen grid generation program, *umg2*, several parameters were considered in the convergence study. These include the number of iterations used for a single simulation, the total number of mesh elements, the boundary layer thickness (chosen as a factor of the throat width) and the radius of the trailing edge refinement circle (chosen as a factor of the trailing edge width). The use of factors to set the value of some parameters was necessary to generalize the results for the range of possible geometries.

To monitor the convergence of the results, the residual of the entropy generation coefficient s_{gen} calculated by the CFD solver has been used. The residual is defined in a similar way to the errors previously defined in Equation 4.2, although the difference is taken between the chosen value of the parameter and the final value of the tested interval, denoted by Δs_{gen} . This parameter should reach a value under a prescribed tolerance. This leads to the specification of the following condition

$$\epsilon_{mesh} = \frac{\Delta s_{gen}}{s_{gen}} < tol, \quad (B.1)$$

which can only be defined correctly if the tested values in the interval converge to a certain value.

First the number of iterations was tested by running a simulation for $2 \cdot 10^5$ iterations (considered to be sufficient for convergence given previous experience with the solver). To explore the most extreme case possible, $6 \cdot 10^4$ mesh elements, a boundary layer thickness factor of 0.2 and no refinement circle were specified. The resulting trend can be visualized in Figure B.1. Based on the results shown in the plot, taking a total number of iterations of 10^4 would result in $\epsilon_{mesh} < 10^{-3}$, which is expected to be a reasonable value.

Subsequently, the boundary layer thickness was varied. This was done for the chosen number of iterations and mesh elements, and a refinement circle with radius $R_{TE} = 5t$. The relevant interval was taken to be $\{H_{BL} \mid 0 \leq \frac{0.5H_{BL}}{o} \leq 0.3\}$, the outcome of which is presented in Figure B.2. It can be noticed that due to the unclear convergence of s_{gen} for this parameter, it is not meaningful to define ϵ_{mesh} . It is also difficult only based on this data to monitor the value of y^+ . Therefore a value $\frac{H_{BL}}{o} = 0.15$ was taken, based mainly on heuristic considerations.

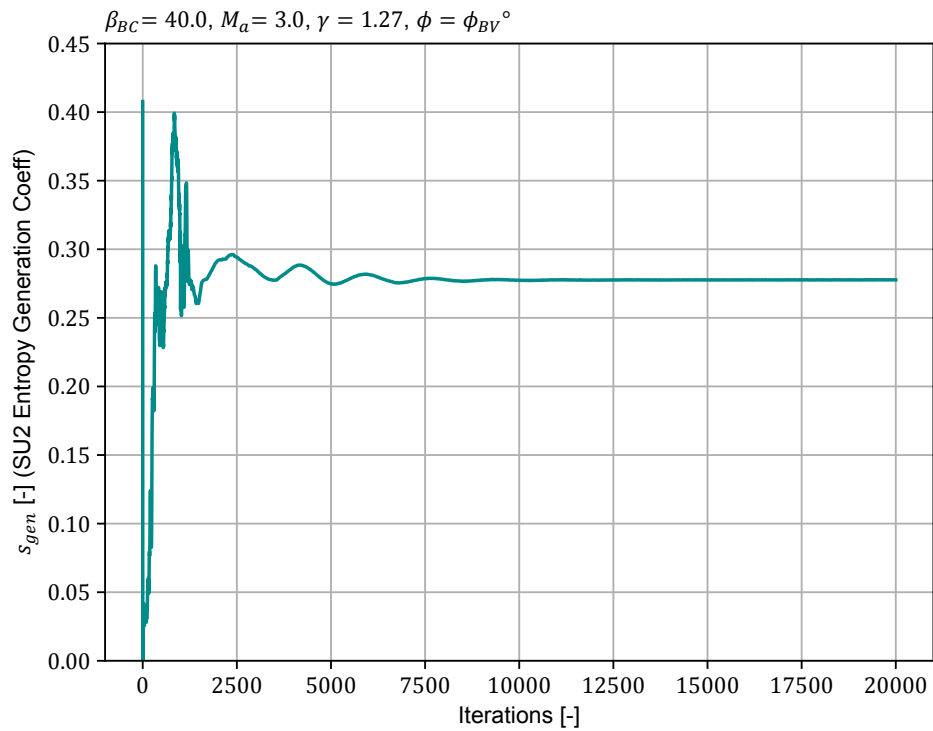


Figure B.1: Mesh convergence for number of simulation iterations

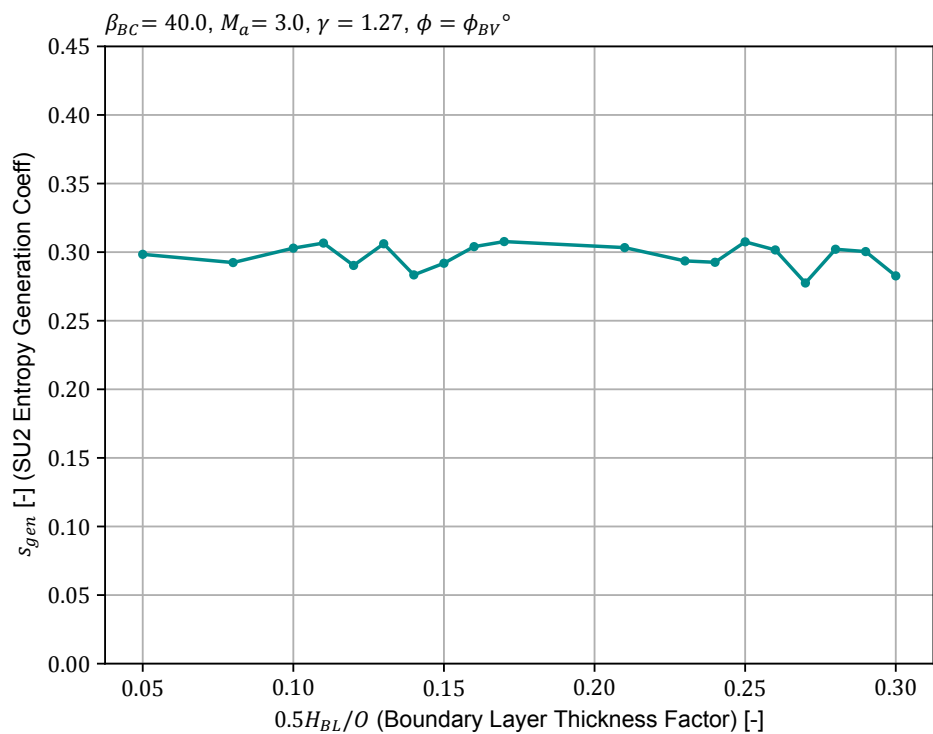


Figure B.2: Mesh convergence for boundary layer thickness

Next, the number of elements, for the given ratio of cell sizes chosen for the mesh (cf. Figure 3.10), was tested, for a range between $5 \cdot 10^4 - 20 \cdot 10^4$ elements, the result of which is shown in Figure B.3. Again in this case, there is no clear sign yet of a convergence of

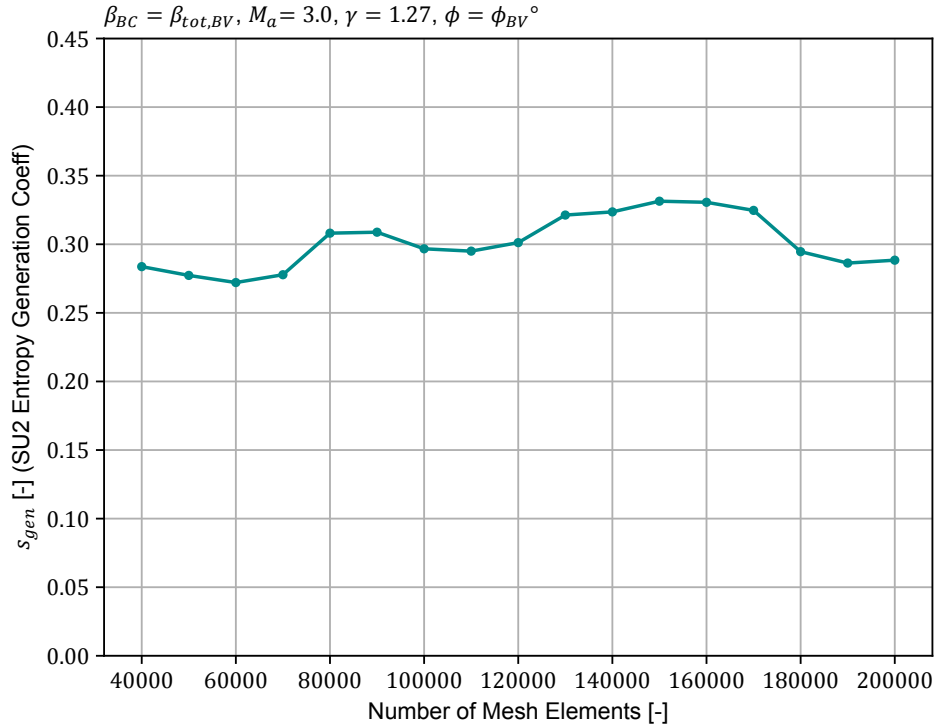


Figure B.3: Mesh convergence for number of elements

the monitored variable. It is suspected that this is due to a trade-off effect occurring when increasing the number of mesh elements when using *umg2*: the overall mesh becomes finer, but the aspect ratio of the cells in the transition region between the boundary layer and the open flow passage near the blade TE decreases. Due to the criticality of this region, it could have a major effect on the solution convergence. Once again in this case, based on heuristics, a number of overall elements of 10^4 was chosen.

Finally, the effect of the refinement circle was studied. The corresponding factor was varied in the interval between 0 – 20. The results are shown in Figure B.4. The results seem to suggest that this value does not have a substantial effect on the simulation convergence. This is expected to be due to the fact that the refinement only makes sense around the very small region around the trailing edge where the most complex flow structures are formed. Based on these configurations, it was decided to take factors between 5 – 6 depending on the configuration.

In summary, while this simple study cannot guarantee the convergence of every simulation performed using the tools in this work, it provides a reasonable argument for the choice of the relevant mesh parameters. This statement is of course made in the context of the sequential mesh generation of numerous geometries with the aim of producing trends, where accuracy is not the main priority.

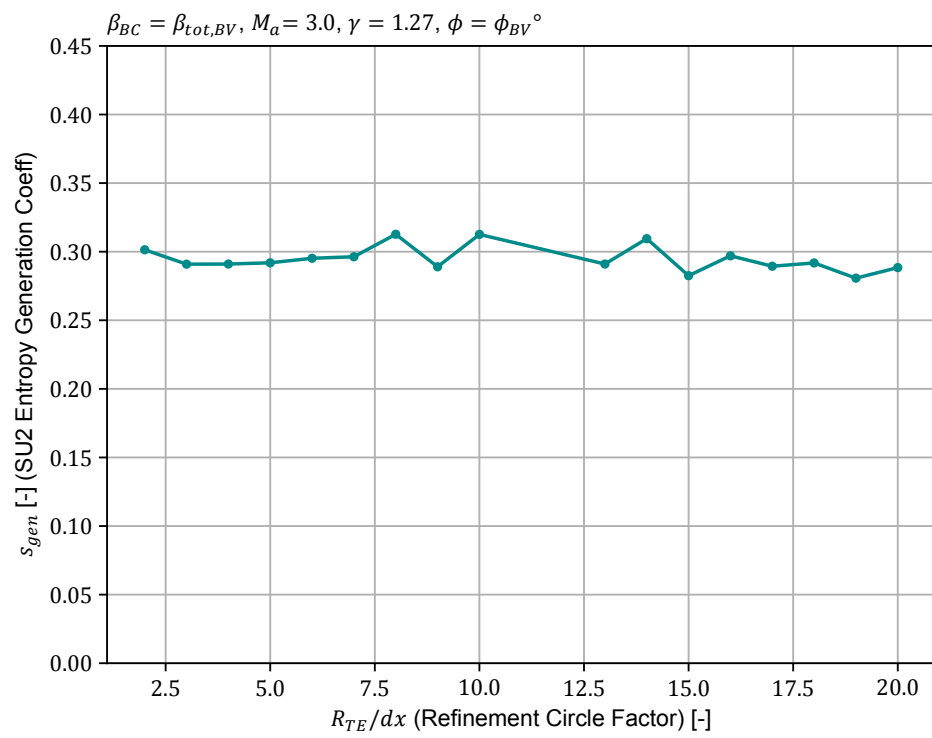
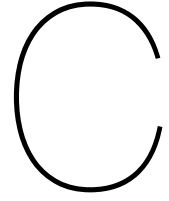


Figure B.4: Mesh convergence for trailing edge refinement radius



Line Integration Validation

Given that the nozzle exit boundary is split on both sides of a blade for the chosen computational domain (cf. Figure 3.10), it is a more complex task to extract properties along this line. To address this complication, a property calculation routine was devised combining a point extraction macro using the commercial software package *TecPlot360* and a line integration procedure using a custom made *Python* script as explained in subsection 3.2.5.

To ensure that the results of this procedure could be used for this project, a quick validation was made by comparing the results of both area and mass averaged properties, by controlling the pressure and the entropy respectively, using a manual line integration in *TecPlot360* and the script. The calculations were done for three different blade configurations with varying M_a at the same operating conditions. These results have been summarized in Table C.1.

Table C.1: Results between commercial package line integration and custom made script for mass (entropy) and area (pressure) average values

M_a [-]	P_a [Pa]		s_a [kJ kg ⁻¹ K ⁻¹]	
	Tec360	Script	Tec360	Script
1.6	506960	508744	3843.14	3840.83
2.5	73958	73371	3838.21	3834.60
3.0	21989	21100	3839.21	3838.18

The results above show an acceptable difference between both methods for the accuracy requirement inherent to a research based on finding trends.

Bibliography

- [1] Statista. Projected global energy consumption from 1990 to 2040, by energy source (in million metric tons of oil equivalent), 2018. URL <https://www.statista.com/statistics/222066/projected-global-energy-consumption-by-source/>. Online; accessed 25-08-2018.
- [2] BP. Bp energy outlook 2040 - summary tables, 2018. URL <https://www.bp.com/en/global/corporate/energy-economics/energy-outlook/energy-outlook-downloads.html>. Online; accessed 25-08-2018.
- [3] European Commission. Report from the commission to the european parliament and the council 2017 assessment of the progress made by member states towards the national energy efficiency targets for 2020 and towards the implementation of the energy efficiency directive as required by article 24(3) of the energy efficiency directive 2012/27/eu. Report, European Union, Brussels, Nov 2017. URL [https://eur-lex.europa.eu/legal-content/EN/TXT/?qid=1511978095545&uri=COM:2017:687:FIN.COM/2017/0687 final](https://eur-lex.europa.eu/legal-content/EN/TXT/?qid=1511978095545&uri=COM:2017:687:FIN.COM/2017/0687%20final).
- [4] T. C. Hung, T. Y. Shai, and S. K. Wang. A review of organic rankine cycles (orcs) for the recovery of low-grade waste heat. *Energy*, 22(7):661–667, 1997. ISSN 0360-5442. doi: 10.1016/s0360-5442(96)00165-x. URL <GotoISI>://WOS:A1997WW73600004. ISI Document Delivery No.: WW736 Pergamon-elsevier science ltd Oxford.
- [5] S. Bahamonde, M. Pini, C. De Servi, A. Rubino, and P. Colonna. Method for the preliminary fluid dynamic design of high-temperature mini-organic rankine cycle turbines. *Journal of Engineering for Gas Turbines and Power-Transactions of the Asme*, 139(8), 2017. ISSN 0742-4795. doi: 10.1115/1.4035841. URL <http://gasturbinespower.asmedigitalcollection.asme.org/article.aspx?articleid=2600400>.
- [6] E. Macchi. *Theoretical basis of the Organic Rankine Cycle*, pages 3–24. Woodhead Publishing Series in Energy, 2016. doi: 10.1016/B978-0-08-100510-1.00001-6. URL <https://www.scopus.com/inward/record.uri?eid=2-s2.0-85017442302&doi=10.1016%2fB978-0-08-100510-1.00001-6&partnerID=40&md5=86cbb186d44ff7109ff05e56cb09ba9d>.
- [7] P. Colonna, E. Casati, C. Trapp, T. Mathijssen, J. Larjola, T. Turunen-Saaresti, and A. Uusitalo. Organic rankine cycle power systems: From the concept to current technology, applications, and an outlook to the future. *Journal of Engineering for Gas Turbines and Power*, 137(10), 2015. doi: 10.1115/1.4029884. URL http://gasturbinespower.asmedigitalcollection.asme.org/data/journals/jetpez/933718/gtp_137_10_100801.pdf.
- [8] S. Dixon and C. Hall. *Fluid Mechanics and Thermodynamics of Turbomachinery*. Fluid Mechanics and Thermodynamics of Turbomachinery. Elsevier Butterworth-Heinemann, 2010. doi: 10.1016/C2009-0-20205-4. URL <https://www.scopus.com/inward/record.uri?eid=2-s2.0-85013831508&doi=10.1016%2fC2009-0-20205-4&partnerID=40&md5=25678ef10424f791c258846b0521065e>.
- [9] G. Persico and M. Pini. *Fluid dynamic design of Organic Rankine Cycle turbines*, pages 253–297. Woodhead Publishing Series in Energy, 2016. doi: 10.1016/B978-0-08-100510-1.00008-9. URL <https://www.scopus.com/inward/record.uri?eid=2-s2.0-85017439096&doi=10.1016%2fB978-0-08-100510-1.00008-9&partnerID=40&md5=0c42ed49f26357eef2d0c15a911284c4>.

- [10] N. Anand, S. Vitale, M. Pini, G. J. Otero-Rodríguez, and R. Pecnik. Design methodology for supersonic radial vanes operating in non-ideal flow conditions. *Journal of Engineering for Gas Turbines and Power*, 2018. ISSN 0742-4795. doi: 10.1115/1.4040182. URL <http://dx.doi.org/10.1115/1.4040182>. 10.1115/1.4040182.
- [11] L. Zhang, W. L. Zhuge, Y. J. Zhang, and T. Chen. Similarity theory based radial turbine performance and loss mechanism comparison between r245fa and air for heavy-duty diesel engine organic rankine cycles. *Entropy*, 19(1), 2017. ISSN 1099-4300. doi: 10.3390/e19010025. URL <http://www.mdpi.com/1099-4300/19/1/25/pdf>.
- [12] J. Harinck, D. Pasquale, R. Pecnik, J. van Buijtenen, and P. Colonna. Performance improvement of a radial organic rankine cycle turbine by means of automated computational fluid dynamic design. *Proceedings of the Institution of Mechanical Engineers Part a-Journal of Power and Energy*, 227(6):637–645, 2013. ISSN 0957-6509. doi: 10.1177/0957650913499565. URL <http://journals.sagepub.com/doi/pdf/10.1177/0957650913499565>.
- [13] M. White and A. I. Sayma. Investigating the effect of changing the working fluid on the three-dimensional flow within organic rankine cycle turbines. In *Proceedings of the ASME Turbo Expo*, volume 3, 2016. doi: 10.1115/GT2016-56106. URL <http://proceedings.asmedigitalcollection.asme.org/proceeding.aspx?articleid=2554996>.
- [14] J. A. Keep, S. Vitale, M. Pini, and M. Burigana. Preliminary verification of the open-source cfd solver su2 for radial-inflow turbine applications. *Energy Procedia*, 129: 1071–1077, 2017. doi: 10.1016/j.egypro.2017.09.130. URL <https://www.scopus.com/inward/record.uri?eid=2-s2.0-85029774803&doi=10.1016%2fj.egypro.2017.09.130&partnerID=40&md5=3358d8c3ea962cb3abdce683ea00e5a9>.
- [15] E. Rinaldi, R. Pecnik, and P. Colonna. Unsteady operation of a highly supersonic organic rankine cycle turbine. *Journal of Turbomachinery*, 138(12), 2016. doi: 10.1115/1.4033973. URL http://turbomachinery.asmedigitalcollection.asme.org/data/journals/jotuei/935341/turbo_138_12_121010.pdf.
- [16] A. P. S. Wheeler and J. Ong. A study of the three-dimensional unsteady real-gas flows within a transonic orc turbine. In *Proceedings of the ASME Turbo Expo*, volume 3B, 2014. doi: 10.1115/GT2014-25475. URL <http://proceedings.asmedigitalcollection.asme.org/proceeding.aspx?articleid=1907813>.
- [17] A. P. S. Wheeler and J. Ong. The role of dense gas dynamics on orc turbine performance. In *Proceedings of the ASME Turbo Expo*, volume 2, 2013. doi: 10.1115/GT2013-95858. URL <http://proceedings.asmedigitalcollection.asme.org/proceeding.aspx?articleid=1776062>.
- [18] F. Lang. Ikea furniture and the limits of ai, 2018. URL <https://www.economist.com/leaders/2018/04/21/ikea-furniture-and-the-limits-of-ai>. The Economist. Online; accessed 21-04-2018.
- [19] A. Guardone, A. Spinelli, and V. Dossena. Influence of molecular complexity on nozzle design for an organic vapor wind tunnel. *Journal of Engineering for Gas Turbines and Power*, 135(4), 2013. doi: 10.1115/1.4023117. URL <http://gasturbinespower.asmedigitalcollection.asme.org/article.aspx?articleid=1671882>.
- [20] C. A. M. Ventura, P. A. Jacobs, A. S. Rowlands, P. Petrie-Repar, and E. Sauret. Preliminary design and performance estimation of radial inflow turbines: An automated approach. *Journal of Fluids Engineering, Transactions of the ASME*, 134(3), 2012. doi: 10.1115/1.4006174. URL <https://www.scopus.com/inward/record.uri?eid=2-s2.0-84859919524&doi=10.1115%2f1.4006174&partnerID=40&md5=363c5bec9a98e13fc309b8466b812054>.

- [21] A. M. Al Jubori, R. K. Al-Dadah, S. Mahmoud, and A. Daabo. Modelling and parametric analysis of small-scale axial and radial outflow turbines for organic rankine cycle applications. *Applied Energy*, 190:981–996, 2017. ISSN 0306-2619. doi: 10.1016/j.apenergy.2016.12.169. URL <GotoISI>://WOS:000395959100080.
- [22] E. Macchi. Design criteria for turbines operating with fluids having a low speed of sound. Lecture Series, Politecnico di Milano, 1977.
- [23] M. Ye. Deych and B. M. Troyanovskiy. Investigation and calculation of axial-turbine stages. Technical report, Air Force Systems Command, Jan 1968.
- [24] J.D. Anderson. *Fundamentals of Aerodynamics*. Series in Aeronautical and Aerospace Engineering. McGraw-Hill, New York, NY, fifth edition, 2011.
- [25] P. Bakker and B. van Leer. Lecture notes on gasdynamics, ae4-140. Delft University of Technology, 2005.
- [26] R. Sauer. General characteristics of the flow through nozzles at near critical speeds (allegemeine eigenschaften der stromung durch duesen in der naehe der kritischen geschwindigkeit; german). Technical report, NASA, 1947. Translated into English by NACA.
- [27] D. Pasquale, A. Ghidoni, and S. Rebay. Shape optimization of an organic rankine cycle radial turbine nozzle. *Journal of Engineering for Gas Turbines and Power-Transactions of the Asme*, 135(4), 2013. ISSN 0742-4795. doi: 10.1115/1.4023118. URL http://gasturbinespower.asmedigitalcollection.asme.org/data/journals/jetpez/926648/gtp_135_4_042308.pdf. 1528-8919.
- [28] J. D. Denton. Loss mechanisms in turbomachines. *Journal of Turbomachinery*, 115(4): 621–656, 1993. doi: 10.1115/1.2929299. URL <https://www.scopus.com/inward/record.uri?eid=2-s2.0-0027677224&doi=10.1115%2f1.2929299&partnerID=40&md5=725445e6e767103f73b0b33c98395b2a>.
- [29] P. Raj. *Physical-based Loss Models for Organic Rankine Cycle Turbines*. Master thesis, Delft University of Technology, 2016. URL <http://repository.tudelft.nl>.
- [30] J. D. Denton. The 1993 igt scholar lecture: Loss mechanisms in turbomachines. *Journal of Turbomachinery*, 115(4):621–656, 1993. ISSN 0889-504X. doi: 10.1115/1.2929299. URL <http://turbomachinery.asmedigitalcollection.asme.org/article.aspx?articleid=1464386>. 10.1115/1.2929299.
- [31] S. Vitale, T. A. Albring, M. Pini, N. R. Gauger, and P. Colonna. Fully turbulent discrete adjoint solver for non-ideal compressible flow applications. *Journal of the Global Power and Propulsion Society*, 1:252–270, 2017. ISSN 2515-3080. doi: 10.22261/JGPPS.Z1FVOI. URL <https://www.gppsjournal.org/journals/journal-of-the-global-power-and-propulsion-society/design-method-for-turbomachinery-working-in-the-nicfd-regime/>.
- [32] M. Pini. Lecture 6 - cascade aerodynamics (turbomachinery – ae 4206). Delft University of Technology, 2016.
- [33] J. D. Denton and N. A. Cumpsty. Loss mechanisms in turbomachines. In *Institution of Mechanical Engineers*, pages 1–14, 1987. URL <https://www.scopus.com/inward/record.uri?eid=2-s2.0-0023572549&partnerID=40&md5=4a3621834a0404fdec205b15fa8a2d17>.
- [34] E.M. Greitzer, C.S. Tan, and M.B. Graf. *Internal Flow Concepts and Applications*. Cambridge University Press, Cambridge, UK, 2004. ISBN 978-0-511-19553-2.
- [35] L. J. Goldman and M. R. Vanco. Analytical investigation of two-dimensional loss characteristics of supersonic turbine stator blades. Technical report, Lewis Research Center, NASA, 1969.

- [36] J. D. Denton and L. Xu. The trailing edge loss of transonic turbine blades. *Journal of Turbomachinery*, 112(2):277–285, 1990. ISSN 0889-504X. doi: 10.1115/1.2927648. URL <http://turbomachinery.asmedigitalcollection.asme.org/article.aspx?articleid=1463456>. 10.1115/1.2927648.
- [37] I. H. Bell, J. Wronski, S. Quoilin, and V. Lemort. Pure and pseudo-pure fluid thermophysical property evaluation and the open-source thermophysical property library coolprop. *Industrial & Engineering Chemistry Research*, 53(6):2498–2508, 2014. doi: 10.1021/ie4033999. URL <http://pubs.acs.org/doi/abs/10.1021/ie4033999>.
- [38] N. Anand. *Supersonic Turbine Design Using Method of Characteristics*. Master thesis, Delft University of Technology, 2016. URL <http://repository.tudelft.nl/>.
- [39] K. Ettabaa, M. Ali Hamdi, and R. Ben Salem. Svm for hyperspectral images classification based on 3d spectral signature. In *2014 International Conference on Advanced Technologies for Signal and Image Processing (ATSIP)*, pages 42–47, 2014. ISBN 978-1-4799-4888-8. doi: 10.1109/ATSIP.2014.6834635.
- [40] L. Pieggl and W. Tiller. *The NURBS Book*. Springer-Verlag Berlin Heidelberg, 1 edition, 1995. ISBN 978-3-642-97385-7. doi: 10.1007/978-3-642-97385-7.
- [41] O. R. Bingol. Nurbs-python, 2016. URL <https://doi.org/10.5281/zenodo.815010>.
- [42] T. D. Economon, F. Palacios, S. R. Copeland, T. W. Lukaczyk, and J. J. Alonso. Su2: An open-source suite for multiphysics simulation and design. *AIAA Journal*, 54(3):828–846, 2015. ISSN 0001-1452. doi: 10.2514/1.J053813. URL <https://doi.org/10.2514/1.J053813>.
- [43] M. Pini, S. Vitale, P. Colonna, G. Gori, A. Guardone, T. Economon, J. J. Alonso, and F. Palacios. Su2: The open-source software for non-ideal compressible flows. *Journal of Physics: Conference Series*, 821(1), 2017. doi: 10.1088/1742-6596/821/1/012013. URL <http://iopscience.iop.org/article/10.1088/1742-6596/821/1/012013/pdf>.
- [44] D. Y. Peng and D. B. Robinson. A new two-constant equation of state. *Industrial and Engineering Chemistry Fundamentals*, 15(1):59–64, 1976. doi: 10.1021/i160057a011. URL <https://www.scopus.com/inward/record.uri?eid=2-s2.0-0016917018&doi=10.1021%2fi160057a011&partnerID=40&md5=29cda5b04778c4c9b3e54b5c7c1b3291>.
- [45] F.R. Menter. Two-equation eddy-viscosity turbulence models for engineering applications. *AIAA Journal*, 32(8), 1994.
- [46] M. B. Giles. Nonreflecting boundary conditions for euler equation calculations. *AIAA Journal*, 28(12):2050–2058, 1990. doi: 10.2514/3.10521. URL <https://www.scopus.com/inward/record.uri?eid=2-s2.0-0025544847&doi=10.2514%2f3.10521&partnerID=40&md5=d914f3eb1f4433d60c375846088c1f82>.